The Dissertation Committee for Utsav KC Certifies that this is the approved version of the following dissertation

Development of a Multiple-Pass Raman Spectrometer For Flame Diagnostics

Committee:

Philip L. Varghese, Supervisor

Noel T. Clemens

Laxminarayan L. Raja

Manfred Fink

Adela Ben-Yakar

Development of a Multiple-Pass Raman Spectrometer For Flame Diagnostics

by

Utsav KC, B.A.; M.S.E.

Dissertation

Presented to the Faculty of the Graduate School of

The University of Texas at Austin

in Partial Fulfillment

of the Requirements

for the Degree of

Doctor of Philosophy

The University of Texas at Austin

May 2013

Dedication

To my parents Raju and Radha KC

Acknowledgements

I am grateful to my advisor Prof. Philip Varghese. He introduced me to the basics of optical alignment. He constantly led by example to inspire me to pay close attention to fine details, to find mistakes and to not make mistakes. I also realize that it would not have been possible for me to be successful in the various steps of the PhD program without the attention and the guidance that I received from him. It is not possible to fully describe my gratitude to him. To use an analogy, if I were a molecule which radiated the PhD work presented in this dissertation, then perhaps Dr. Varghese is the incident electric field tuned at the right frequency and with adequate intensity, which caused the radiation from the molecule.

I am also thankful to Dr. Clemens, Dr. Raja, Dr. Ben-Yakar and Dr. Fink, who are my PhD committee members. I am especially thankful to Dr. Clemens and Dr. Raja for opening my eyes to the broader field of optical diagnostics which extends far beyond Raman spectroscopy.

I am also thankful to Dr. Joel Silver of Southwest Sciences, Inc. as my research was initially sponsored by the United States Air Force through his company. I also thank PECOS for financially supporting me in the latter half of my PhD.

I would also like to acknowledge the love and support of my parents, my brother Pukar KC, and Vatsala Shah, who have always believed in me more than I ever have on myself. I also appreciate the support and encouragement from Prashant Shukla, Naresh Neupane, Marshall Albright, Shankar Mahadevan, Doug Breden and Hariswaran Sitaraman. I also appreciate the encouragement that I received from Dr. Raja every now and then.

Development of Multiple-Pass Raman Spectrometer For Flame Diagnostics

Utsav KC, PhD

The University of Texas at Austin, 2013

Supervisor: Philip L. Varghese

A multiple-pass cell is developed and applied to enhance the Raman signal from methane-air flames for temperature measurements. Stable operation of the cell was demonstrated and studied in two alignment modes. In the ring mode, the beams are focused into a ring of ~ 3 mm diameter at the center of the cell, and spectra were recorded at low dispersion (0.26 nm/pixel). Temperature is calculated from the ratio of the intensity of Stokes to anti-Stokes signal from nitrogen. Temperature is also inferred from the shapes of the Stokes and anti-Stokes peaks in the spectrum. The uncertainty in the value of flame temperature in these measurements was ±50 K. The signal gain from 100 passes is a factor of 83. Signal to noise ratio (SNR) improved by a factor of 9.3 in room temperature air with an even higher factor in flames. The improvement in SNR depends on the acquisition time and is best for short acquisition times. In the two point mode, multi passing is achieved simultaneously with high spatial resolution as the laser is focused at two small regions separated by ~ 2 mm at the center of the cell. The probe regions are 300 μm × 200 μm. The vast improvement in the spatial resolution is achieved at the cost of a reduced number of passes and signal gain. The two point mode is operated with 25 passes at each point with a signal gain factor of ~20; the SNR gain depends on the data acquisition time. Spectra were recorded at high dispersion (~0.03 nm/pixel).

Temperature is inferred from curve fitting to the high resolution Stokes spectrum of nitrogen in methane-air flames. The curve fit is based on very detailed simulation of Raman spectrum of nitrogen. The final model includes the angular dependence of Raman scattering, electrical and mechanical anharmonicity in the polarizability matrix elements, and the presence of a rare isotope of nitrogen in air. The uncertainty in the value of temperature in the least noisy data is ±9 K. The sources of uncertainty in temperature and their contribution to the total uncertainty are also identified.

Table of Contents

List of Tables

List of Figures

List of Illustrations

Chapter 1: Introduction

The inelastic scattering of light is called Raman scattering after C.V. Raman, who first demonstrated it. The basic introduction to Raman scattering is available in countless web pages and books on Raman spectroscopy. The history and evolution of Raman instrumentation is summarized in [1]. In this chapter, first the characteristics of some popular combustion diagnostics techniques are briefly outlined. It is followed by the explanation of some of the concepts which are involved in a deeper understanding of Raman scattering. Then the motivation for the development of a multiple-pass Raman instrument is described. After that the state of the art in Raman instrumentation is summarized and some of the applications of the multiple-pass technique for Raman diagnostics are stated. At the end of this chapter, an overview of the dissertation is presented.

1.1 General Background

Optical diagnostics methods can be categorized into passive and active techniques. In a passive technique the sample emits spontaneously and irradiation with an external light source is not required. Emission spectroscopy is an example of a passive technique. All the techniques in which the sample is irradiated with an external light source like a laser comprise the active techniques. The popular active optical diagnostics methods commonly used for combustion measurements are absorption, laser induced fluorescence, coherent anti-Stokes Raman, spontaneous Raman and Rayleigh spectroscopy. Absorption spectroscopy is a line of sight technique, whereas the others are point techniques which can have high spatial resolution. Here, some of the features of the point methods will be briefly reviewed, and in that context the advantages and limitations of the multiple pass based Raman spectroscopy will also be presented. One can learn

about optical diagnostics methods from their detailed descriptions available in several books [2-4] and review articles [5-7].

Signal Strength and Detectability

In order to rank the methods in terms of signal strength one should first distinguish between coherent and incoherent techniques. In a coherent technique like coherent anti-Stokes Raman spectroscopy (CARS) the signal propagates as a laser-like beam, whereas in the incoherent techniques like laser induced fluorescence (LIF), Rayleigh, and spontaneous Raman spectroscopy the signal is emitted in all directions. LIF can be used to detect species which are present in parts per million (ppm) and even sub-ppm concentrations. Rayleigh and Raman signals are much weaker than LIF signals for the same laser excitation power. Hence, much higher laser pulse energies are typically used for Rayleigh and Raman measurements than for LIF measurements. Additionally, the laser can be spread into a thin sheet to enable simultaneous multi-point laser induced fluorescence measurements in a plane (PLIF). Because of the need to maintain high laser excitation energy in the measurement volume Rayleigh and Raman measurements are typically limited to line measurements at best. The Raman cross section is typically less than Rayleigh cross section by a factor of 1000. Both Raman and CARS techniques can be used to detect minor species down to concentrations of ~0.1%. However, the conversion efficiency (P_s/P_i) in CARS is higher than in Raman typically by a factor of $\sim 10^7$ because in CARS all the scattered light is collected whereas in Raman only a small fraction of it is collected. For example, if the collection optics is f/5 then the collection solid angle is ~0.03, which means only 0.2% of the scattered light is recorded. Nevertheless single shot Raman spectroscopy is feasible using lasers with high pulse energies [8, 9].

Presently, tunable lasers are not readily available below 200 nm. When $\lambda < 200$ nm there is also strong absorption from air which means the laser is attenuated before it reaches the sample. For these two reasons, single photon LIF is not possible for species which absorb in the ultra violet. It is possible to overcome this problem by using two or multiple photon LIF. The single photon LIF signal is proportional to the laser power, but the two photon LIF signal is proportional to the ratio of the square of incident power to the area of the probe region so that it is desirable to focus the laser beam to a small volume. However, this can lead to photodissociation or photoionization of the sample species which can generate interferences or cause significant perturbations of the system being studied. The diagnostic technique loses its non-intrusive character. CARS and Raman spectroscopy can only be performed in molecules which are Raman active. Raman activity is described later in this chapter. Rayleigh scattering is less restrictive, but it cannot be used to distinguish between different species as the Rayleigh signals from all the species appear at the excitation wavelength.

CARS and LIF signals can be generated from only one molecular species at a time because the laser must be tuned to match a molecular resonance. Even when broad band CARS is used it typically does not cover multiple species, but only multiple transitions of a given species. In Raman spectroscopy it is possible to excite and record Raman signals from several species simultaneously, so it is a convenient technique for molecule identification.

Spatial Resolution

As noted above, LIF can generate strong signals so cylindrical lenses can be used to form laser sheets and fluorescence can be recorded from each point in the sheet. The signal from many points can be recorded simultaneously with spatial resolution of ~100

μm. CARS requires overlap of at least two laser beams so the spatial resolution is ~1 mm. In the single beam Raman and Rayleigh scattering it is possible to reduce the dimensions of the probe region to O(10-100μm). Raman and Rayleigh scattering can be recorded from multiple points simultaneously by using a multiple pass cell. Multiple point CARS has also been reported [16].

Interference

It is challenging to be quantitative in linear LIF because of the loss of excited species by photoionization, predissociation and quenching. The LIF signal power is given by [2]

$$F \propto laN_1^0 \frac{B_{12}}{B_{12}+B_{21}} \frac{A_{21}}{1+\frac{I_{sat}^{\nu}}{I_{\nu}}}, \tag{1.1}$$

where

$$I_{sat}^{\nu} = \frac{(A_{21}+Q_{21})c}{B_{12}+B_{21}}. \tag{1.2}$$

In the above equations, 2 is the excited energy state and 1 is the ground state, N_1^0 is the ground state population before excitation, A and B are the Einstein coefficients, l and a are the length and the area of the probe region, and Q is the quenching rate. Predissociation and photoionization rates are neglected in the derivation of the above equation as the excited species are mainly deactivated by quenching and spontaneous emission. According to eqn. 1.1, Q should be known for accurate interpretation of the signal. The value of Q depends on the pressure, temperature and composition of the mixture. The most common approaches used to circumvent this problem are as follows: (i) Q can be estimated using $Q_j = \sum_i \sigma_i n_i v_{ij}$; (ii) The value of A_{21} is well known so Q can be measured from the lifetime of the excited species, but this requires excitation using pico second lasers as the life time of the excited species is ~1 ns; (iii) One can

make $I_\nu \gg I_{sat}^{\nu}$ so that F is independent of Q, however this method also has its own limitations e.g. it may not be possible to achieve $I_\nu \gg I_{sat}^{\nu}$ at the temporal and spatial wings of the beam as the profile of I_ν is not a top-hat function.

The CARS spectrum has background from non-resonant transitions, which is one of its major sources of uncertainty. Similarly, in Rayleigh scattering there is interference by Mie scattering from particles and also stray light from the optical surfaces. They can be overcome with filtered Rayleigh scattering in which a very narrow width laser can be used to irradiate the sample and an atomic or molecular vapor cell can be inserted in the collection optics to attenuate the very intense Mie scattering and stray reflections from the optics. The Rayleigh signal is relatively broad (especially in flames) so the atomic or molecular absorber only removes the central portion of the signal where the strong interferences are located. The Rayleigh signal and fluorescence are the major sources of interference in spontaneous Raman scattering. Interference from Rayleigh scattering is typically suppressed with a notch filter. The fluorescence interference can be subtracted out from the Raman signal using polarization filters, because Raman signals have a strong polarized contribution, whereas fluorescence is unpolarized. CARS signals are less likely to suffer from interference from fluorescence because the CARS signal is blue shifted while fluorescence is red shifted from the excitation wavelength. Additionally the CARS signal is generated as a coherent beam so one can collect the entire signal with a small collection solid angle while spatially filtering out most of the flame luminosity and background scatter from any particles present in the flow. Because of its high signal to background ratio and coherent signal beam CARS is often used for measurements in industrial scale devices.

Thermometry

Because it is a non-linear technique, the shape of the recorded CARS spectrum depends in a complex way on the mode structure of the laser (which may vary from pulse to pulse) and on the non-resonant susceptibility of the medium, in addition to the resonant susceptibility of the species being studied. Thus CARS spectra are difficult to model and tend to fluctuate with each laser pulse and when using CARS the temperature is typically determined from the shape of the spectrum by comparing the recorded spectrum with a library of reference spectra recorded or computed at fixed temperature intervals. In Raman spectroscopy the temperature is inferred from curve fitting the spectrum or from the ratio of Stokes to anti-Stokes signals. Because it is a linear technique it is much easier to compute the Raman spectrum and the shape of the spectrum is not distorted by laser pulse-to-pulse fluctuations. In Rayleigh scattering temperature is inferred by using the ideal gas equation or from the Doppler width of the Rayleigh signal. In LIF the temperature is determined by measuring the intensity of various transitions and then determining temperature using the Boltzmann relation between state population and temperature.

Table 1.1 and 1.2 list some examples of temperature measurements in flames using various methods. The uncertainty in the temperature measurements is not always estimated consistently. In most of the cases ΔT is determined by comparing with measurement from an alternative method. In some cases comparisons are made with thermocouple temperature measurements which themselves have an uncertainty of few percent. The uncertainty in temperature also depends on the thermometric species as the values of molecular parameters are required to calculate temperature.

Besides noise, the error in temperature measurement is also caused by uncertainty in the values of some of the input parameters in the scattering calculations. The error in

CARS temperature measurements arise from uncertainty in the value of non-resonant susceptibility and the Raman line widths. The error in CARS temperature at high pressure is particularly caused by the lack of accurate quantification of the collisional narrowing effects on the Raman line widths. Such effects become important in CARS at lower pressures than in Raman spectroscopy. The error in the LIF temperature measurements can be mainly attributed to the uncertainty in the quenching, predissociation and photo dissociation rates. The error in Rayleigh temperature measurements is caused by the uncertainty in the Rayleigh cross sections of the sample constituents.

Table 1.1: Examples of temperature measurements using LIF spectroscopy.

Diagnostic technique	Thermometric species (Sample flame)	T [K]	Determination of ΔT
LIF [10]	OH, NH, CH (H_2/N_2O, H_2/O_2, C_3H_8/N_2O, C_3H_8/O_2)	1000 – 2500 ± 100	Comparison between T_{OH}, T_{NH}, T_{CH}
LIF [11]	Indium (CH_4/air)	1700 – 2000 ± 75	RMS spread in T
LIF [12]	OH (CH_4/air)	2000 ± 100	Comparison with absorption measurements
LIF [13]	O_2 (air furnace)	1800 ± 23[1]; 1800 ± 126[2]	Comparison with thermocouple measurements (tc); std. deviation of measurements

[1] Signal from 100 pulses
[2] Signal from single pulse

Table 1.2: Examples of temperature measurements using Rayleigh, CARS and Raman spectroscopy.

Diagnostic technique	Thermometric species (Sample flame)	T [K]	Determination of ΔT
Rayleigh [15]	(C_3H_8/air)	1700 ± 68	
Rayleigh [16]	(H_2/air)	2400 ± 75	Comparison with CARS and calculations
CARS [17]	N_2	2104 ± 9	Comparison with tc
CARS [18]	N_2 (CH_4/air)	1826 - 4	Comparison with tc $\Delta T_{tc} = \pm 60$ K
Raman [19]	H_2, N_2 (H_2/air)	1880 ± 21[3] 1890 ± 80[4] 1995 ± 130[5] 1900 ± 150[6]	
Raman [20]	N_2 (CH_4/air)	1975 ± 59[7] 1950 ± 115[8]	
Raman [21]	CO, CO_2, H_2O, N_2 (CH_4/air, C_2H_6/air)	400 – 2150 ± 100	Comparison between T_{CO}, T_{CO_2}, T_{H_2O}, T_{N_2}
Raman [22]	N_2, CO_2, H_2O, O_2 (DME/air)	2171± 43 2171 ± 87 2171 ± 65 2171 ± 43	

Given the availability of various optical diagnostics techniques for flame temperature measurements, multiple pass Raman spectroscopy is most suitable when it is

[3]Rotational T_{N_2}
[4] Rotational T_{H_2}
[5] Vibrational T_{N_2}
[6] Vibrational T_{H_2}
[7] Temperature from curve fitting.
[8] Temperature from the intensity ratio of the fundamental to the first hot band.

desirable to do Raman spectroscopy using a low energy pulse laser; the refractive index along the beam path is relatively constant; the sample breaks down even with relatively low laser irradiance; precise Raman measurements are necessary; a compact set up is necessary. The signal enhancement in a multiple pass cell is limited by the mirror diameter and reflectivity. If the sample is inside a glass cell then the transmittance of the windows also puts a limit on the signal gain. As the fluctuations in the refractive index along the beam path increase the number of passes has to be reduced to prevent misalignment. The requirement of only a single optical port is often cited as an advantage of Raman spectroscopy over CARS as the signal in Raman spectroscopy can be back scattered, but in CARS at least two optical ports are required as the signal propagates in the direction of the incident beam. However in a multiple pass based Raman spectroscopy at least three optical ports are necessary when the sample is inside a chamber.

1.2 BACKGROUND TO RAMAN SPECTROSCOPY

An external electric field is able to induce an electric dipole in an atom or a molecule by distorting its electron cloud. An electric dipole is a pair of charges of equal magnitude q, and opposite sign separated by a given distance s. The dipole moment $\boldsymbol{P} = q\boldsymbol{s}$. The polarizability is the property which indicates how easily the electron cloud can be distorted to form an induced dipole. Not all the molecules which can acquire an induced dipole show Raman activity. A vibrational mode is Raman active when the derivative of the polarizability changes about the equilibrium inter-nuclear separation. For example, in the case of the bending mode of CO_2, the polarizability profile as a function of inter-nuclear separation is symmetric about the equilibrium separation so that although the polarizability changes during the bending mode, the derivative of polarizability does not change about the equilibrium inter-nuclear separation and so the bending mode of CO_2 is

not Raman active. For the symmetric stretch of CO_2, the derivative of polarizability with respect to inter-nuclear separation is not zero at the equilibrium inter-nuclear separation and so the symmetric stretch mode of vibration in CO_2 is Raman active [23]. In the case of N_2, only one mode of vibration is possible. When the two N nuclei are closest to one another the polarizability is minimum and when the two nuclei are farthest from one another the polarizability is maximum. Thus, the polarizability changes at the equilibrium inter-nuclear separation and so the vibrational mode of N_2 is Raman active.

Depending on the symmetry of the molecule, the scattered light can be polarized in any direction relative to the incident polarization. The explanation is as follows. The induced electric dipole term can be expanded into terms of several orders ($\boldsymbol{P} = \boldsymbol{\alpha}.\boldsymbol{E} + \frac{1}{2}\boldsymbol{\beta}:\boldsymbol{EE} + \frac{1}{6}\boldsymbol{\gamma}\vdots\boldsymbol{EEE} + \cdots$). In this thesis, only normal Raman scattering which arises from the first order term is of interest ($\boldsymbol{\alpha}.\boldsymbol{E}$). Hyper Raman scattering that is attributed to the second order term and second hyper Raman scattering that is attributed to the third order term are much weaker in intensity, and they appear at higher shifts than the normal Raman scattering. Each component of the polarizability tensor $\boldsymbol{\alpha}$ can be expanded in Taylor series with respect to the normal coordinate of vibration:

$$\alpha_{ij} = (\alpha_{ij})_0 + \left(\frac{\partial \alpha_{ij}}{\partial \xi}\right)_0 \xi + \frac{1}{2}\left(\frac{\partial^2 \alpha_{ij}}{\partial \xi^2}\right)_0 \xi^2 + \cdots \qquad (1.3)$$

The index *i* is the direction of the induced dipole and the index *j* is the direction of the electric field which induces the dipole. A normal mode of vibration is chosen to decompose the overall vibrational motion of the molecule into independent vibrational modes [9]. Here, $\xi = \frac{x - x_0}{x_0}$, where x_0 is the equilibrium separation between the nuclei. The first term in the expansion accounts for Rayleigh scattering. The second term accounts for

[9] A normal mode is an eigen function of the nuclear displacement operator, where the displacements are relative to the center of the mass.

Raman scattering in the harmonic oscillator assumption, and the scattering intensity is proportional to

$$I \propto \int \psi_m^* \left(\frac{\partial \alpha_{ij}}{\partial \xi}\right)_0 \xi \psi_n d\xi. \tag{1.4}$$

Here, ψ_n and ψ_m represent the wavefunctions of the initial and the final energy states, respectively.

Raman scattering has very weak signal. In a physical sense the small cross section of Raman scattering is explained as follows. The energy states can be modeled as wave functions and so the lower state of the molecule can be excited to the tail end of the upper electronic state. The tail end of the upper electronic state is also referred to as the virtual state. The probability of existence in the tail end is very low, so in ~10^{-15}s the molecule falls back to an energy state which is close to the original lower state. This is the reason the Raman scattering appears instantaneous. It is also the reason the scattering process is very weak.

Equation (1.4) represents Raman scattering with an assumption of electrical harmonicity. Alternatively one can take the inner product by including also the zeroeth and the higher order terms in eqn. (1.3) in which case the inner product with respect to the first term explains Rayleigh scattering, and Raman scattering is also dependent on the higher order terms. The oscillations in the electric field is analogous to that of a mechanical oscillator and as a result of the inclusion of the higher order derivatives the electric field oscillations become analogous to an anharmonic oscillator, so that the inclusion of the higher order terms of eqn. (1.3) in the inner product of the initial and final state with respect to the polarizability operator is referred to as allowing for the electrical anharmonicity in the scattering model.

In addition to so-called electrical harmonic/anharmonic effects, the anharmonic effects may be included or neglected in the mechanical vibration of the molecule. If the molecular potential function in the Schrödinger's equation, which is used to calculate the vibrational wave functions, is assumed to be parabolic (restoring force linear in displacement, though one never explicitly deals with the force when solving the Schrödinger equation) one gets harmonic oscillator wave functions and simultaneously equi-spaced energy levels. If a more realistic potential is used then (restoring force is non-linear) one gets anharmonic oscillator wave-functions and energy level spacing decreases with increasing vibrational quantum number. To be strictly consistent both these effects of mechanical anharmonicity must be included simultaneously. However, one sometimes uses correct (accurate) energy levels (often determined experimentally rather than from a solution of the Schrödinger equation) but retains the analytical form of the harmonic oscillator matrix elements when computing the vibrational quantum number dependence of the Raman scattering. This hybrid approach, though strictly inconsistent, is common (especially in low temperature Raman spectroscopy).

The induced dipole arising from the second term in eqn. (1.3) can be written as

$$\begin{bmatrix} P_x \\ P_y \\ P_z \end{bmatrix} = \begin{bmatrix} \alpha'_{xx} & \alpha'_{xy} & \alpha'_{xz} \\ \alpha'_{yx} & \alpha'_{yy} & \alpha'_{yz} \\ \alpha'_{zx} & \alpha'_{zy} & \alpha'_{zz} \end{bmatrix} \xi . \begin{bmatrix} E_x \\ E_y \\ E_z \end{bmatrix}. \tag{1.5}$$

Polarizability is a tensor as it depends on two directions. The matrix representation of the first derivative of the polarizability is called the derived polarizability matrix. From eqn. (1.5) it is clear that even when the incident light is only polarized in one direction, say its electric field is described by [0, 0, E_z], the scattered light can be polarized in any direction based on the pattern of entries in the derived polarizability matrix. The values of the elements of the derived polarizability matrix are calculated by using eqn. (1.4).

The polarizability in all three directions is also often represented by a polarizability ellipsoid, which is a 3D plot of $1/\sqrt{\alpha_i}$ for an electric field applied in a specific *j* direction. For example, when the electric field is oriented along the bond of a diatomic molecule the polarizability ellipsoid is elongated perpendicular to the bond and the minor axis of the ellipsoid is along the bond. When the electric field is oriented perpendicular to the bond the polarizability ellipsoid is a sphere. A molecule is vibrationally Raman active if the size, shape or orientation of the polarizability ellipsoid changes between the two extremes of the vibrational motion. For example, the symmetric stretch mode of H_2O is Raman active because of the change in the size of the polarizability ellipsoid, but the bending mode is Raman active because of the change in the shape of the polarizability ellipsoid, and the anti-symmetric stretch is Raman active because of the change in orientation of the polarizability ellipsoid. In polyatomic molecules group theory is used to predict the Raman activity.

The ratio of scattered light polarized perpendicular to the incident polarization and polarized parallel to the incident radiation is called depolarization ratio ($\rho = I_\perp/I_\parallel$). In the case of N_2 $\rho = 0.75$ for the *O* and *S* branches (notation is described subsequently) and $\rho \ll 0.75$ (depends on the rotational level) for the *Q* branch which indicates that the *Q* branch is strongly polarized and the *O* and the *S* branches are strongly depolarized.

Raman scattering results in transitions between vibrational and rotational levels. The lines in the spectrum are labeled to indicate the transitions. If the scattered light has lower frequency (red-shifted) than the excitation frequency then it is called the Stokes signal ($\Delta v \equiv v_f - v_i = +1$, for vibrational Raman, where subscripts *f* and *i* represent final and initial states respectively). If the scattered light is at higher frequency (blue-shifted) then it is called the anti-Stokes signal ($\Delta v = -1$, for vibrational Raman). The

expressions given in Long's book[10] [24] are for Stokes scattering and one should be cautious in using them to model anti-Stokes scattering. The change in rotational state is represented by $\Delta J = J' - J"$, where J' represents the rotational state of the higher energy level and $J"$ represents the rotational state of the lower energy level. Transitions that correspond to $\Delta J = +2$ are labeled as the *S* branch, $\Delta J = 0$ as the *Q* branch and $\Delta J = -2$ as the *O* branch. It implies that in pure rotational Raman scattering there are only Stokes and anti-Stokes *S* branches as the transitions occur within the same vibrational level. The transition $J \rightarrow J + 2$ is labeled as the *S* branch in the Stokes band and as the *O* branch in the anti-Stokes band. Similarly, the transition $J \rightarrow J - 2$ is labeled as the *O* branch in the Stokes band and as the *S* branch in the anti-Stokes band. Transitions corresponding to the *P* ($\Delta J = -1$) and *R* ($\Delta J = +1$) branches are not observed in the Raman spectrum of the diatomic molecules.

1.3 MOTIVATION

The importance of Raman spectroscopy simply cannot be overstated. It is mostly applied in pharmaceutical industry, food and agriculture industry, forensic analysis, carbon analysis, gemology, art and archaeological analysis, bioscience and medical diagnosis, etc. The Raman spectrum is like the finger print of the scattering species as it can be used to identify them. It can also be used to infer their temperature and concentration. However, Spontaneous Raman Scattering (SRS) has a very small cross section. The ratio of the number of Raman signal photons to the incident excitation

[10] The book is a very good resource, but it does not provide the complete theory. In particular, the vibrational parts of the polarizability matrix elements, which contribute to the transition intensities, have been calculated assuming a harmonic oscillator. In flames higher vibrational states are also populated and so the transition intensities should be calculated assuming an anharmonic oscillator. The theory given in the book also does not account for the contribution of the interaction between vibration and rotation on the transition intensities. This effect is accounted for by the Herman-Wallis factors. The first edition of the book also does not describe the angular dependence of Raman scattering; however, it is covered in its latest edition [25].

photons is very small. For instance when pressure P = 1 atm, temperature T = 2000 K, excitation wavelength λ = 532 nm and collection solid angle Ω = 0.03 Sr (f/5) the ratio of Raman photons from nitrogen to the excitation photons is $6 \times 10^{-14} l \in q$, where l is the probe length, $\in$ is the transmission efficiency of the optics and q is the quantum efficiency of the detector.

So, it is most desirable to enhance the Raman signal. This has led to the development of sophisticated Raman techniques like Stimulated Raman Scattering, Coherent Anti-Stokes Raman Scattering (CARS), Resonance Raman Scattering, Surface Enhanced Raman Scattering and their variations. Not all of these methods can be applied in flame diagnostics. The signal from flame is also weaker because of low sample density for the same pressure. CARS is widely used in combustion experiments; however, as mentioned earlier although it can yield strong signal and accurate temperature measurements, it is complicated both in set-up and the interpretation of data.

In the afore-mentioned Raman methods, the probability of scattering is amplified for any given interaction between the radiation and the molecule. In this research, we explore the application of a simpler technique in which scattering is not enhanced for a given interaction between the radiation and the molecule, but the enhancement of SRS is achieved by making the same laser pulse interact with the sample multiple times. The SRS signal is linearly proportional to the energy of the incident radiation so repeated interactions of the pulse with the sample effectively amplifies the pulse energy and thus amplifies the signal proportionally.

The greatest advantage of using a multiple-pass cell is that it can deliver the performance of a laser with high pulse energy (few hundred mJ per pulse) using a laser with relatively low pulse energy (few mJ per pulse). In CARS and SRS experiments the lasers with high energy and short pulse give high pulse power, which can cause laser

induced breakdown of the sample and affect the sample properties. This will be particularly obtrusive in the study of flames in which plasma is used to reduce ignition temperature and increase combustion efficiency [33, 34]. The breakdown is typically prevented by including a pulse stretcher along the laser's optical path [35] and also by defocusing the laser. In the multiple passing of a low energy pulse, the breakdown is avoided as high excitation energy can be deposited in the probe region while maintaining low local energy density as the beams do not completely overlap one another at the focal region. In contrast to a low pulse energy laser, a high pulse energy laser can also damage the optical components.

1.4 STATE OF THE ART

Since August 2012 alone, new Raman instruments have been released by companies like Ocean Optics, Bruker, CRAIC Techologies, DeltaNu, Cobalt Light Systems, Horiba Scientific, Centice Corporation, B&W TEK. Most of the new instruments are based on some type of surface enhanced Raman scattering method. Other companies who already have their commercial Raman instrument in the market are Rigaku, Reinshaw, BaySpec, PerkinElmer, Process Instruments, Thermo Scientific, B&W TEK and Agiltron. So, although the signal is weak, Raman spectroscopy is rapidly becoming an everyday technique. However, most of these instruments are only used for species identification and not for quantitative measurements.

None of the afore-mentioned instruments include a multiple-pass cell. Multiple-pass cells have been used to enhance Raman signal in several lab based experiments. A retro-reflecting multipass light cell, which enhances the signal gain by 15 times, was used for Raman thermometry of premixed methane air flames [26]. The sample volume was 6 mm wide, 1.1 mm deep and 0.2 mm high. An effective signal gain of 20 times can be

obtained in a multiple-pass cell which was demonstrated with Stimulated Raman Scattering of H_2 gas [27]. More recently, the multiple-passing concept was applied as silver coated capillary cell to enhance Raman signal from CO_2 and CH_4 by up to 20 times [28]. Multiple-passing was also used to generate CARS signal in flame from as many as nine points simultaneously [29]. A multiple-pass cell, which is similar to the one reported in this paper, with signal gain of ~45 was also employed for the detection of trace gas in transformer oil [30]. In this paper, it is not clear if the specifications of the cell are determined experimentally or computed. The light is focused at two foci and they claim that the separation between the foci is 0.2 mm, but it is not stated how the separation between the foci was measured. A sample cell for a multiple-pass cell has also been proposed for non-flame environments [31].

This dissertation describes the development and application of multiple-pass cell to amplify the Raman signal gain by about a factor of 80 from room air and flames. The sample volume was a ring of about 3.5 mm diameter and it was 0.2 mm long (set by the spectrometer slit width). Later some of the signal gain was traded off for a dramatic increase in the spatial resolution and the capability to do simultaneous measurements at two well separated points. The total signal gain at each point or focus in the new alignment is 20 and each focus is about 0.2 mm long (set by the spectrometer slit width) and has a diameter of about 0.3 mm. The data are analyzed to calculate the temperature of flames by curve fitting with detailed simulation of Raman spectra. The sources of uncertainty and the magnitude of the error that they cause are also identified.

1.5 OVERVIEW

Chapter 2 describes the experimental set-up. It also includes a detailed explanation of how a multiple-pass cell works and presents the results from ZEMAX

simulations. The simulations helped to understand the performance of optics and also to test various possible ways to align the multiple-pass cell. The wavelength, intensity and flow meter calibrations and the determination of polarization sensitivity of the collection optics is presented in Chapter 3. In chapter 4, the details of the Raman simulation are given. The simulation is used to calculate the temperature of the flame from the Raman spectrum of nitrogen in the flame. The signal and signal to noise ratio (SNR) gain obtained by using the multiple-pass cell in the two alignment modes are described in Chapter 5. The calculations of temperature from low and high resolution Raman spectra using various methods are presented in Chapter 6. Chapter 7 concludes the thesis and also includes recommendations for future work.

The appendices provide supplementary information. Appendix A contains the details on the calculation of thermocouple radiation corrections. Appendix B contains the derivation of the angular dependence of Raman scattering from a beam along the axis of the multiple-pass cell and also a beam at an angle to the axis of the cell. The plots of the final expressions reveal that it is very important to include the angular dependence in the model particularly when the data is collected at low f/# (possible in microscopy based Raman techniques). Appendix C illustrates the straight forward extension of Raman code for N_2 to H_2. It also highlights the importance of the anharmonic terms in the simulation of lighter molecules. Appendix D contains notes on the units of polarizability derivatives and their conversion into one another. In Appendix E the design of a Raman gas sample cell is provided for future multiple-pass Raman experiments on non-flame media.

Chapter 2: Experimental Set-Up

The experimental set-up was modified over the course of the project. Initially collection optics was imported from a project on Rayleigh scattering. This set of collection optics is described in detail later. The laser was Corona 10 kHz multimode laser with 150 ns pulse width and 6 mJ pulse energy. A PMT was used as the detector. The spectrograph was Triax320. The mirrors were 50.8 mm in diameter and about 30 passes were obtained. The set-up was then modified. To enable measurements of Raman spectra of several species simultaneously the PMT was replaced with a Newport 78105 CCD detector which was mounted on a Newport 74050 spectrometer. The raw survey spectrum obtained using the updated detection system over 30 s of integration time is shown in Fig. 2.1.

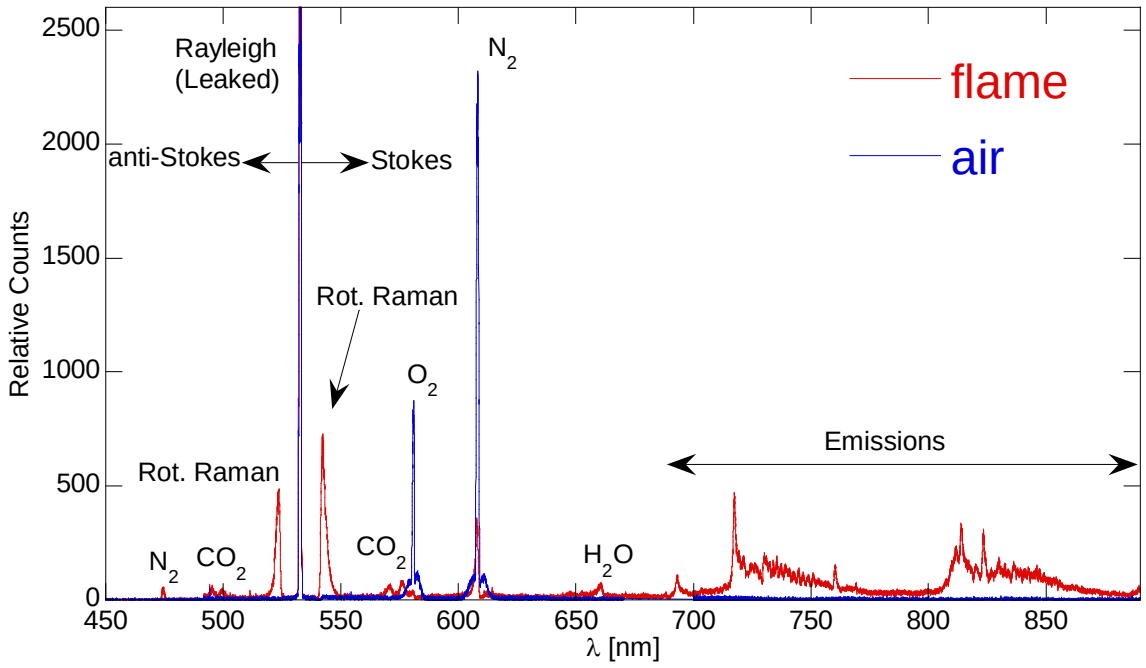

Figure 2.1: Survey spectrum obtained from room air and flame using the old set-up

However, all of the quantitative results reported here are obtained from a new set-up. The experiments were carried out in two separate modes of alignment. In the first alignment mode, the probe region is shaped like a ring; and in the second alignment mode, the probe region has two well separated points.

2.1 THE MULTIPASS PULSE

In both the alignment modes multiple passing of the single pulse leads to the generation of an effectively higher energy pulse. The generation of an effective pulse by multiple passing of a single pulse is explained as follows. For definiteness I use the parameters of the laser and the cell used for our experiments. The laser pulse has a Gaussian intensity profile with 12 ns FWHM. Suppose the laser operates at 100 Hz so the pulses are separated by 10^7 ns. An effective pulse as a result of multi-passing a 12 ns FWHM Gaussian pulse 100 times through a 400 mm long cell is shown in Fig. 2.2. The reflectivity, R of the mirrors is assumed to be 1. The calculation was performed in MATLAB. The amplitude of the single pulse is unit normalized. The area under the intensity profile is the energy of the pulse which is 6 mJ.

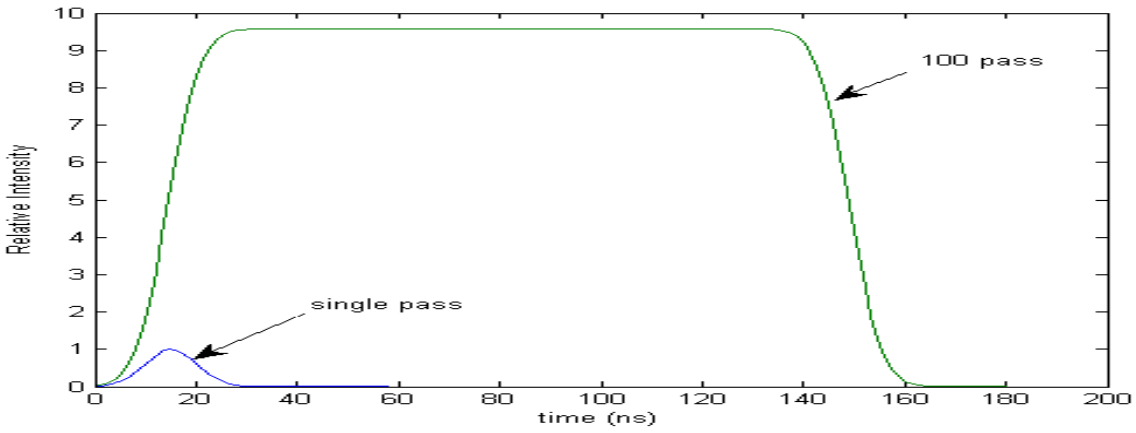

Figure 2.2: Single pass pulse and 100 pass pulse from a Quantel CFR200 laser in a multi-pass cell

In a single pass there are no mirrors and the pulse simply propagates through the observation region. The shape of the effective pulse can be understood in the following way. Consider Fig. 2.3. Assume that at time t_1 intensity A is observed at the center of the cell. The cell is about 400 mm long so about 1.3 ns after t_1, because of the propagation of the pulse, intensity B is at the center of the cell; however by this time intensity A has reflected from the rear mirror and again reached the center of the cell. The effective intensity is the sum of A and B. At $t_1 + 2 \times 1.3$ ns, intensity C reaches the center of the cell. A and B have also reflected back from the rear and front mirrors respectively and reached the center. The effective intensity at $t_1 + 2 \times 1.3$ ns is therefore $A + B + C$. In this way, the intensity of the effective pulse increases until the entire length of the original pulse passes through the center. Once the entire pulse passes through the center, each point on it reflects from the mirrors and comes back to the center after an interval of every 1.3 ns and so the intensity of the effective pulse stays constant. Eventually on the final pass the effective pulse begins to leave the cell and so the intensity falls.

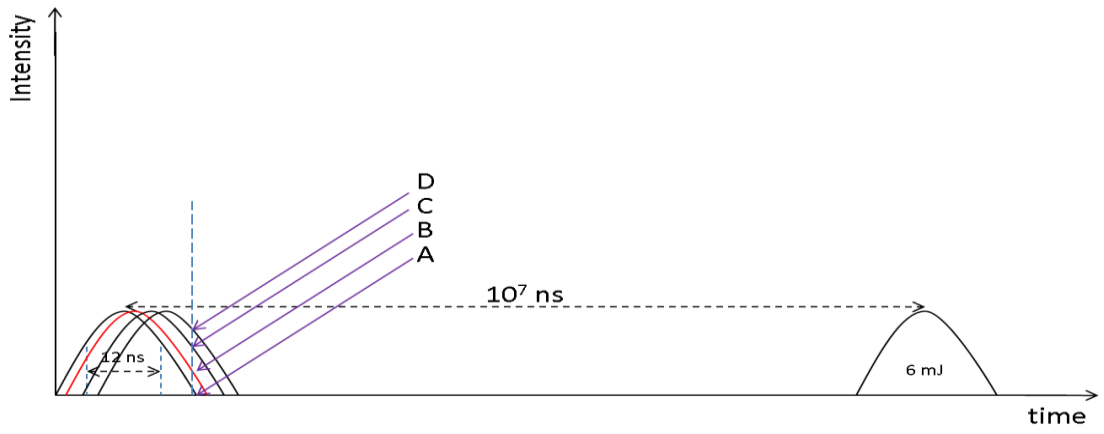

Figure 2.3: Pulse stretching process

The effective energy of the multipass pulse is highly sensitive to mirror reflectivity. By using the trapezoidal method to calculate the area under the curves, we

find that the energy incident on the focal volume from a 100 pass effective pulse in Fig. 2.2 is ~100 times the energy incident from a single pulse. Figure 2.4 shows the results of the calculations of the intensity profile of the effective pulse at various values of mirror reflectivity. For the set of less reflective mirrors, the relative intensity drops over time as some of the energy is lost in the mirrors upon each reflection. The ratio of area under the curve corresponding to $R = 1$ to the area under the curve corresponding to $R = 0.9$ is 10. Multipassing is not a new concept. It was demonstrated in the 70's and the 80's. However, at that time the highly reflective mirrors were not readily available. Now they can be acquired at a reasonable price. The reflectivity of the mirrors used in our set-up is specified to be 0.997. When the reflectivity is 0.997 the area under the effective pulse is ~87 times the area under the single pulse. Walderr and Linn [32] also give a detailed explanation of how a more energetic effective multiple-pass pulse is generated from a single pulse in a multiple-pass cell.

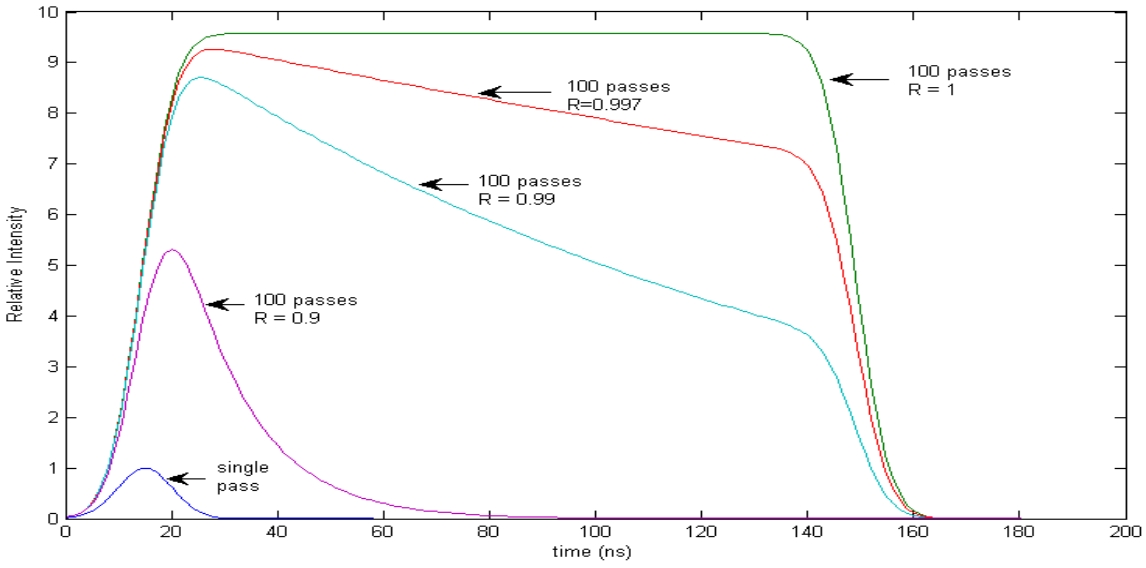

Figure 2.4: Effective pulse in a 100 pass cell when the reflectivity is varied

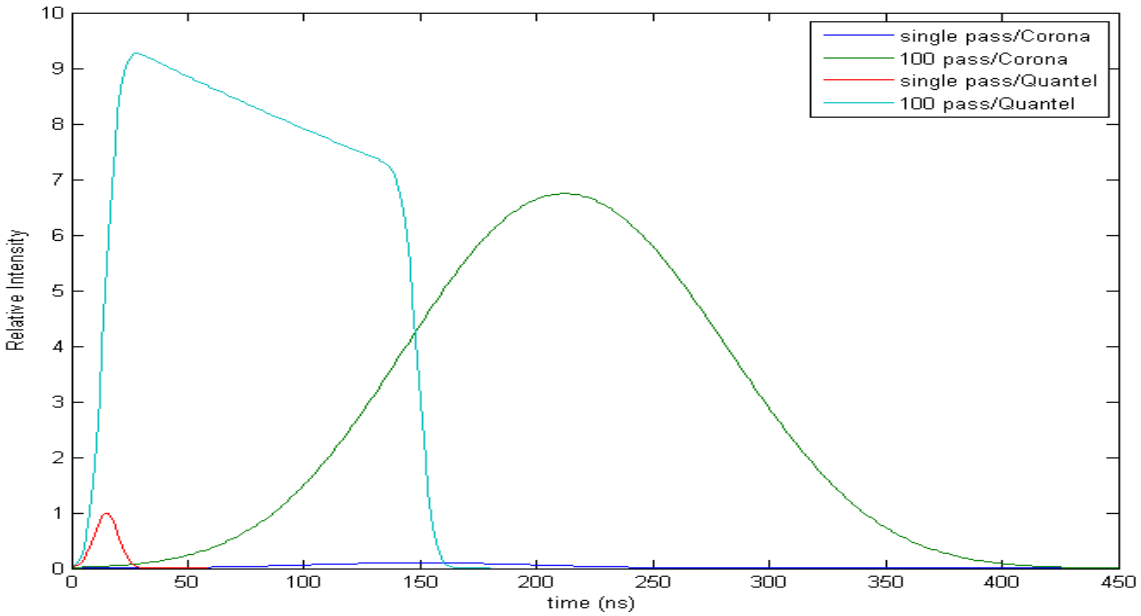

Figure 2.5: 120 ns wide pulse (Corona) and 12 ns wide pulse (Quantel) inside a multi-pass cell

The width of the single pulse also affects the quality of the effective pulse. Figure 2.5 shows 120 ns FWHM single pulse (labeled Corona after the name of the second laser at our disposal) and its effective pulse after 100 passes. Since high energy is maintained for a longer time with the effective pulse from the Quantel we expect it to generate higher SNR than the effective pulse from Corona (another advantage of the Quantel laser over Corona is that the former has Gaussian beam mode which is easier to focus tightly than the multimode beam profile of the latter). In this way, the use of highly reflective mirrors and shorter pulse lasers can improve the performance of a multiple-pass cell.

Now, each alignment mode is described in detail.

2.2 THE RING MODE

In the ring mode the multiple-pass cell was aligned to focus the multiple passes of the laser to a ring like structure at the center of the cell. Raman spectra were recorded in the low dispersion mode so as to capture both Stokes and anti-Stokes signals

simultaneously on the array detector. Temperature was determined by comparing the Stokes signal from N_2 with its anti-Stokes signal. A schematic layout of the set-up is illustrated in Fig. 2.6. A frequency-doubled, flashlamp-pumped, Q-switched Nd:YAG laser (Quantel CFR200) with a TEM_{00} output provides 532 nm light at 100 pulses per second. Each pulse is 6 mJ in energy with a nominal full width at half maximum (FWHM) intensity of 12 ns. The beam diameter at the laser is ~1.5 mm with a divergence of 1.5 mrad. This light passes through a polarization rotator/polarization beam splitter pair that directs the light into the multiple-pass cell or into a beam dump. When the polarization is adjusted to dump the light, the overall extinction ratio of the beam splitter leaks about 1-2 mW of light into the multiple-pass cell, permitting a safe source of light for initial alignment.

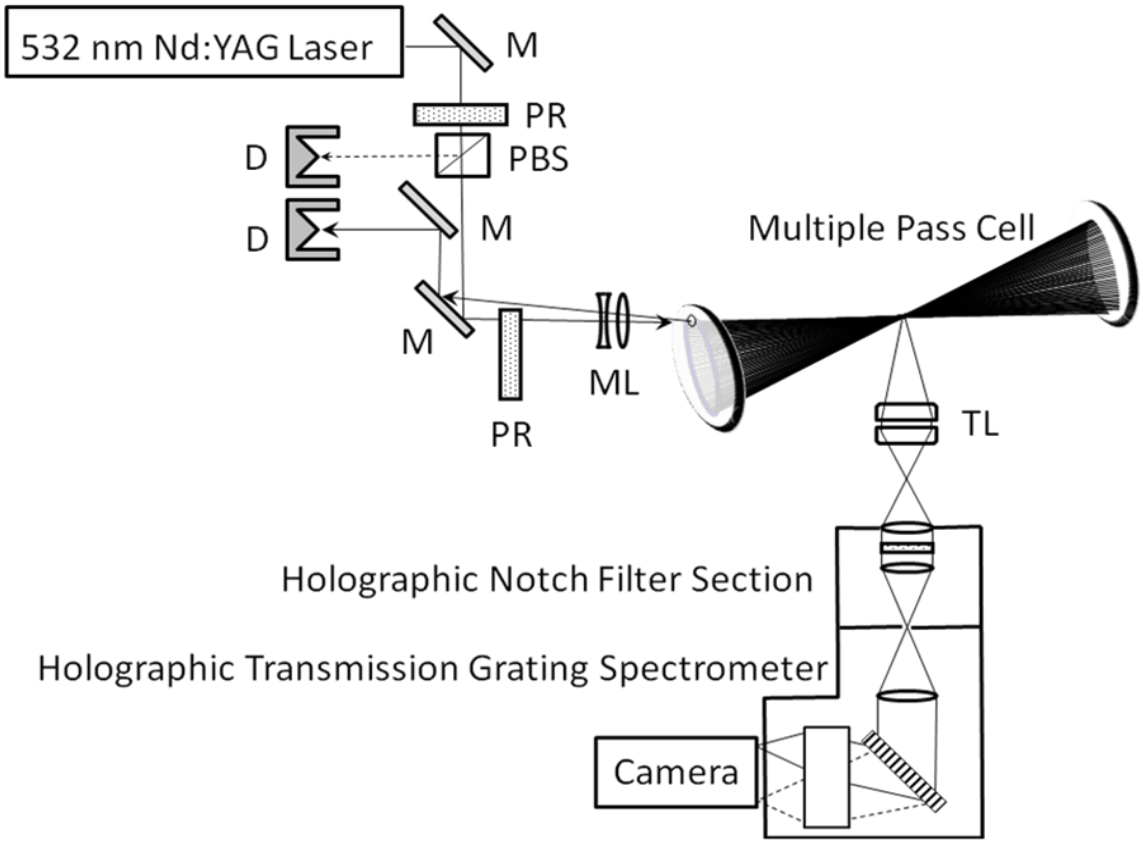

Figure 2.6: The experimental set-up in the ring mode. D = beam dump, M = mirror, PR = polarization rotator, PBS = polarization beam splitter, ML = mode-matching lens pair, and TL = image transfer camera lenses [36]

The main beam passes through a bi-concave and bi-convex pair of lenses with adjustable separation and position that expand the beam and focus it at the center of the cell appropriate to the requirements for mode-matching. The alignment of these lenses was simulated in ZEMAX, where the relative orientation of the optical components was optimized to minimize the spot radius at the center of the cell. All laser optics is coated for high power operation at 532 nm.

A pair of matched 101.6 mm diameter, 100 mm focal length mirrors forms the multiple-pass cell. These mirrors have a dielectric coating for greater than 99.7%

reflectivity at 532 nm, and are mounted in Newport 600-A precision kinematic mounts using 100 TPI micrometer adjusters. The rear mirror mount is attached to a translation stage that also has a 100 threads per inch micrometer with a 2-inch travel range. A 4 mm wide slot at the outer edge of the input mirror allows the beam to enter and exit the cell.

A second polarization rotator is located just before the focusing lens pair to control the polarization of the beam incident on the cell so that Raman scattering occurs in the direction normal to the cell axis and into the collection optics. Experiments confirm that all passes through the cell retain the same polarization.

The beam exits the cell at a slightly different angle than which it entered, and is eventually picked off by a small mirror and directed into a beam dump to safely collect the light. For eye safety, most of the optics outside the cell is enclosed in a colored acrylic box having an optical density OD > 4 at 532 nm.

Raman scattered light is collected with camera lenses. We used two stock Nikon camera lenses (Micro Nikkor, 105 mm, f/2.8 followed by a Nikkor, 50 mm, f/1.4) to provide good collection efficiency while minimizing chromatic and spherical aberration and matching the f/# to the spectrograph used to disperse the Raman signal. The working f/# of the collection optics is ~f/5.9 and the collection system magnification is 0.52. The magnification is determined by imaging light from a hole of known dimensions and comparing the hole size with its image size. The magnification was determined more carefully later as described in section 2.3. In the ring mode, the collection f/# was determined directly by measuring the diameter of the lens and the distance between the probe region and the surface of the lens. This is not the best way to determine the collection f/# as not all the light that hits the front surface of the collection optics is transmitted into the spectrograph. Since the slit width is 100 μm and the magnification is 0.5, scattering is recorded from 200 μm wide region in the focal volume. The depth of

field of the collection optics is 4.6 mm. It was determined by translating one end of a 200 μm optical fiber along the optical axis and recording the 546 nm line from a mercury calibration lamp placed near other end of the fiber.

A Kaiser Optical Instruments Holospec HS-f/1.8i-VIS spectrometer is used as the dispersion system. Raman scattered light is imaged through the entrance aperture and sent into the pre-filter section of the spectrograph, where it is collimated and filtered by a holographic notch filter. This filter has an OD > 6 at 532 nm with a FWHM transmission width < 350 cm^{-1} and a passband transmission efficiency > 90 %. The Raman emission that passes through the filter is then imaged through the entrance slit of the spectrometer. This unit uses a volume-phase holographic transmission grating matched to the spectral range required for simultaneous observation of the Stokes and anti-Stokes Raman signals. The grating has higher throughput than comparable refractive gratings. For the experiments in the ring mode we used an HFG-539.5 grating, which has a nominal spectral coverage from 411.4 to 667.6 nm and linear dispersion of 10 nm/mm. When used in conjunction with a detector array with 26 μm pixels, this gives a linear dispersion of 0.26 nm/pixel.

A Princeton Instruments PI-MAX3 1024×256-HBf-P43 front-illuminated intensified CCD camera is mounted at the image plane of the spectrometer. It has a 1024×256 CCD array with 26 μm × 26 μm pixels and digitization rates up to 2 MHz. The array is connected via a 1:1 fiber-optic bundle to an 18 mm diameter Gen III filmless image intensifier with an extended blue response photocathode and a P43 phosphor. The photocathode has a peak quantum efficiency of 51% at 476 nm. In the spectral range of interest, 465 to 620 nm, the quantum efficiency is above 40%. Because the intensifier is smaller than the detector array width, only 692×256 pixels of the detector array are

active. The intensifier is effective over the full 256 pixels height (y) of the array for 645 pixels (pixels 204 – 848).

The size of the focal ring is about 2.5 mm according to the simulations of the cell performed in ZEMAX, although in practice we operate it at ~3.5 mm diameter. It is very complicated to simulate the multiple-pass cell in the sequential mode of ZEMAX and so the simulation was performed in the non-sequential mode. The non-sequential mode is not available in the Standard Edition (SE) so the software was upgraded to the Engineering Edition (EE). At the time of the upgrade Physical Optics Propagation (POP) was not available in the non-sequential mode so the propagation of light in the simulation follows ray optics. The goal of the simulation was to analyze the overall shape and size of the probe region and later on, to discover additional alignment modes of the multiple-pass cell, so it was not absolutely necessary to obtain an accurate image of every pass at the location of the detector.

The lenses used in the telescope can be loaded in the sequential mode, but they have to be converted to non-sequential mode to combine the lens surfaces and express them as a non-sequential object. The parameters of the optical components in the simulation are specified to represent the reality. The set-up is shown in Fig. 2.7a and b. The laser beam is specified to have a Gaussian ray distribution. The diameter of the beam at the source is 1.5 mm and the divergence is 1.5 mrad. The beam propagates 50 mm before it hits the plano concave lens. The specification of the slot through which the beam enters the multiple-pass cell also matches its actual dimensions. In Fig. 2.7a the small rectangle at the center of the cell, which is more noticeable in Fig. 2.7b, is a false optical component. It is a detector which is set to record the intensity of the incident light on both sides. It does not interfere with the ray propagation. The rectangle behind the rear mirror

is also a false optical component which is in place so that the lay out will draw the rays in case they miss the rear mirror.

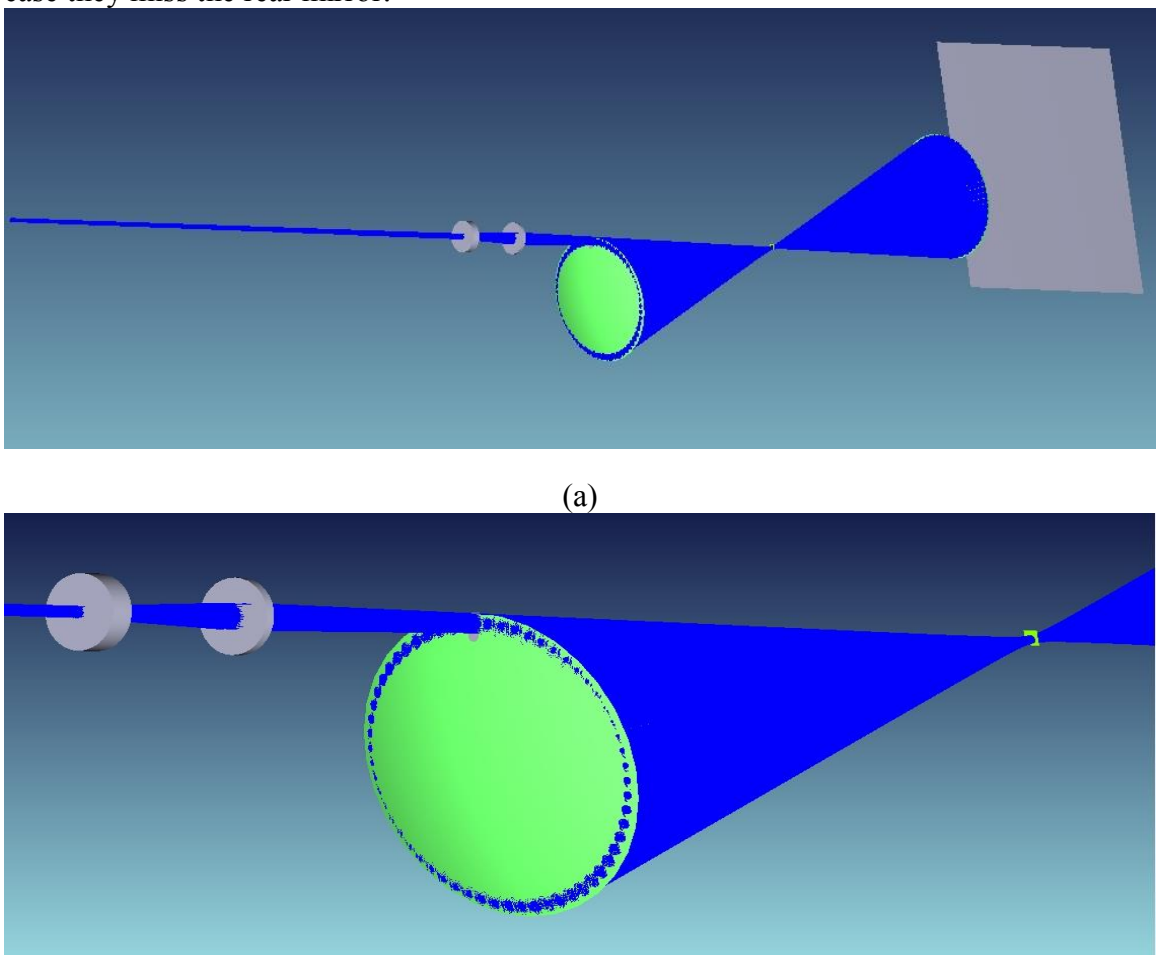

(a)

(b)

Figure 2.7: (a) Simulation of the multiple-pass cell in the ring mode, (b) and the close-up view of the mode matching telescope, front mirror and the probe region.

The layouts in Fig. 2.7 are generated by launching 1000 rays from the source; however the analysis is carried out with 10000 rays. The data recorded by the detector at the center of the cell is shown in Fig. 2.8. It can be inferred from Fig. 2.8 that in this simulation 134 passes were obtained. The profile along the central vertical column of the

plot shown in Fig. 2.8 is shown in Fig. 2.9, which indicates that the ring at the center is about 2.5 mm wide.

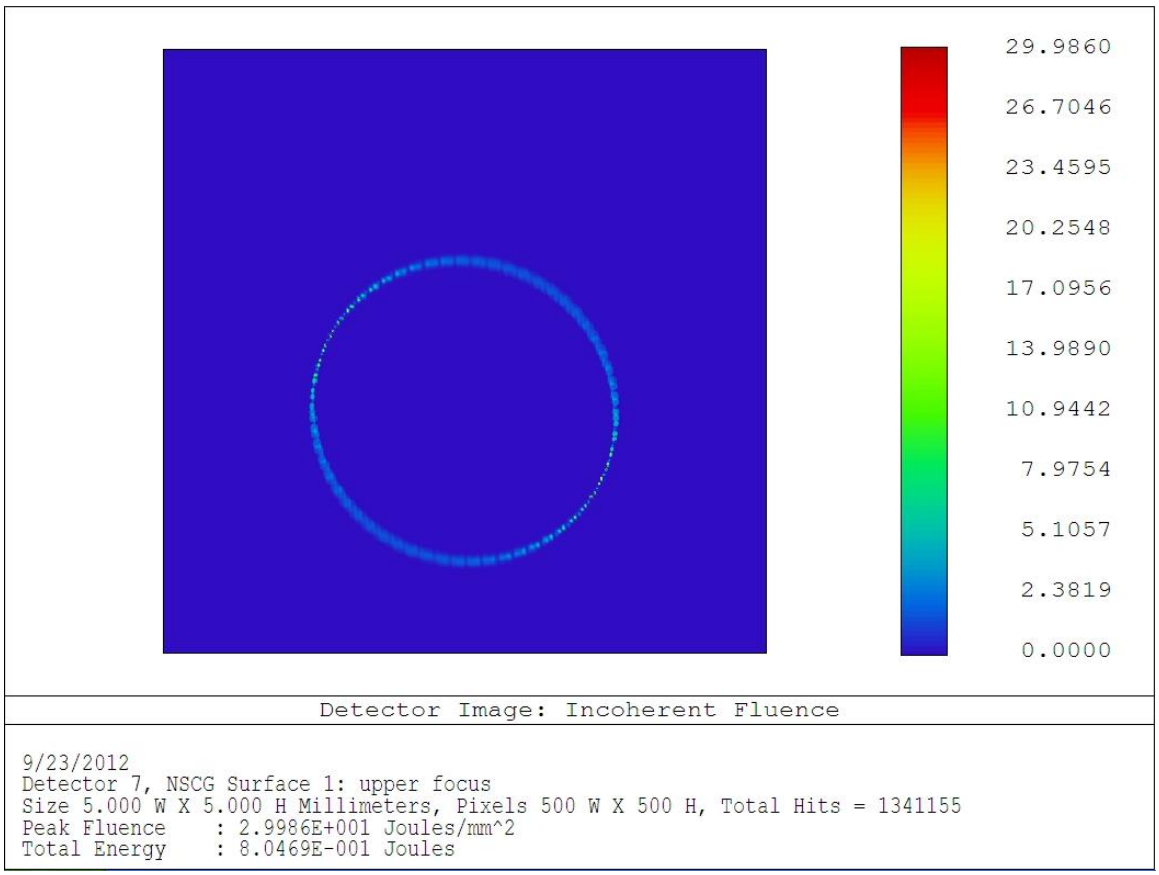

Figure 2.8: Fluence profile at the center of the cell. 10,000 analysis rays were launched from the source and the detector was hit 1341155 times indicating that 134 passes were obtained.

Now, the simulations of Rayleigh collection optics that was initially used to collect Raman signal are described as important lessons were learned from them. The raw Raman data were acquired without significant struggle. However, the values of temperature inferred from the calibrated spectra were much lower (~1400 K) than their expected value (~2000 K). Finally the simulations in ZEMAX revealed that our collection optics had chromatic aberration. Since the inception of the project, we were

imaging 473 nm and 607 nm with optics which was optimized for 532 nm and not corrected for chromatic aberration.

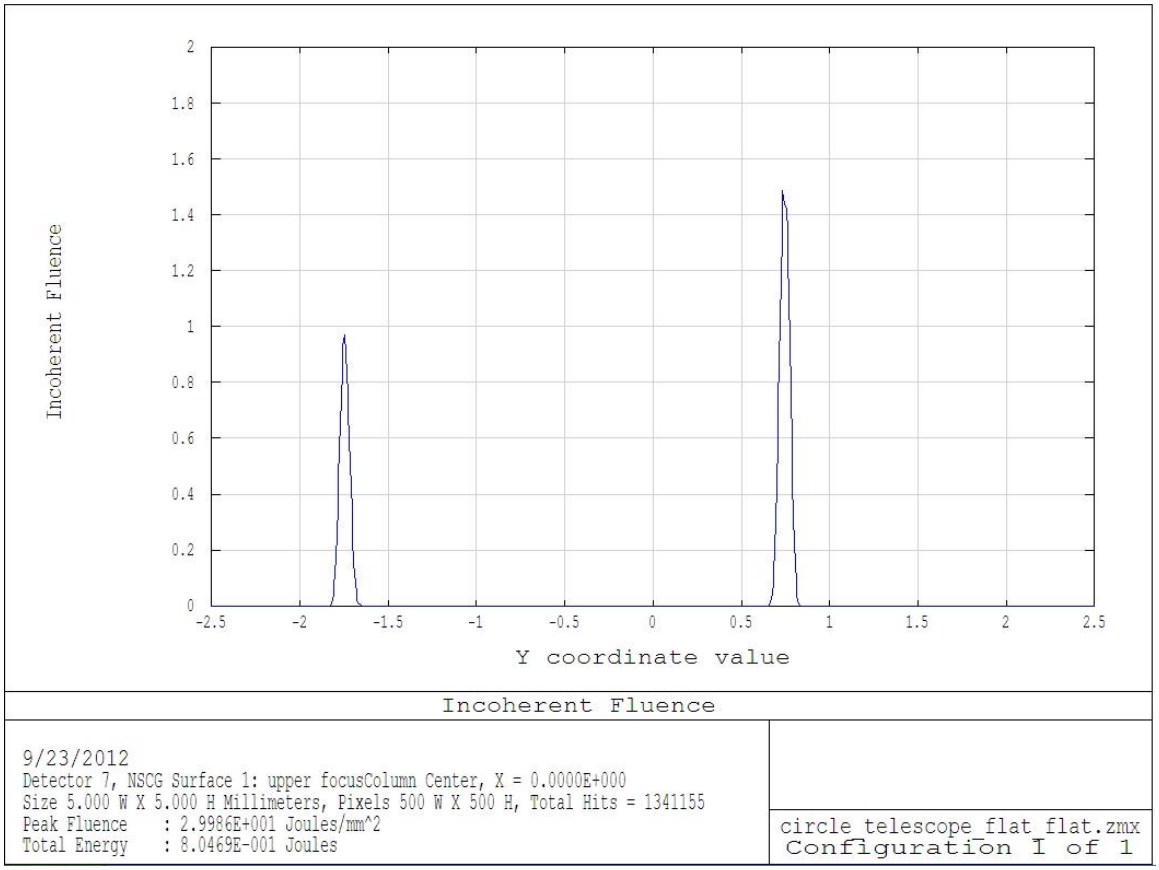

Figure 2.9: Fluence profile at the center of the ring, which shows that the ring is 2.5 mm in diameter.

The alignment of the Rayleigh collection optics was optimized in the simulation to minimize the spot size of the point source. The alignment is shown in Fig. 2.10. The 3 colors represent the light radiating from the 3 point sources. The off-axis point sources are at 1.5 mm from the axis. Each off axis source is given a weighting of 1 and the on axis source is given weighting of 2 for optimization. The optimization is carried out for 532 nm. The default merit function is used and Rectangular Array is selected for pupil

integration method because circular aperture was defined for each optical component. The lenses are two pieces of 01LPX311 plano convex lens, 01LMN011 meniscus and 01LDX179 biconvex lenses available from CVI Melles Griot, and they can be directly loaded in the simulation from the lens catalog in ZEMAX.

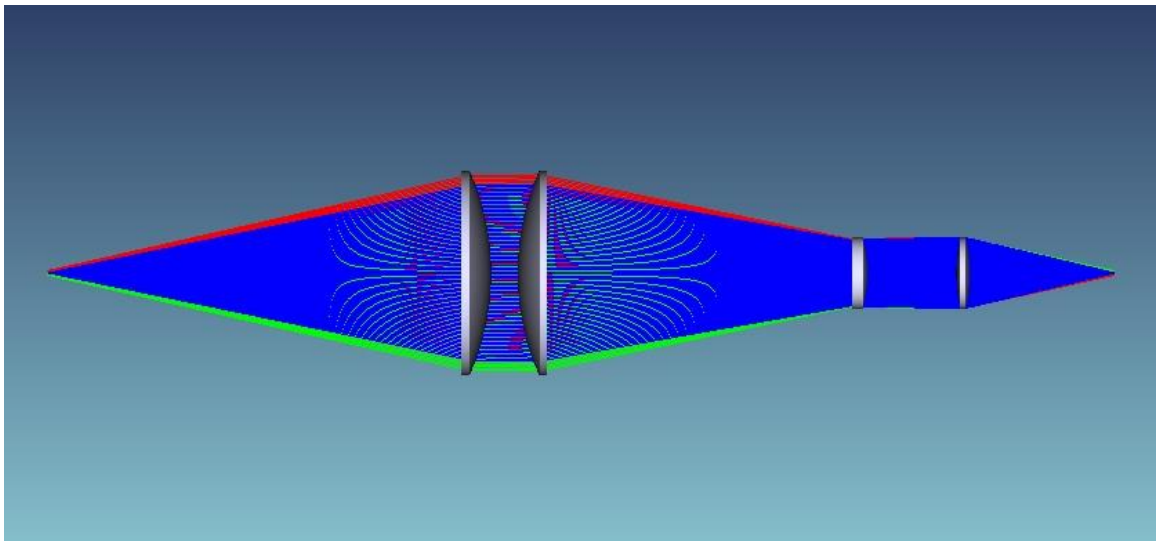

Figure 2.10: Optimized alignment of Rayleigh optics

The spot diagrams of the on-axis and off-axis point sources are shown in Fig. 2.11. The spot diagrams represent the distribution of the intensity of the point sources on the image plane. The sizes of the spots are listed in Table 2.1. The simulation accounts for ray aberration, but not for diffraction effects. Diffraction effects are included when the spot diagram is represented as a Huygens Point Spread Function (PSF). However, in the case of Fig. 2.11, the geometric spot is significantly larger than the Airy disk, which is the diffraction limited spot size, so we can assume that the point spread caused by diffraction is negligible compared to the other effects.

In Table 2.1, the mid-point of the spot cluster at a given wavelength is taken as the reference to calculate the linear dimensions. The root mean square (rms) radius is

calculated by taking the square root of the average of the square of the difference between the reference point and each point. GEO radius is the maximum difference between the reference point and the ray.

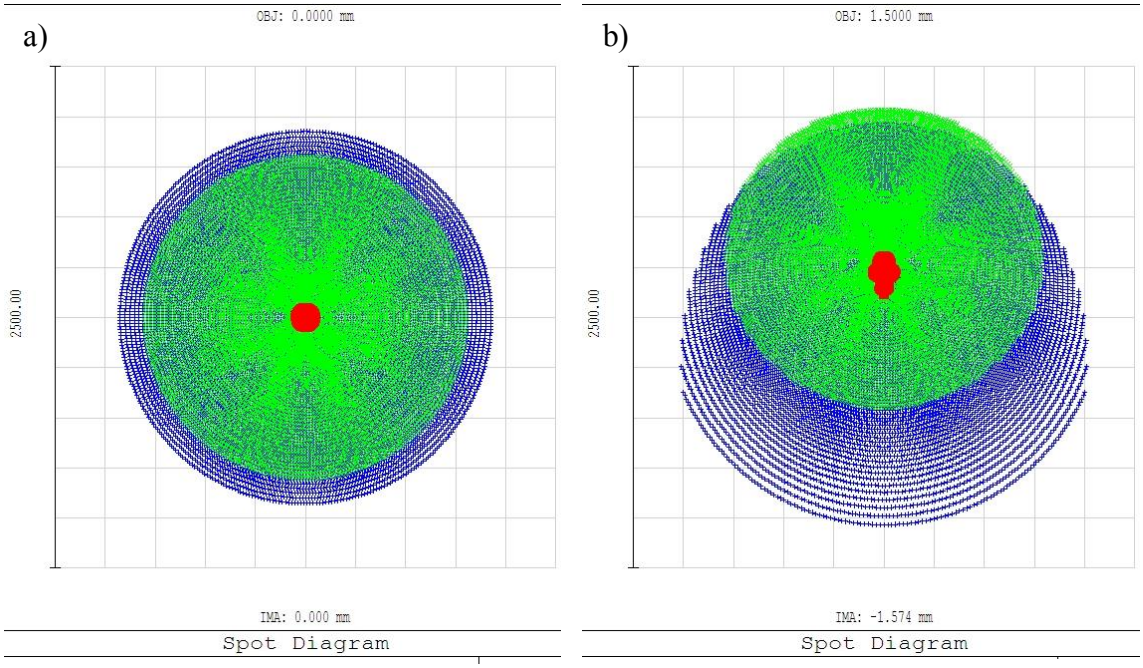

Figure 2.11: Spot diagrams of (a) on axis sources and (b) off axis sources. Red is 532 nm, green is 607 nm and blue is 473 nm.

The chromatic aberration is such that if the optics is aligned to maximize 532 nm or 607 nm then significant proportion of the signal at 473 nm does not enter through the slit of the spectrograph. In this way, the intensity of the anti-Stokes signal is underestimated and lower value of temperature is obtained. So, the Rayleigh optics cannot be used without chromatic aberration correction when the goal is to compare the relative intensity of anti-Stokes and Stokes signal. However it is very desirable to have lenses with larger aperture to collect as much Raman signal as possible. The plano convex lens facing the sample has a diameter of 6 inches. Simulations were carried out to

estimate the performance of this collection optics if it were to be used to acquire a high dispersion Stokes spectrum from nitrogen, in which the spectral coverage is over a restricted range.

Table 2.1: Characteristics of the geometric spots optimized for 532 nm at Stokes and anti-Stokes wavelengths of N_2

On-axis				
λ [nm]	RMS radius [μm]	GEO radius [μm]	Airy radius [μm]	Location [mm]
473	628.7	926.5	1.11	0.00
532	37.5	60.5	1.25	0.00
607	519.7	800.6	1.43	0.00
Off-axis				
λ [nm]	RMS radius [μm]	GEO radius [μm]	Airy radius [μm]	Location [mm]
473	693.5	1071.5	1.11	-1.62
532	56.1	106.7	1.25	-1.36
607	497.3	789.9	1.43	-1.28

The spot diagrams of the off-axis and on-axis sources are shown in Figs. 2.12 and 2.13, respectively. The alignment was optimized for 607 nm. The PSF of the on-axis sources are also shown as they are more informative about the distribution of intensity in the image plane. The PSFs of the off axis sources were not computed as they do not pass the FFT validity test (i.e. for FFT PSF to be accurate the distribution of rays in the cosine space should be uniform). The Huygens PSF was not computed as it takes a lot of memory and time. For our purpose even the geometric spot diagram is adequate to show the aberrations. The characteristics of the spots based on the geometric spot diagrams are tabulated in Table 2.2. There are substantial aberrations if the Rayleigh optics are used even in a restricted spectral range so the collection optics was set up using camera lenses, which are spherical and chromatic aberration corrected.

Table 2.2: Characteristics of geometric spots optimized for 607 nm in a restricted spectral range

On axis				
λ [nm]	RMS radius [μm]	GEO radius [μm]	Airy radius [μm]	Location [mm]
595	65.0	86.1	1.37	0.00
607	37.8	60.7	1.40	0.00
620	97.0	170.5	1.43	0.00
Off axis				
λ [nm]	RMS radius [μm]	GEO radius [μm]	Airy radius [μm]	Location [mm]
595	124.4	198.1	1.37	-1.42
607	56.1	107.0	1.40	-1.28
620	97.4	168.8	1.43	-1.38

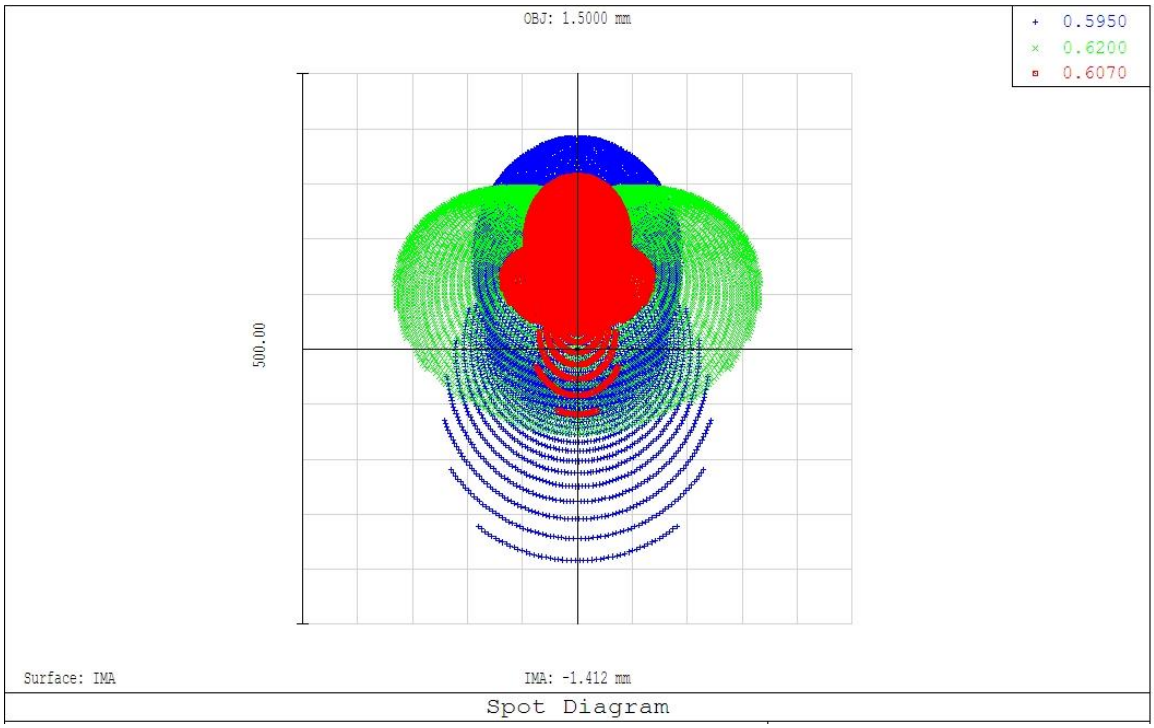

Figure 2.12: Geometric spot diagram of the off axis sources. The square is 500 μm × 500 μm.

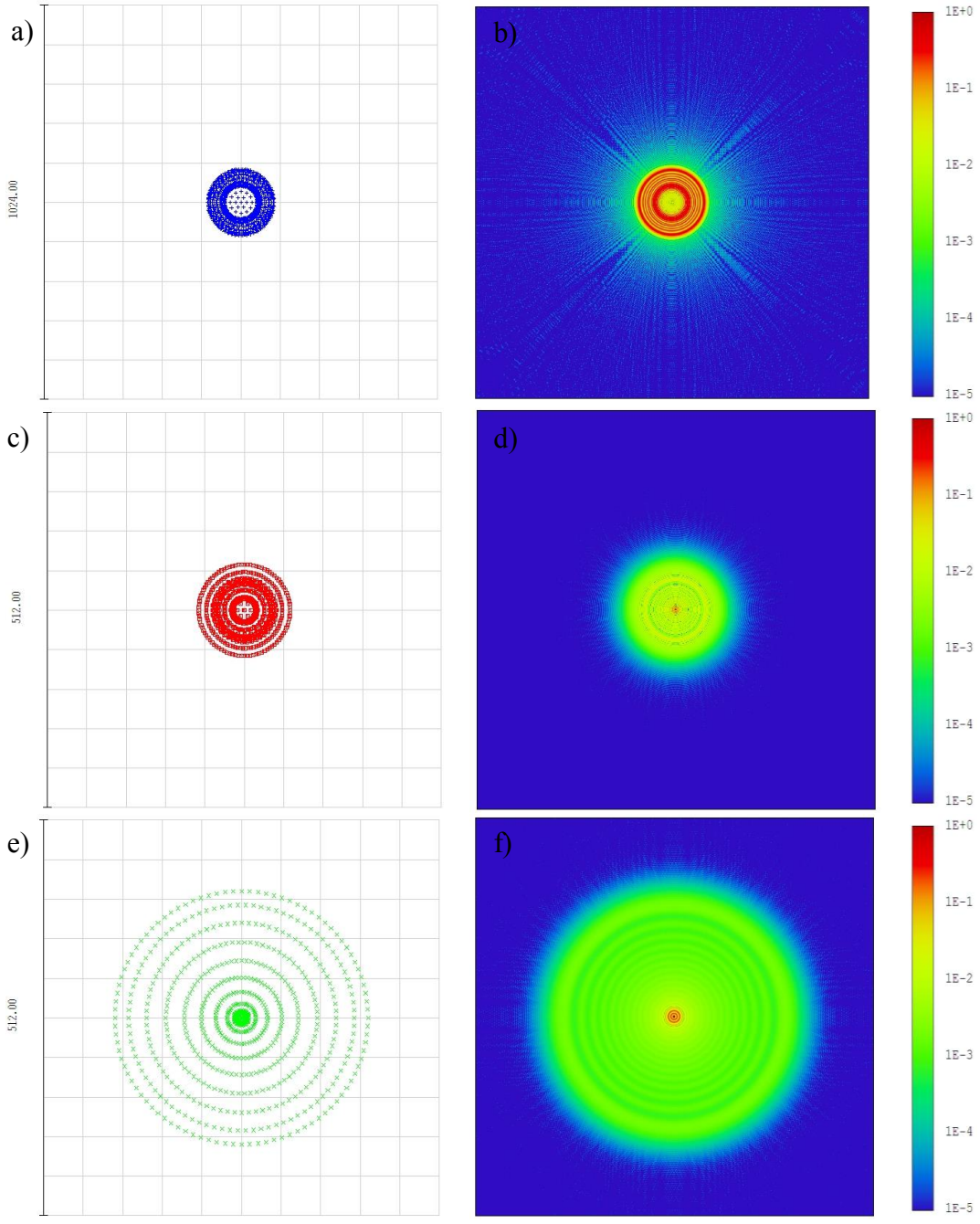

Figure 2.13: Geometric spot diagrams and PSFs of the on-axis sources for (a), (b) 595 nm, (c), (d) 607 nm and (e), (f) 620 nm. The square is 1024 µm × 1024 µm in (a), (b) and 512 µm × 512 µm in (c), (d), (e) and (f).

2.3 TWO POINT MODE

According to the simulations in ZEMAX, it is possible to align the multiple-pass cell in other useful ways. For example, when the circular pattern on the mirrors is collapsed the probe region is shaped like a line, which is oriented parallel to the spot pattern on the mirrors. As shown in Fig. 2.14, the simulations also predict how the cell can be aligned when the sample is inside a transparent chamber. The glass walls are 3 mm thick. The separation between the front and rear mirrors should be slightly increased (few mm) for alignment in the presence of the glass windows.

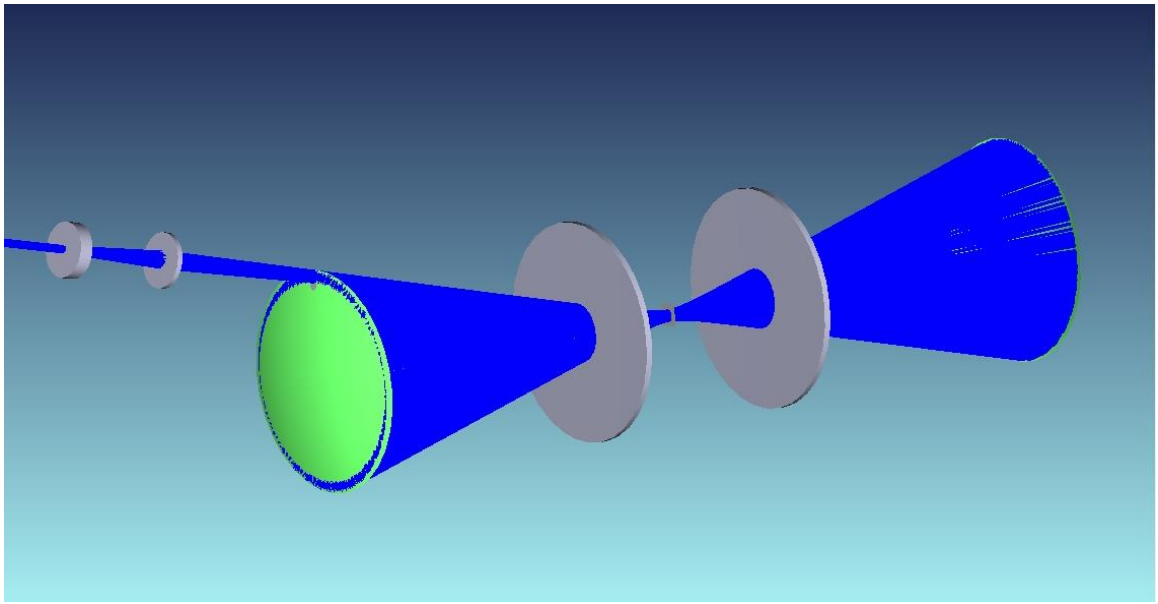

Figure 2.14: Alignment of multiple-pass cell when the sample is contained inside a glass chamber

When the spots line up along the diameter of the mirrors and do not loop back into the mirror the light is focused at two points at the center of the cell as shown in Fig. 2.15.

Even in a simulation it is difficult to align the cell to obtain maximum number of passes. This is because the alignment is extremely sensitive to minor changes in the tilt

and position of the mirrors. So, the mirrors should be mounted on translation stages with very fine spatial resolution. Among the possible useful alignment modes, temperature measurement of flames was carried out in the two point mode as it has the best spatial resolution and scattering can be recorded simultaneously from two regions.

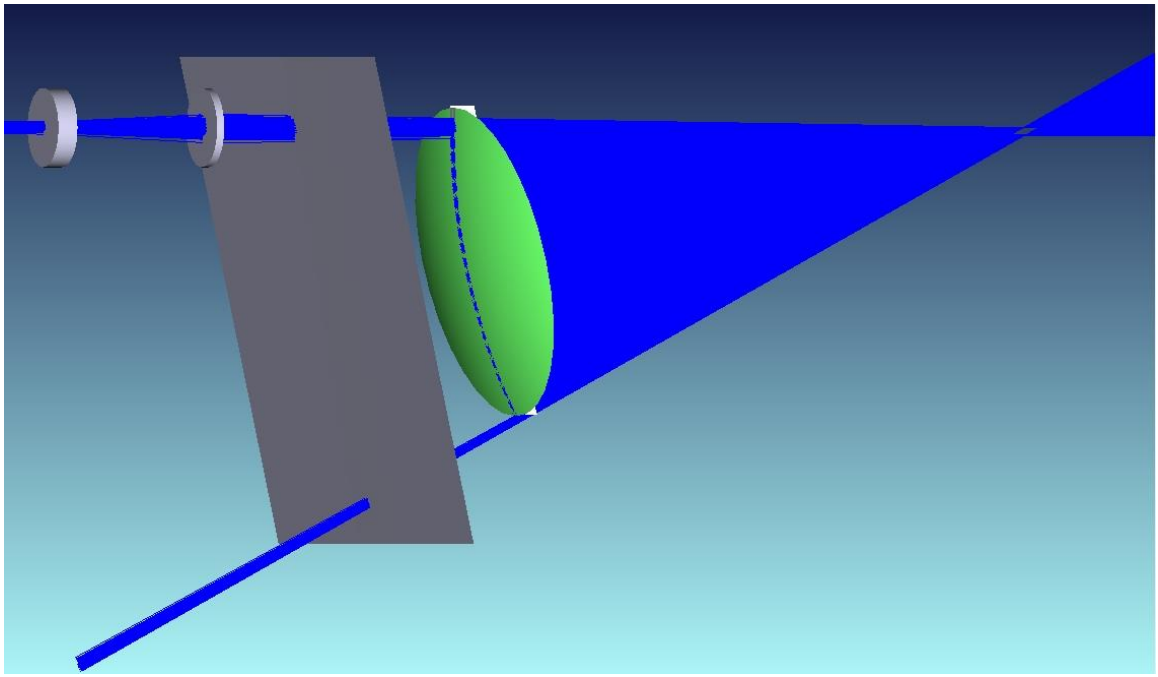

Figure 2.15: Simulation of the two point alignment mode. Telescope, front mirror and the probe region are shown. The rectangles on the two sides of the front mirror are false optical components in place for analysis.

The schematic of the set-up in the two point mode is shown in Fig. 2.16. The pattern on the mirror and the probe region are also shown in Figs. 2.17 and 2.18, respectively. In principle it is possible to obtain better mode matching on the mirrors than in Fig. 2.17 and obtain tight foci at the sample region simultaneously; however, the alignment becomes progressively more difficult and unstable as the number of passes increases.

In this mode the spectra were recorded at high dispersion which gives better spectral resolution. The grating used in the spectrometer is HDG-607 made by Kaiser Optical Systems, Inc. It gives an average linear dispersion of 0.035 nm/pixel in our system, where the pixels are 26 μm × 26 μm. The spectral coverage is 595-620 nm.

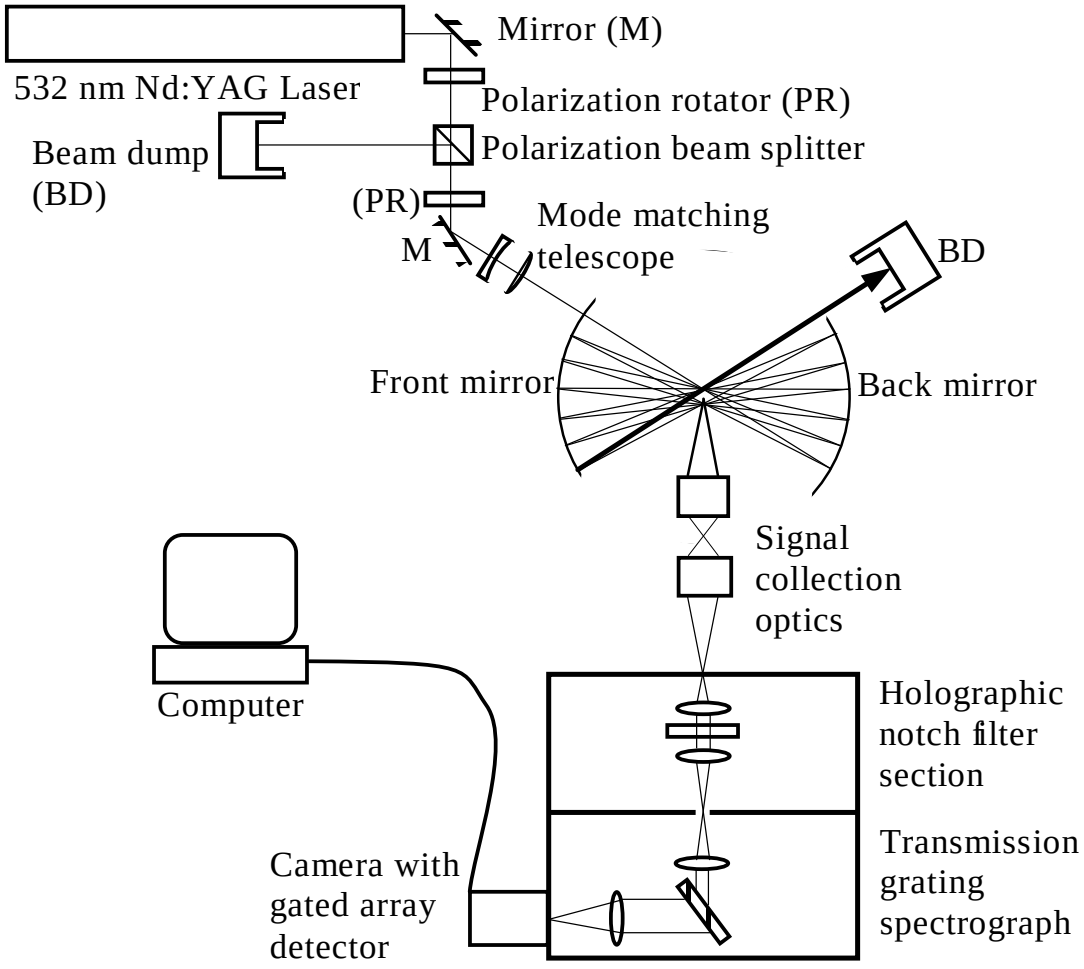

Figure 2.16: The experimental set-up in the two point mode

The separation between the two points is measured in the following way. First, the combined magnification of the collection, the dispersion and the detection optics was determined by imaging an object of known size. A rectangular tape of dimension 2 cm ×

0.5 cm was pasted on a transparency, which was illuminated using a Neon lamp. The tape casts a shadow in the Neon emission spectrum. The spectrum was horizontally binned over the region of active pixels. The dispersion axis is oriented horizontally. The size of the shadow was inferred from a plot of horizontally binned counts vs. the vertical pixel number. The image extent in the vertical direction or *y*-axis depends on the length of the sample. The pixel size is 26 µm × 26 µm, so it is possible to measure the size of the shadow cast by the rectangular tape and hence the magnification. We find that the magnification is 0.48±0.02.

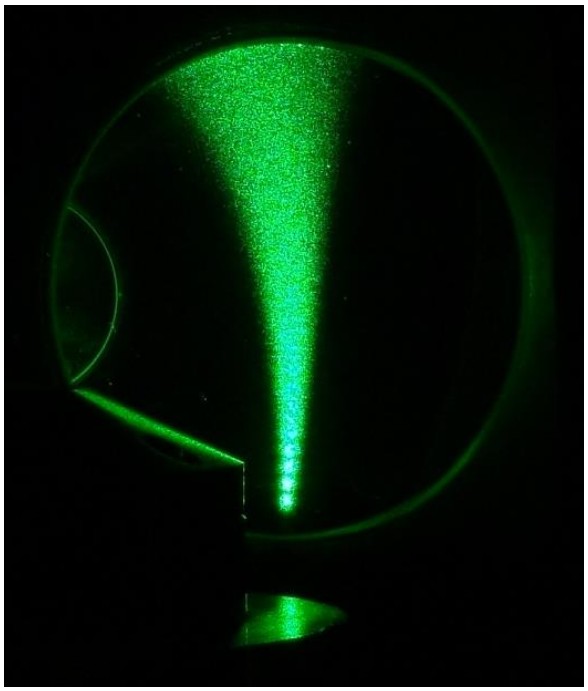

Figure 2.17: Spot pattern on the rear mirror in the two point mode

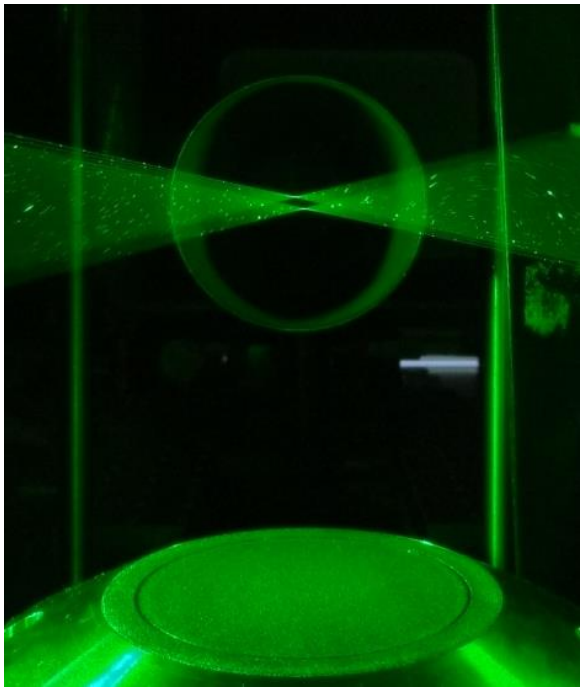

Figure 2.18: Probe region above the burner in the two-point mode

Secondly, Raman scattering is recorded from a near stoichiometric flame. The raw data are shown in Fig. 2.19. The data in Fig. 2.19 were also horizontally binned over the region of illumination and then a plot of horizontally binned counts vs. *y*-pixel # was

generated as shown in Fig. 2.20. From the plot it was inferred that the centers of the two images are separated by 36 pixels and so the two points are separated by 1.95 mm. This measurement was visually confirmed by placing a scale beside the probe region, according to which the separation was ~2 mm.

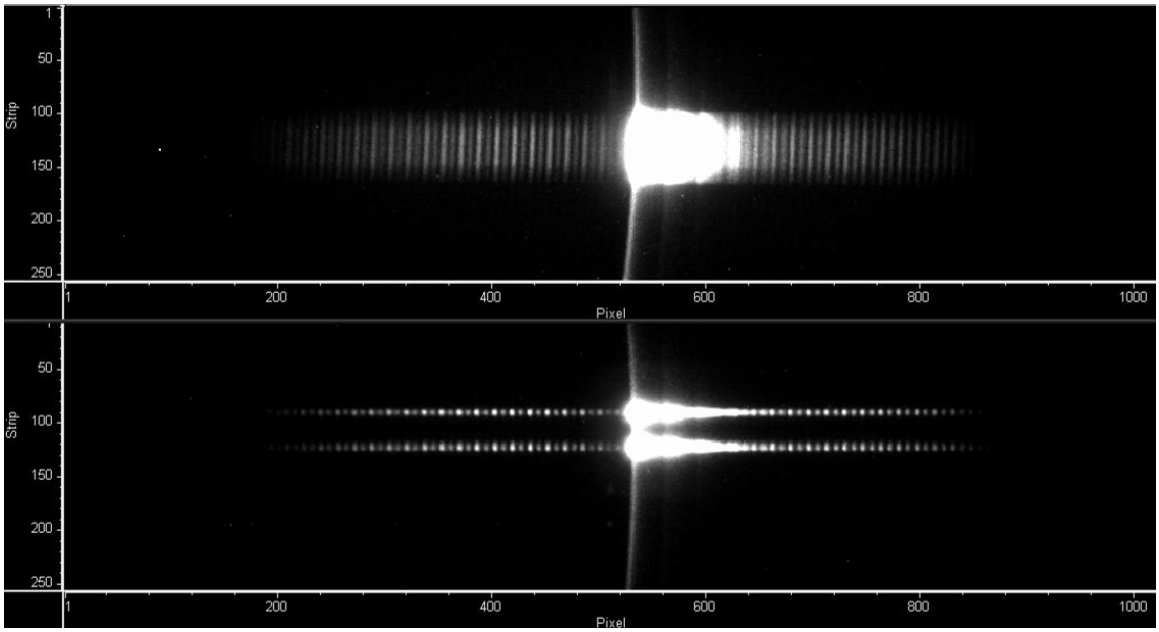

Figure 2.19: Raman signal from flame on the image sensor. Ring mode (top); two point mode (bottom).

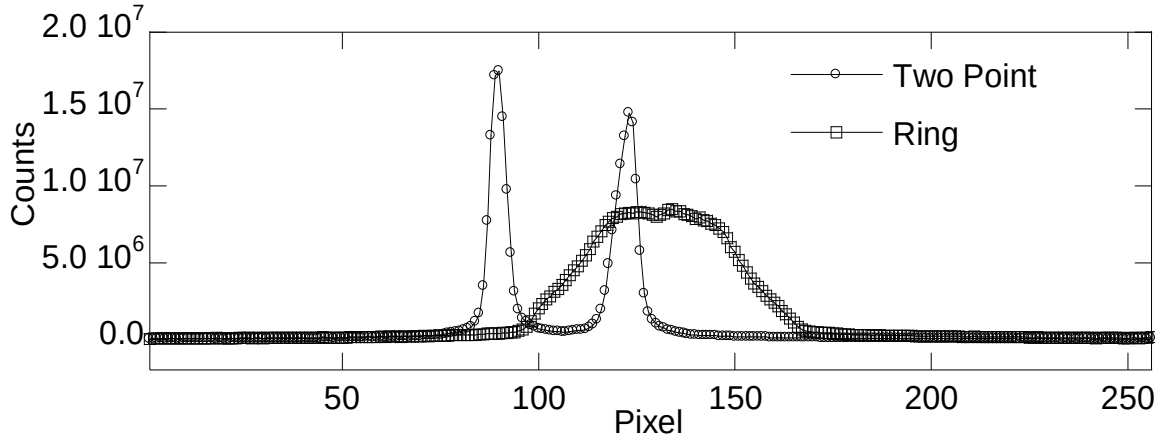

Figure 2.20: Horizontally binned versions of the raw data in Fig. 2.19

The size of the probe region is also deduced from Fig. 2.20. The signal from the lower point extends over 16 pixels and that from the upper point extends over 13 pixels. The FWHM of the lower point is 5 pixels and that of the upper point is 5.5 pixels. Therefore, the total sizes of the upper and lower points are 0.70 mm and 0.87 mm respectively and FWHMs are 0.30 mm and 0.27 mm respectively. Since the slit width is set at 0.1 mm the probe size along the beam propagation direction is 0.2 mm. Hence, the spatial resolution in the new alignment mode is well within the typical probe volume size in an SRS experiment, which is 0.2-1 mm diameter and 0.5-2 mm length (along the beam propagation direction) [37].

In addition to the obvious improvement in the spatial resolution, operation in the two point mode achieved 1.55±0.15 times more power deposition in comparison to the ring mode within the central 300 μm of the probe region. This can be deduced from Figs. 2.19 and 2.20 in which the intensity profiles of the signal obtained in the ring and the two point modes are shown. The data in both modes were taken with the high dispersion grating in the spectrometer.

It was not possible to directly count the number of spots in the two point mode because of the washout of the spot pattern on the mirrors as a result of poor mode matching which is also evident in Fig. 2.17, and so the number of passes is deduced by comparison of the area under the profiles to the area with the ring mode. The ring mode was operated with 100 passes. Comparison between the total counts in the ring mode and the two point mode indicate that the two point mode was operated with 26 passes at each point.

The spatial stability of the probe regions is determined by studying 79 frames of Rayleigh signal acquired at 0.5 s intervals from a near-stoichiometric flame. The notch filter is removed to acquire Rayleigh signal, and the HDG-607 grating is replaced with

HFG-539.5 as the spectral coverage of the former does not include the wavelength of Rayleigh scattering. Each frame is acquired from single pulse i.e. multiple passes of single laser shot. It is not possible to detect Raman signal from flame using single pulse with our apparatus so Rayleigh signal was used to study the stability. It was found that the peak of the upper point can be anywhere within 5 pixels and the peak of the lower point can be anywhere within 4 pixels, which translates to uncertainty in the probe region location of 245±25 μm.

It is necessary to measure the effective collection f/# accurately as the angular dependence is included in the high resolution spectral model. For this purpose, an iris with adjustable aperture size is placed in front of the objective lens of the first camera lens. Rayleigh signal is recorded as the aperture size is varied. The intensity of the signal binned over the pixels illuminated by scattering from the lower point increased as the pupil was widened up to 19.5 mm in diameter. It indicates that the spatial extent of the cross section of the signal at the location of the iris was 19.5 mm. The iris was at 115 mm from the probe region so the effective collection f/# is 5.9.

As mentioned earlier, the camera has a gated intensifier which is switched on only when the signal is incident on it. In the new alignment, the total number of passes is different and the separation between some of the optics has also changed slightly so the optimum gate width and delay were determined again. As expected the gate delay remained the same at 5 ns. In the ring mode the gate width was 165 ns and the gate width in the two point mode is 90 ns. The gate delay is determined as follows. Rayleigh signal is recorded with a fixed gate width of 200 ns for varying gate delay. Plot of gate delay vs. signal is generated. From the plot it can be easily inferred that the signal increases when the delay is decreased down to 5 ns and then it stays constant on shorter delays. Gate width is determined from a plot of gate width vs. total Rayleigh signal when the delay is

fixed at 5 ns. The signal continues to increase to up to gate width of 90 ns and then it becomes constant. It indicates that the single pulse remains inside the multiple-pass cell for 90 ns before it eventually exits the cell.

The grating was tested using a cavity black body and a polarizer, and it was found to be slightly polarization sensitive. Black body spectra were recorded as a function of polarizer orientation which was changed in steps of 10°. The recorded signal was binned along the dispersion and non-dispersion axes for each orientation of the polarizer. The plot of total counts vs. polarizer orientation showed that the total count varies by 8% about an average value. Raman signals can be decomposed into polarized and unpolarized components. Since the grating is polarization sensitive, in order to compare data with simulations either the polarization sensitivity has to be characterized and included in the model or the signal should be completely depolarized before it is incident on the grating. We first attempted to depolarize the signal by using an achromatic depolarizer DPU-25 available from Thorlabs. However, tests on the depolarizer using an expanded beam from a He-Ne laser showed that the depolarizer is not capable of completely removing the polarization of the monochromatic light incident on it. Of the total He-Ne radiation that passes through the depolarizer about 89% is unpolarized and 11% still remains polarized and only about half the incident intensity is transmitted by the depolarizer. Hence, it was decided to dispense with the depolarizer and account for the polarization sensitivity of the grating in the model. The discussion on the determination of the polarization sensitivity is in chapter 3.

Chapter 3: Calibration

It is essential to test and calibrate an instrument irrespective of whether it is recently purchased or imported from an old experimental set up. Even when the readings are in the desired units, it is a good practice to test it by comparing against a standard source. This is because calibrations are valid for a particular setting, which may not be the case in the experimental set-up in the lab. Calibration is also necessary to express the raw data in standard units by correcting for non-uniform sensitivity of the measurement device. In this chapter, the flow meter calibration, wavelength and intensity calibrations are presented. The characterization of the depolarizer is also presented.

3.1 WAVELENGTH CALIBRATION

The raw data is acquired in terms of pixels along the dispersion axis. The purpose of wavelength calibration is to convert pixels to wavelength units. First the calibration for the experiment with high dispersion grating is described. A neon lamp is used as the source for wavelength calibration as it has many emission lines in the spectral region of the Stokes signal from N_2. Other calibration lamps at our disposal did not have intense and uniformly distributed emission lines in this region. Thirteen neon emission lines between 596.1623 nm and 618.2146 nm are recorded. These lines are tabulated in the NIST database [38] and also by Kim *et al.* [39]. The line centers of the recorded transitions are determined to sub-pixel resolution by curve fitting the data. The curve fit to seven neon lines within the spectral range of interest is shown in Fig. 3.1. The curve fit to the six other lines with lower intensity is carried out separately. Fitting the lower intensity peaks separately helps to increase the accuracy of the curve fit as the curve fit tries to minimize the square of the difference between the data and the fit, and so the high intensity peaks inherently receive greater weighting. In the curve fit procedure, the line

shape parameters, the line center, the overall scale and the linear background are set as the floating parameters. A convolution of a trapezoid with a Lorentzian is used to model the recorded line shape function. Details on the choice of a suitable line shape are in chapter 4. The calculated line center is not sensitive to the choice of the line shape model. The differences between the values of the line centers obtained with various line shape models is less than 0.01 pixel. The line positions in terms of pixels are then compared with line positions in terms of wavelength to generate a direct mapping between pixels and wavelength.

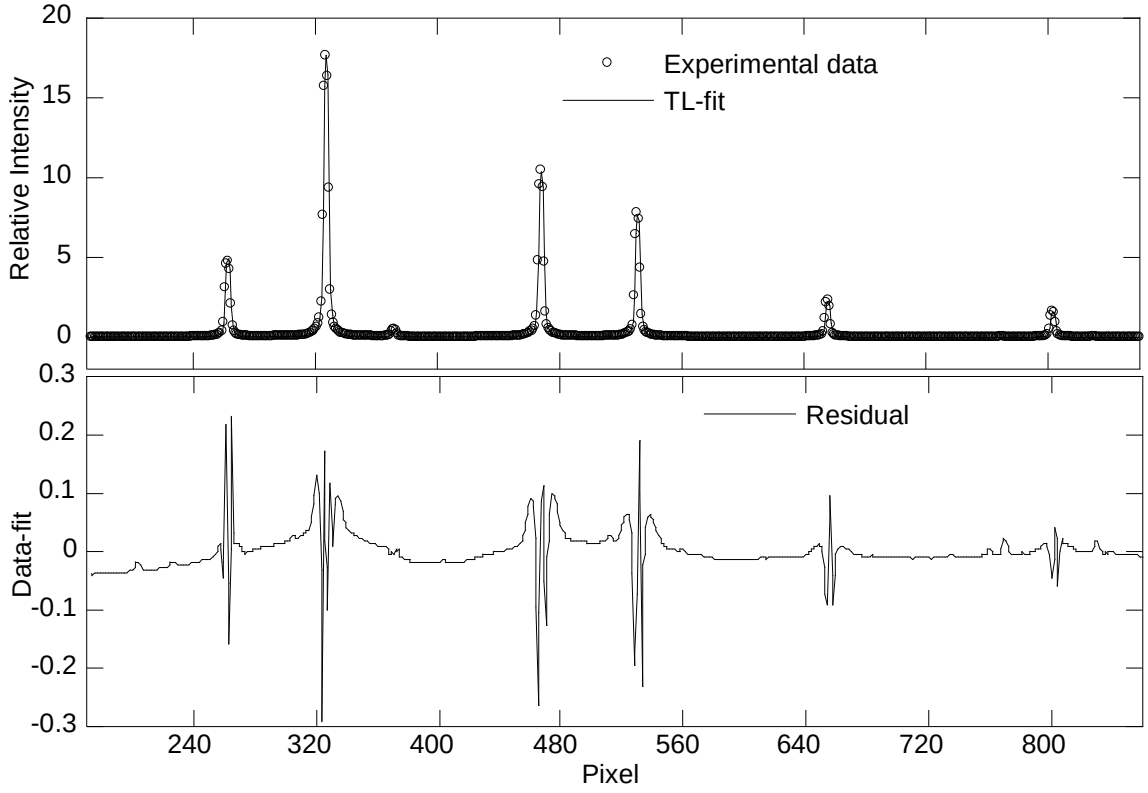

Figure 3.1: Curve fit to atomic line emissions from neon lamp to determine the pixel positions of the line centers

The plot of pixel position vs. wavelength is shown in Fig. 3.2. The plot is curve fitted with quadratic and cubic functions. Both the functions are apparently indistinguishable; however, they deviate more from one another at the edges of the spectral range of interest.

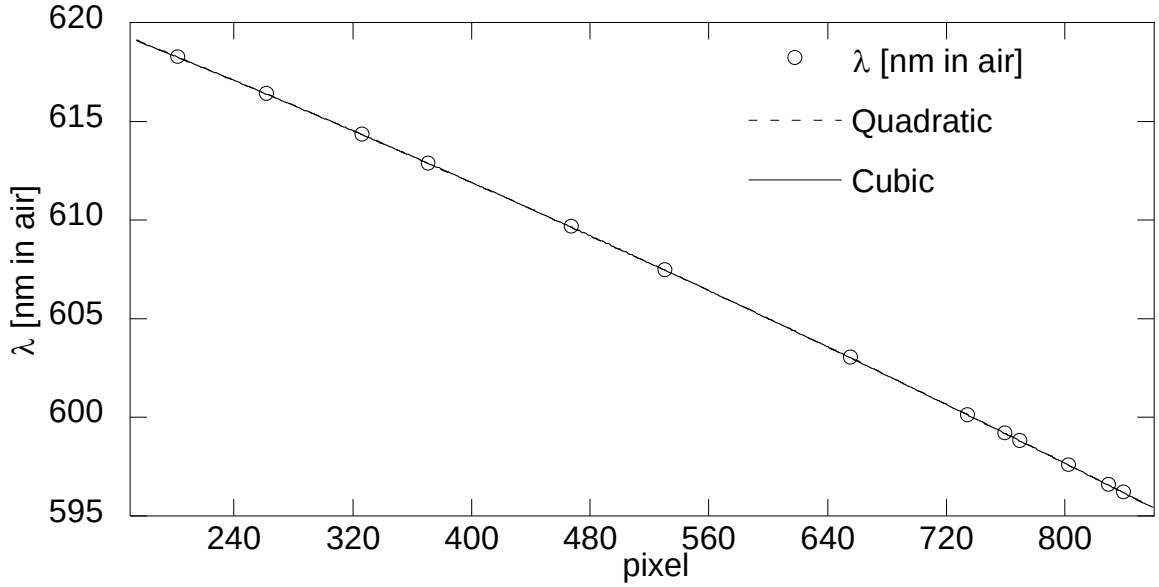

Figure 3.2: Determination of the wavelength calibration function with high dispersion grating. $\lambda = c_0 + c_1 p + c_2 p^2 + c_3 p^3$; c_0 = 624.13, c_1 = -0.027524, c_2=-8.1958×10^{-6}, c_3 = 1.5781×10^{-9}.

As shown in Fig. 3.3, the plot of residuals vs. pixel number shows that there is systematic error when the wavelength calibration function is quadratic. Hence, the cubic function is used for wavelength calibration. Figure 3.3 also shows that a higher order model does not improve the agreement between the data and the curve fit. When the quadratic calibration function was used to obtain the wavelength axis there was noticeable disagreement between the positions of the peaks of rotational-vibrational transitions in the calibrated data and its simulation at high and low wavelengths. However, when the cubic wavelength calibration function is used there is good

agreement between the line positions at all wavelengths. The calibration function converts pixels to wavelength in air. The modeling is done in vacuum wavelengths so the wavelength calibration function is multiplied by the refractive index of air at this wavelength, 1.00027 provided by NIST [40][11]. The dispersion of the high dispersion grating is ~0.03 nm per pixel, but it varies across the spectrum because the mapping between pixel number and wavelength is non-linear.

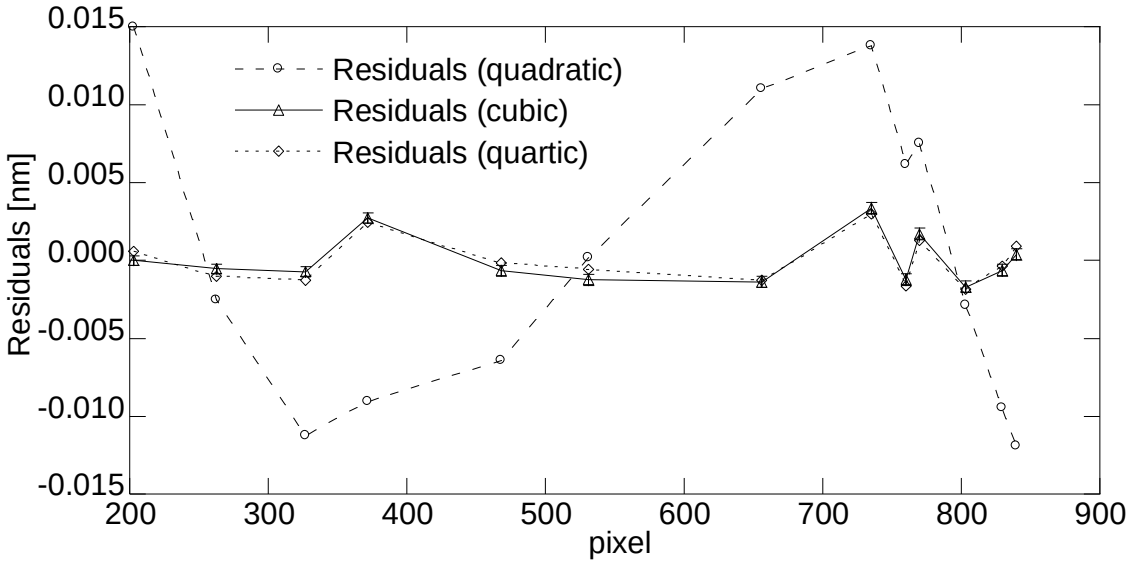

Figure 3.3: Residuals in the curve fit on pixel vs. wavelength. Uncertainty error bars on the cubic points reflect 0.01 pixel uncertainty in line center location and corresponding uncertainty in wavelength based on local slope.

When low dispersion grating was used the wavelength calibration was performed by recording spectra from xenon and krypton calibration lamps (Oriel 6033 and 6031).

[11] The refractive index of air can be calculated by using the so-called Cidor equation or the Elden equation. The value of n-1 is sensitive to the composition of air. In the Elden equation the humidity of air is also an input parameter whereas in Cidor equation CO_2 concentration is also an input parameter in addition to humidity. Assuming that CO_2 in air is 390 ppm, when $10 \leq$ % humidity ≤ 80 we get $2.7019 \times 10^{-4} \geq n\text{-}1 \geq 2.69523 \times 10^{-4}$ at room temperature and pressure according to Cidor equation, and $2.70199 \times 10^{-4} \geq n\text{-}1 \geq 2.69533 \times 10^{-4}$ according to Elden equation. For our purpose n=1.00027 is sufficient for the agreement between the recorded and the predicted line positions of the Raman transitions.

The calibration function is shown in Fig. 3.4. The xenon lamp has emission lines in the anti-Stokes region and the krypton lamp has emission lines in the Stokes region.

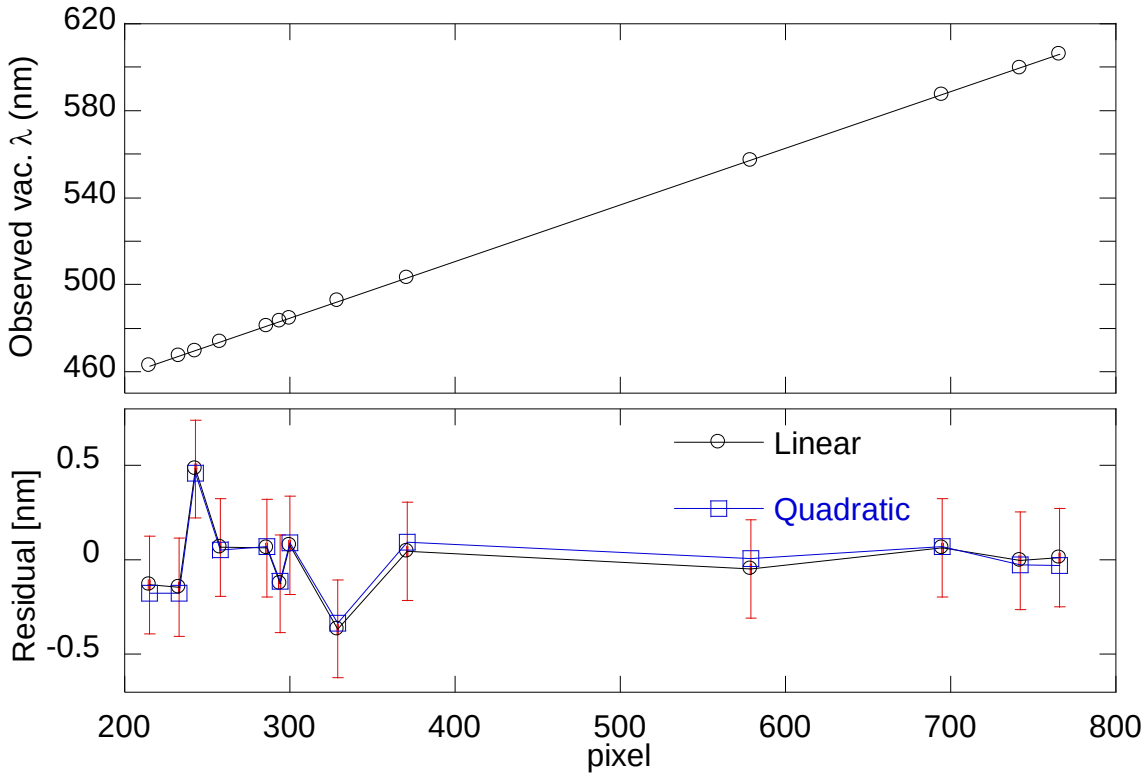

Figure 3.4: Determination of wavelength calibration function with low dispersion grating. $\lambda = c_0 + c_1 p; c_0 = 406.48, c_1 = 0.26019.$

For these low dispersion measurements the pixel positions of the atomic emission lines were not determined by curve fitting. They were read directly from the raw data. The line shape was determined later from the calibrated data. The line positions tabulated in NIST were used to convert observed line positions in pixels and thus determine the wavelength calibration. The uncertainty in pixel position is ±0.5 pixel and the uncertainty in wavelength is ±0.26 nm. Such assignment of uncertainty assumes that if a pixel is imagined as a square then the center of the square corresponds to exactly the reference pixel # so that any photon that lands at ±0.5 pixel from the center is assigned that pixel

number. The uncertainty in wavelength is ±0.26 nm because the dispersion of the low resolution detection system is 0.26 nm per pixel.

As shown in Fig. 3.4, the dispersion of the low resolution system is found to remain constant, which is consistent with the spectrograph's specification. The residuals of the wavelength calibration functions are almost equal between the linear and the quadratic fit, which confirms that the wavelength calibration function is linear.

3.2 INTENSITY CALIBRATION

In the raw data the signal is recorded in terms of counts. Intensity calibration accounts for the relative sensitivity of the various pixels and converts the counts to relative intensity. The intensity calibration is carried out using SR-20 cavity black body manufactured by CI Systems. This black body is considered a reliable standard radiation source in the 400 to 1450 nm wavelength region. The black body was set at 1473 K, which is its maximum set temperature. In order to obtain an accurate calibration, the system response was measured with all optical components in place including the holographic notch filter used to suppress elastic scattering of the excitation at 532 nm. The notch filter is specified to attenuate laser scatter by six orders of magnitude. The details of the filter transmission are not critical to temperature measurements that are made using the N_2 Stokes and anti-Stokes scattering at wavelengths (607 and 473 nm) far from the filter stop band. The expected black body spectrum is calculated using Planck's function. Since the instrument function has very narrow width compared to the width of the black body spectrum, the convolution of the instrument function with Planck's function is indistinguishable from it. The calibrated intensity is obtained using the following relation.

$$\frac{Planck's\ function}{Blackbody\ counts} \times Raman\ counts = Calibrated\ Raman\ intensity \qquad (3.1)$$

The calibration factor for the high dispersion grating is used point by point i.e. a curve fit is not performed to generate an intensity calibration function. This is because there is an intrinsic absorption like structure in the recorded black body spectrum as shown in Fig. 3.5.

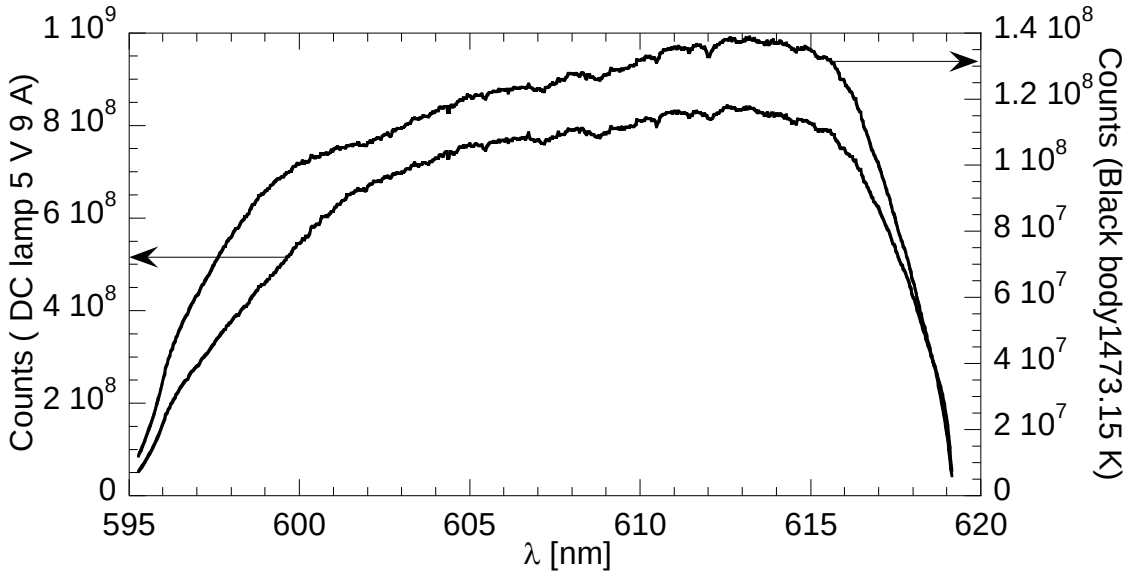

Figure 3.5: Black body and lamp counts as a function of wavelength. The power supply of the lamp was set at 5 V and 9 A. Both the lamp and the black body spectra are recorded under identical camera settings.

This absorption like structure in the recorded black body spectrum cannot be attributed to noise because it is independent of the acquisition time. Furthermore, the recorded features are independent of the source as they were also detected in spectra from a tungsten lamp. They are also not caused by the relative sensitivity of the detector pixels as exactly the same features are not seen in a spectrum taken at low dispersion on the same detector as shown in Fig. 3.6. The absorption like features are noticeable at longer

wavelengths. The spectrum at shorter wavelengths is relatively smooth. We believe that the observed features can be attributed to the absorption characteristics of the dichromated gelatin [41] used in the grating or in the coatings of the optics.

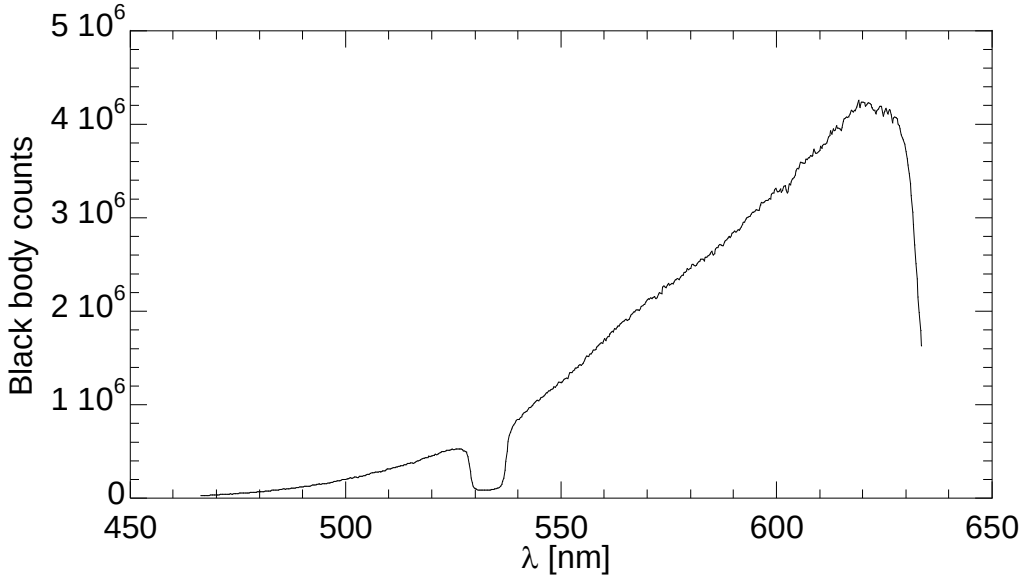

Figure 3.6: Raw black body spectrum obtained using a low dispersion grating

The low and high resolution intensity calibration functions are shown in Figs. 3.7 and 3.8, respectively. The low resolution experiments were carried out 2 years before the high resolution experiments. At that time, it was not obvious that the lack of smoothness in parts of raw black body spectrum has a physical origin. So, in the case of low resolution spectrum the calibration function was obtained by curve fitting.

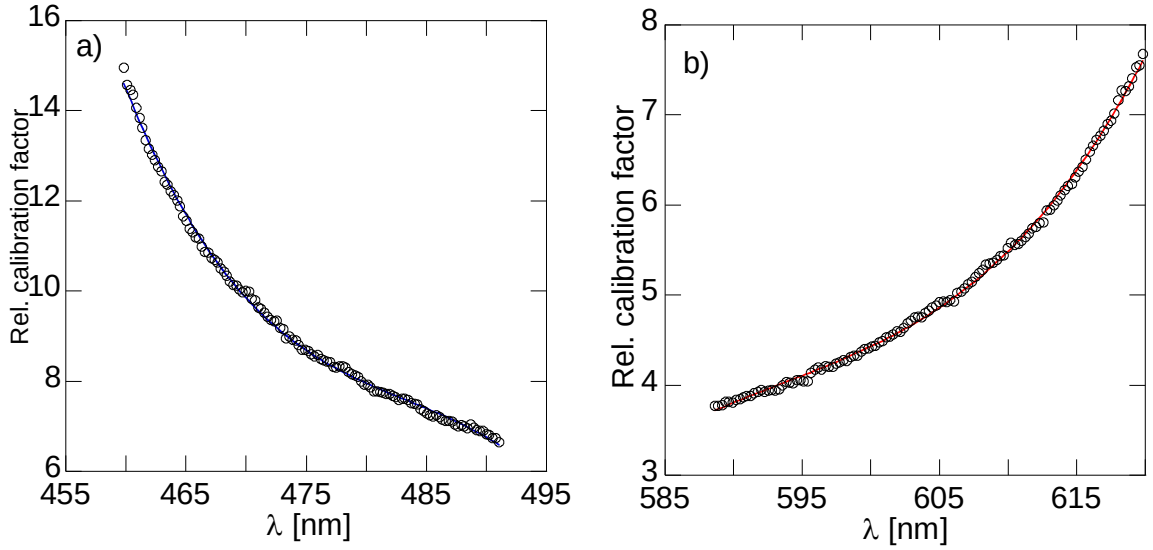

Figure 3.7: Intensity calibration function, $y = c_0 + c_1\lambda + c_2\lambda^2 + c_3\lambda^3$, in (a) anti-Stokes region; $c_0 = 38786, c_1 = -240.45, c_2 = 0.49722, c_3 = -3.4288 \times 10^{-4}$, (b) Stokes region; $c_0 = -23599, c_1 = 119.17, c_2 = -0.20067, c_3 = 1.1268 \times 10^{-4}$.

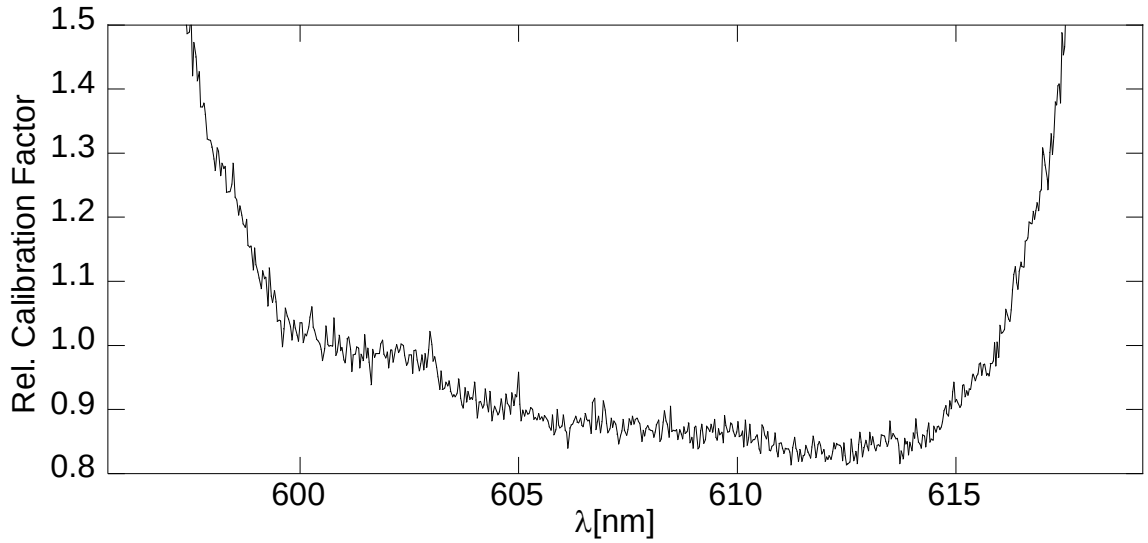

Figure 3.8: Intensity calibration factors with high dispersion grating

3.3 CHARACTERIZATION OF THE DEPOLARIZER

The collection optics is polarization sensitive. Figure 3.9 shows the polarization sensitivity compensation curve. It is generated in the following way. The high dispersion grating is used in these experiments. The notch filter is removed and a polarizer is mounted in its place. The black body is used as the source. The radiation from the blackbody is unpolarized. So, if the detection system is not polarization sensitive then a uniform response is expected as a function of the orientation of the polarizer. However, when the polarizer was rotated in steps of 10 degrees a non-uniform response was observed. The reciprocal of the black body counts as a function of polarizer orientation was normalized to generate Fig. 3.9 so that when the recorded black body spectrum as a function of polarization angle is multiplied by the function in Fig. 3.9 we obtain a flat line. If the polarization of the incident signal is known then its product with the factor corresponding to that polarization given in Fig. 3.9 will make up for the varying response arising from polarization dependence of the collection optics.

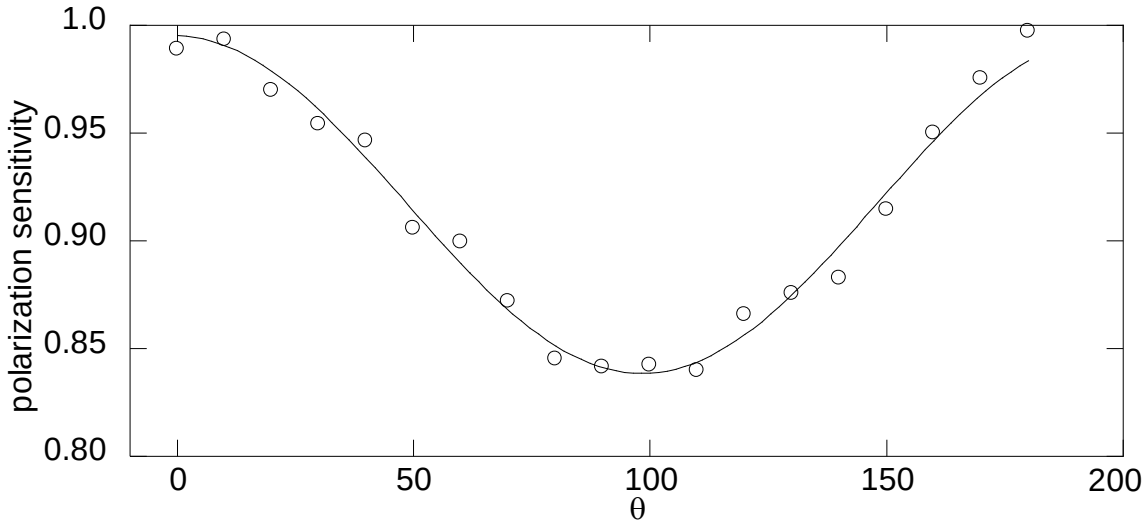

Figure 3.9: Polarization sensitivity compensation curve. $y = A_0 \cos(n\theta + \phi) + k$; $A_0 = 7.8371 \times 10^{-1}, n = 1.8178, \phi = 1.3571, k = 0.91691.$

The Raman spectrum consists of the strongly polarized Q branch and the strongly depolarized S and O branches. Figure 3.10 shows the variation in the intensity of the Q branch signal from N_2 in air as a function of the orientation of a linear polarizer. The signal is generated by binning over 6 x × 10 y-pixels. As expected, it shows that the Q branch is strongly polarized. Because of ~15% variation in system response to polarization we considered using a depolarizer (ThorLabs DPU-25) in the collection optics. However, this depolarizer is not used in the final set-up. Its test and characterization is described here to explain why it was not used.

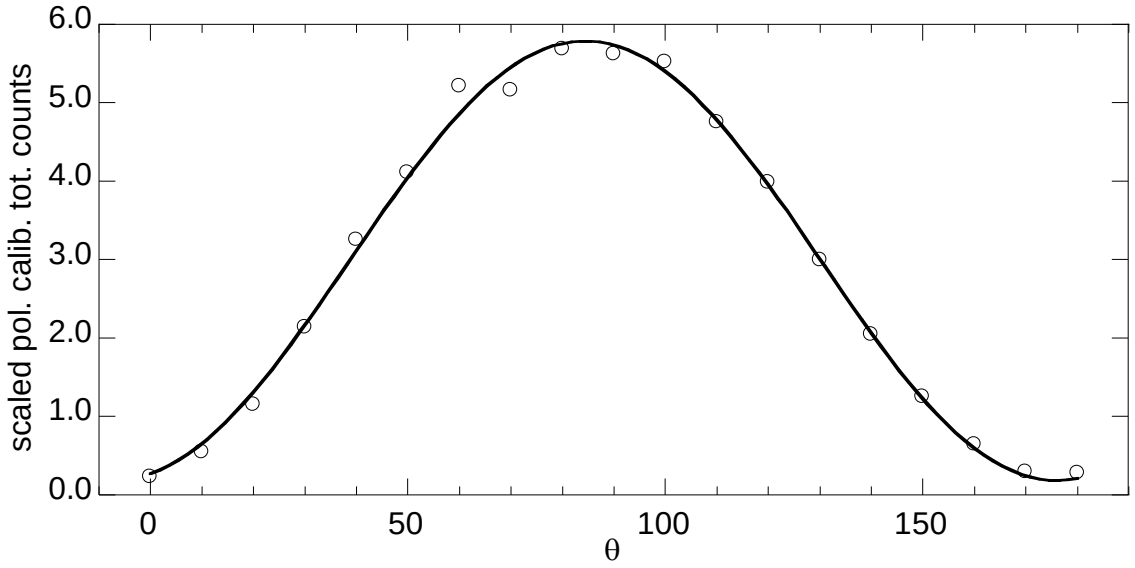

Figure 3.10: The intensity of Q branch as a function of the orientation of the polarizer on its path. The curve fit function is $y = A_0 \cos^2(n\theta + \phi) + k$; $A_0 = 5.6028, n = 0.98347, \phi = -83.047, k = 0.18568$.

The performance of the depolarizer was characterized by shining it with a He-Ne laser, which is also polarized. A polarization rotator was used to orient the polarization of the He-Ne laser in the same direction as the Q branch. The experiment was set up on a table separate from Raman experiments; the depolarizer was also oriented in the same

way as in the Raman experiment. A linear polarizer was mounted behind the depolarizer to select the polarization of light falling on the power meter. Figure 3.11 shows the variation in the measurement by power meter as a function of the relative polarization angle. It shows that even after polarized light passes through the DPU-25 depolarizer 11% of the total intensity remains polarized.

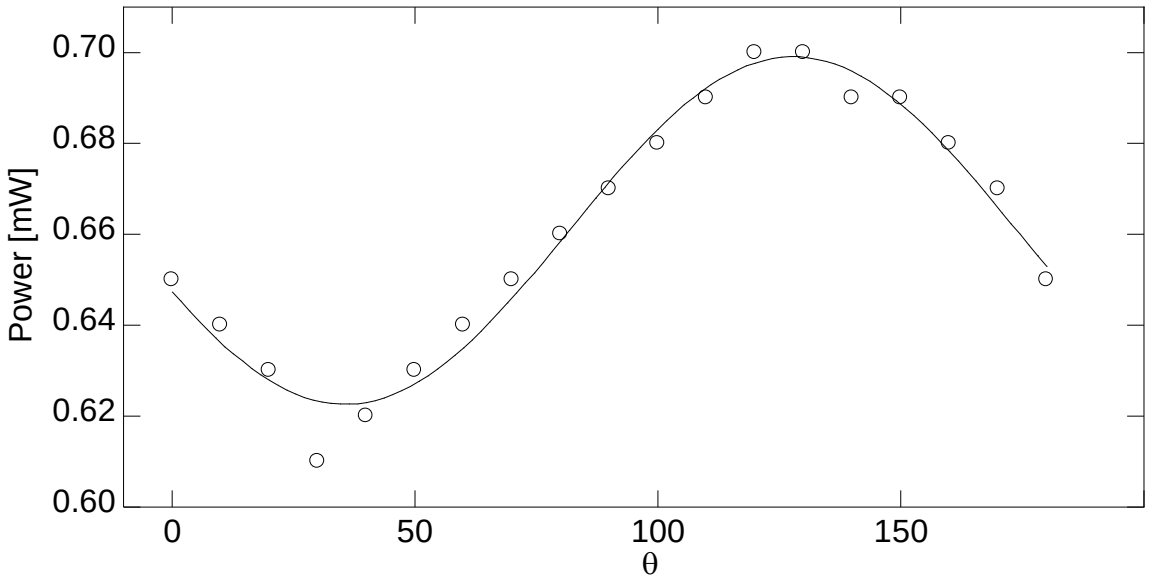

Figure 3.11: Analysis of the output of the depolarizer using a linear polarizer to assess the degree of depolarization achieved. The curve fit function is $y = A_0 \cos^2(n\theta + \phi) + k; A_0 = 7.6495 \times 10^{-2}, n = 0.97607, \phi = 55.235, k = 0.62259.$

We decided to dispense with the depolarizer and include a polarization sensitivity factor in the model because the depolarizer does not scramble the polarization effectively, i.e. it's output still shows substantial residual polarization if the incident light is strongly polarized, and it also transmits only half of the incident light.

When we didn't include a polarization sensitivity factor in our model the Q branch intensity was always under predicted and one way to make the data agree with the model was to multiply the observed intensity by a polarization correction factor which

would suppress it and make it agree with the model. This method is complicated as the signal is not completely polarized and strictly speaking it does not also have a unique polarization as it is generated by multiple beams passing at different angles. So, instead of suppressing the intensity of Q branch in data we enhance it in the model by scaling α' (and higher derivatives of α) up by the polarization sensitivity factor.

The inclusion of the polarization sensitivity factor in the model is explained in chapter 4. Its value is determined by trial and error. In the first step, we curve fit to O and S branches in room air without the Q branch using a detailed spectral model. In this fit we determine the overall scale factor for the spectrum, the background, and the instrument line shape parameters, i.e. the half width of the base of the trapezoid, the half width of the top of the trapezoid and the Lorentz scale; temperature (295 K) is set as a fixed input parameter. In the second step, the parameters obtained from the first step are used to simulate the entire spectrum (O, Q and S branches) and the results compared with the data from room air. In the third step, if the simulated intensity of the Q branch does not agree with the recorded intensity then the value of the polarization sensitivity factor is updated in the detailed spectral model, the first step is revisited and the iteration is repeated until the simulated intensities of the O, Q and S branches agree with the recorded intensities. We find that the value of polarization factor is 1.17 when the polarizability derivatives for $^{14}N_2$ given by Buldakov *et al.* [42] are used. As we discuss below the polarization sensitivity factor not only accounts for the polarization sensitivity of the detection optics, but it also compensates for possible error in the relative values of the isotropic and anisotropic polarizability derivatives.

Since the relative intensity between Q and O or S branches are proportional to the ratio of the square of α' to γ', when the polarization sensitivity factor is 1.17 the predicted intensity of the Q branch is increased by a factor of 1.36. However, according to Fig. 3.9,

the recorded intensity of polarized light at ~84 degrees should be scaled down by ~0.85; which implies that if the data is not corrected for the polarization sensitivity then the intensity should be scaled up in the model by a factor of 1.18. This indicates that the ratio of α' to γ' given by Buldakov may not be correct if we assume that the relative intensity of Q branch to O branch depends only on the ratio of α' to γ'. According to Buldakov, $\left(\frac{\alpha'}{\gamma'}\right)^2 = 0.70$. According to Knippers $\left(\frac{\alpha'}{\gamma'}\right)^2 = 0.83$. If we had used Knippers' value of $\frac{\alpha'}{\gamma'}$ then the intensity of Q branch in the model would have to be enhanced by 1.15 times, which is closer to the enhancement factor expected from the characterization of polarization sensitivity using the black body. This indicates that the value of $\frac{\alpha'}{\gamma'}$ given by Knippers is more accurate. However, the intensity of the Q branch relative to the O and the S branch depends on the ratio of α' to γ' only in the harmonic approximation. When the anharmonic effects are included the higher order polarizability derivatives also determine the relative intensities Q and O or S branches.

3.5 FLOW METER CALIBRATION

The calibration of rotameters was indispensable because the recorded spectra were not consistent with the spectra expected from the metered equivalence ratio of the flame. In the low resolution spectra, Raman scattering of oxygen was consistently detected even when methane and air were mixed to produce nominally rich flames. The rotameters were calibrated to resolve this discrepancy between the expected and recorded data. The correct value of volume of air or methane flow at a given time interval was determined by measuring the amount of water the gas flow displaces from an inverted graduated measuring cylinder which is submerged in a tank filled with water. The density of the gases was obtained as follows.

The density of methane and air are tabulated for standard conditions. Their values in the lab can be obtained using the ideal gas law. The following relation is used to calculate density of air and methane in the lab:

$$\rho_{\mathrm{L}} = \rho_S \frac{T_S}{T_L} \frac{P_L}{P_S}$$

The subscript "*L*" denotes 'Lab' and the subscript "*S*" denotes standard. The standard values are constant, the lab values given in the table below were measured in October 2010.

Table 3.1: Temperature, pressure and density of methane and air (October 2010)

	Air	Methane
ρ_S (Grams/Liter)	1.1839	0.6557
T_S (K)	298.15	298.15
T_L (K)	296.21	296.21
P_L (Torr)	755	755
P_S (Torr)	760	760
ρ_{L} (Grams/Liter)	1.184	0.656

In Fig. 3.12, the equivalence ratio calculated using the manufacturer, Cole Parmer's (CP) calibration is compared with the equivalence ratio calculated using our calibration. It is clear that the equivalence ratio is overestimated when the flow conversion tables given by CP is used.

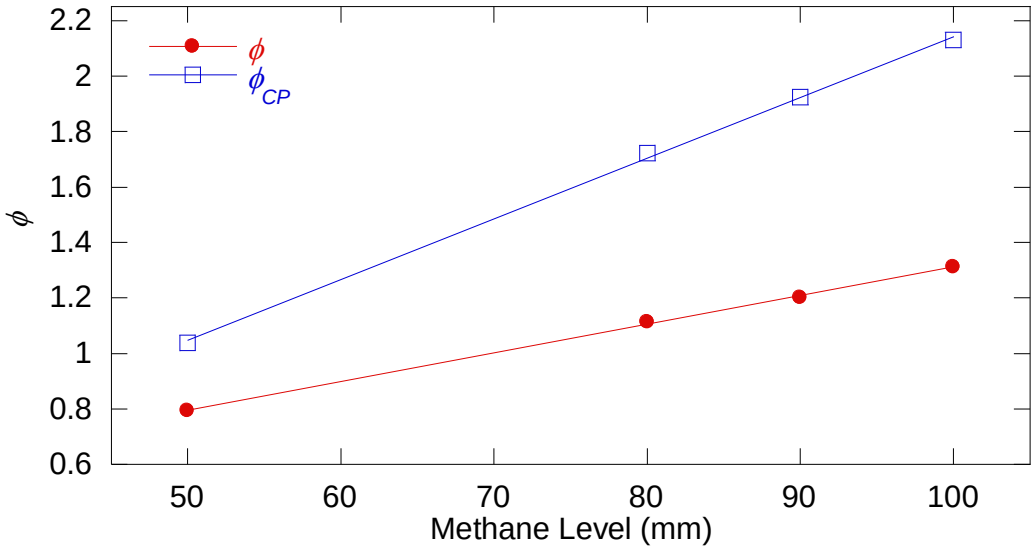

Figure 3.12: Equivalence ratio calculated by using the flow rate table provided by the manufacturer and by using the flow rate determined from calibration in our lab

The calibration was performed again in May 2011 and the following values of density, pressure and temperature were obtained:

Table 3.2: Temperature, pressure and density of methane and air (May 2011)

	Air	Methane
ρ_S (Grams/Liter)	1.1839	0.6557
T_S (K)	298.15	298.15
T_L (K)	295.93	295.93
P_L (Torr)	762.5	762.5
P_S (Torr)	760	760
ρ_L (Grams/Liter)	1.197	0.663

Calibration functions of rotameters for air flow and methane flow are given in Figs. 3.13 and 3.14. In Fig. 3.13, the air flow rate is held fixed at 30 mm level. The methane flow rate is varied.

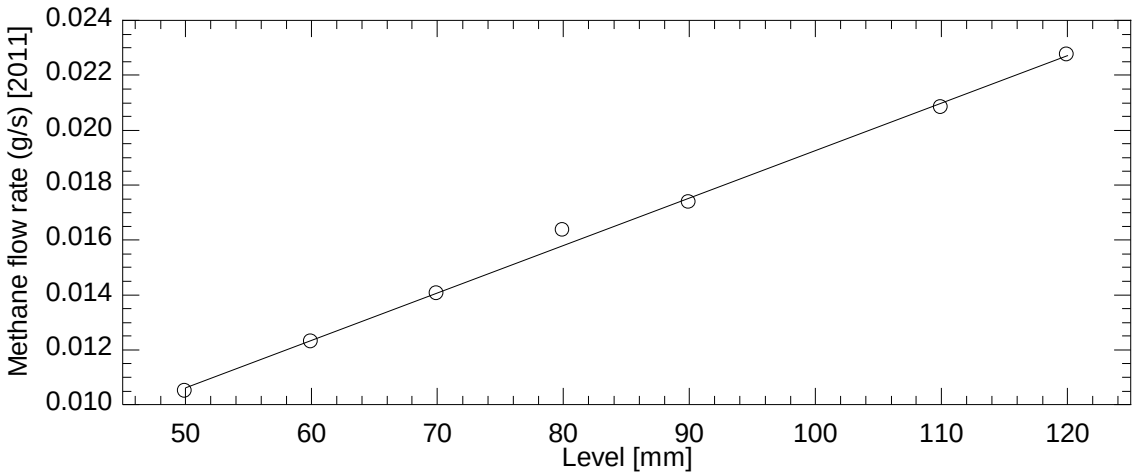

Figure 3.13: Methane flow rate as a function of the position of the floating sphere. The curve fit function is $\dot{m} = c_0 + c_1 l$; $c_0 = 1.9741 \times 10^{-3}$, $c_1 = 1.7288 \times 10^{-4}$.

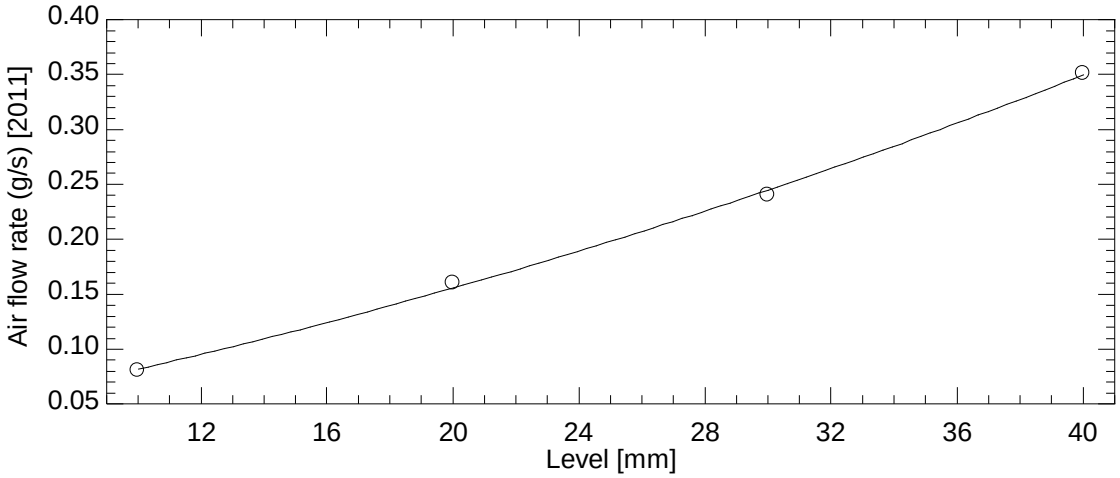

Figure 3.14: Air flow rate as a function of the position of the floating sphere. The curve fit function is $\dot{m} = c_0 + c_1 l + c_2 l^2$; $c_0 = 2.3517 \times 10^{-2}$, $c_1 = 5.0518 \times 10^{-3}$, $c_2 = 7.7452 \times 10^{-5}$.

The results of 2011 are shown in different terms than earlier results because the purpose of showing the earlier results was to underscore the importance of calibrating the instruments for the correct interpretation of the measurements. An instrument only reports numbers, but its measurements are meaningful only after it is calibrated.

The calibration is expected to change with time as the set-ups get modified and the operating conditions change so it is recommended to recalibrate the instruments after some time. The results of 2011 should be thought of as the latest calibration of the flow meters. Figures 3.13 and 3.14 should be used to meter desired amounts of methane and air through the burner.

Chapter 4: Raman Simulation

The experimental data are the combination of Raman signal and background. The temperature measurement requires simulation of the Raman spectrum. The simulation can be fit to the data with temperature as a floating parameter. The total intensity of the signal can also be obtained from the curve fit. In the low resolution spectrum, the ratio of total intensity of the Stokes and the anti-Stokes signals is used to calculate the most reliable value of temperature whereas it is inferred directly from the curve fit on the high resolution Stokes spectrum. In this chapter, the simulation of high resolution spectrum is described first. This is followed by a description of the low resolution spectrum simulation.

4.1 SIMULATION OF THE HIGH RESOLUTION SPECTRUM

The high resolution spectrum obtained in the two point mode was simulated using a detailed theoretical model because the rotational-vibrational lines are well resolved up to high values of rotational quantum number, *J*. Rotational-vibrational transitions up to *J* = 29 can be identified in the data from room air and up to *J* = 42 in flame data. The simulation includes scattering from both $^{14}N_2$ and $^{14}N^{15}N$ as the air that is used as the oxidizer naturally contains trace amounts of the ^{15}N isotope [43]. The ^{15}N isotope is sufficiently rare (0.346 – 0.421% natural abundance) that the contributions of $^{15}N_2$ to the Raman spectrum can be neglected.

The contribution to the total intensity at a given wavelength from a Stokes transition in a molecular species is given by [24]

$$I(\lambda) = \frac{G}{T}[\nu_0 - \nu_k(v,J)]^4 g_s(J) \frac{(2J+1)e^{-\frac{hcE_v(v)}{kT}} e^{-\frac{hcE_J(v,J)}{kT}}}{Q(T)} \times \Phi_x(v,J) S(\lambda; \lambda_k(v,J), b, \Delta\lambda_L, t). \quad (4.1)$$

Slope and baseline offset terms are added to the sum of the intensity of all transitions to match the simulated intensity with the experimental data. Here, G is a constant independent of temperature T and the line position of the transition. It only depends on the mole fraction of the species so that $G_{^{15}N^{14}N} = 6.0\times10^{-3} G_{^{14}N_2}$. The contribution of $^{14}N^{15}N$ is determined by adjusting its value in the code until the intensity of the signal from $^{14}N^{15}N$ in the data from room air matches the simulation. This accounts for both the relative abundance of $^{14}N^{15}N$ and the possible differences in its Raman cross-section from $^{14}N_2$. The factor $\frac{1}{T}$ accounts for the dependence of total number density on temperature at constant pressure. The term $[\nu_0 - \nu_k(v,J)]^4$ arises out of the frequency dependence of the Raman intensity; ν_0 is the excitation frequency and $\nu_k(v,J)$ is the molecular frequency associated with the transition. The term $g_s(J)\frac{(2J+1)e^{-\frac{hcE_v(v)}{kT}}e^{-\frac{hcE_J(v,J)}{kT}}}{Q(T)}$ is the Boltzmann factor that accounts for the relative population distribution among the various vibrational and rotational energy states. Here, $g_s(J)$ is the nuclear spin statistical weight. For $^{14}N_2$, g_s= 3 when J is odd and g_s= 6 when J is even; this causes the intensities in the rotational-vibrational spectrum to have an alternating pattern. For $^{14}N^{15}N$, g_s= 6 for all J. The term $(2J+1)$ is the contribution to the degeneracy of the rotational states from the possible orientations of the angular momentum. $Q(T)$ is the internal partition function, and is computed by a numerical sum over states $Q = \sum_{v=0}^{v_{max}}\sum_{J=0}^{J_{max}} g_s(J)(2J+1)e^{-hcE_v(v)/kT}e^{-hcE_J(v,J)/kT}$, where v_{max} = 10 for $^{14}N_2$ and 7 for $^{14}N^{15}N$, and J_{max} = 100 .

The molecule is modeled as an anharmonic oscillator and non-rigid rotor with coupling between vibrational and rotational energies:

$$E_v(v) = \omega_e\left(v+\frac{1}{2}\right) - \omega_e x_e\left(v+\frac{1}{2}\right)^2 + \omega_e y_e\left(v+\frac{1}{2}\right)^3 + \omega_e z_e\left(v+\frac{1}{2}\right)^4 \qquad (4.2)$$

$$E_J(v,J) = \left[B_e - \alpha_e\left(v+\frac{1}{2}\right) + \gamma_e\left(v+\frac{1}{2}\right)^2\right]J(J+1) - DJ^2(J+1)^2. \quad (4.3)$$

The vibrational and rotational constants of the molecule are given by Laher and Gilmore [44]. The rotational constants of the rare isotope are given by Bendtsen [45]. The vibrational constants of $^{15}N^{14}N$ are obtained by scaling the vibrational constants of $^{14}N_2$ by ρ^n, where ρ is the square root of the ratio of the reduced mass of the dominant isotope to that of the rare isotope, and *n* is the order of the term to which the coefficient belongs [46].

The factor $\Phi_x(v,J)$ in eqn. (4.1) is proportional to the square of the space averaged polarizability tensor component for diatomic molecules. The subscript x identifies the transition between the rotational states. For Stokes scattering, the spectral lines arising from the transition $J \to J+2$ comprise the *S* branch, those from $J \to J-2$ comprise the *O* branch and from $J \to J$ the *Q* branch. This nomenclature is used more extensively later in the discussion.

$$\Phi_{J\to J\pm2} = \frac{7}{45}M(v,\gamma)F(v,J,\gamma)b_{J\pm2,J}4\phi\cos\theta + \tfrac{1}{45}M(v,\gamma)F(v,J,\gamma)b_{J\pm2,J}\tfrac{1}{12}(9\cos\theta - \cos3\theta)\,(\sin2\phi - 2\phi). \quad (4.4)$$

$$\Phi_{J\to J} = \left[M(v,\alpha)F(v,J,\alpha) + \frac{7}{45}M(v,\gamma)F(v,J,\gamma)b_{J,J}\right]4\phi\cos\theta \quad (4.5)$$

$$+\left[M(v,\alpha)F(v,J,\alpha) + \frac{1}{45}M(v,\gamma)F(v,J,\gamma)b_{J,J}\frac{1}{12}(9\cos\theta - \cos3\theta)\,(\sin2\phi - 2\phi)\right].$$

The quantities $b_{J\to J'}$ in eqns. (4.4) and (4.5) are the Plackzek-Teller coefficients given by

$$b_{J\to J-2} = \frac{3J(J-1)}{2(2J+1)(2J-1)},\ b_{J\to J} = \frac{J(J+1)}{(2J-1)(2J+3)},\ b_{J\to J+2} = \frac{3(J+1)(J+2)}{2(2J+1)(2J+3)}.$$

The angular dependence of Raman scattering is included via the factors involving ϕ and θ, where $\phi = \arctan\left(1/(2f\#)\right)$, $\theta = \pi/2 - \phi$. The derivation of the angular dependence is shown in Appendix B. Its method is outlined by Long [25]. The collection f/# of our optics is 5.9 and is determined as discussed in the section on the experimental set-up. The factor $M(v,p)F(v,J,p)$ represents a part of the polarizability matrix element. $M(v,p)$ is the vibrational part of the polarizability matrix element and $F(v,J,p)$ is the Herman-Wallis factor. If we assume a harmonic oscillator and no interaction between the vibrational and rotational states then [24]

$$M(v,p)F(v,J,p) \propto \frac{(v+1)}{\nu(v)} p'^{2}.$$

However, in our most accurate simulations we assume an anharmonic oscillator model and $M(v,p)$ and $F(v,J,p)$ are given by Buldakov *et al*. [42].

$$M(v,p) = \frac{B_e}{\omega_e}(v+1)R_p^2 \times \left\{ p'_e + (v+1)\left(\frac{2B_e}{\omega_e}\right)\left[\left(\frac{11}{16}a_1^2 - \frac{3}{4}a_2\right)p'_e - \frac{5}{4}a_1 p''_e + \frac{1}{4}p'''_e\right]\right\}.^2 \tag{4.6}$$

Here, $p = \gamma$ for anisotropic polarizability and $p = \alpha$ for isotropic polarizability. The values of the polarizability and their derivatives are also obtained from Buldakov, *et al.* [42]. Although the absolute value of the polarizability derivatives is a weak function of excitation wavelength [47], the relative values are quite insensitive to the excitation wavelength. The quality of the curve fit depends on the relative values of the polarizability derivatives so we have used their values in the static limit. Furthermore, the higher order derivatives of the polarizability are not listed at specific wavelengths. The *a*'s are the coefficients in the expansion of Dunham potential; their values are also listed by Buldakov, *et al.* [42]. In the final simulation, we use the same values of the polarizability derivatives and Dunham potential coefficients for both the $^{14}N_2$ and the $^{15}N^{14}N$ isotopes. We assume that the error caused in temperature calculation is negligible

as the reduced masses of the two species are almost equal and the rare isotope is present in a very low proportion. R_p^2 is the factor that accounts for the polarization sensitivity of the optics. It also implicitly compensates for the relatively large uncertainty in the values of the anisotropic polarizability derivatives.

The Herman-Wallis factor, $F(v,J,p)$ accounts for the effect of the interaction between vibration and rotation on the intensity. In the absence of $F(v,J,p)$, the intensity of the *S* branch is overestimated and that of the *O* branch is underestimated in the simulation. For *O* and *S* branches,

$$F(v,J,\gamma) = \left[1+\frac{R_\gamma}{M(v,\gamma)^{1/2}}\left\{\begin{array}{c} m\left(\frac{v+1}{2}\right)^{\frac{1}{2}}\left(\frac{2B_e}{\omega_e}\right)^{\frac{3}{2}} \\ \left\{-2\gamma_e+(v+1)\left(\frac{2B_e}{\omega_e}\right)\left[\begin{array}{c}\left(\frac{9}{2}a_2-\frac{41}{8}a_1^2-\frac{15}{2}a_1-6\right)\gamma_e \\ +\left(\frac{13}{4}a_1+\frac{3}{4}\right){\gamma'}_e-\frac{1}{2}{\gamma''}_e\end{array}\right]\right\} \\ +(m^2+3)\left(\frac{v+1}{2}\right)^{\frac{1}{2}}\left(\frac{2B_e}{\omega_e}\right)^{\frac{5}{2}}\left[-\frac{3}{16}(a_1+1){\gamma'}_e+\frac{1}{4}{\gamma''}_e\right]\end{array}\right\}\right]^2, \tag{4.7}$$

where $m = 2J+3$ for the *S*-branch and $m = -2J+1$ for the *O*-branch. For the *Q*-branch,

$$F(v,J,p) = \left[1+\frac{R_p}{M(v,p)}\left\{m\left(\frac{v+1}{2}\right)^{\frac{1}{2}}\left(\frac{2B_e}{\omega_e}\right)^{\frac{5}{2}}\left[-\frac{3}{4}(1+a_1){p'}_e+{p''}_e\right]\right\}\right]^2, \tag{4.8}$$

where $m = J(J+1)$.

The Herman-Wallis factor given by Tipping and Bouanich [48] is considered to be accurate and it is widely used in the literature [49-52]. We also find comparisons [53, 54] between this form of the Herman-Wallis factor and those given by Buldakov *et al.* [42], as if they have separate origins. However, the expression given by Tipping and

Bouanich is an approximate form of the expression given by Buldakov *et al.* because Tipping and Bouanich provide an approximation to the Herman-Wallis factors given by Tipping and Ogilvie [55]. Buldakov *et al.*'s expression is a function of *v*, which simplifies to Tipping and Ogilvie's expression, which is given only for v=0. Hence, the Herman-Wallis factor given by Buldakov *et al.* is used here as it also accounts for the dependence on the vibrational level. The Herman-Wallis factors are also derived by James and Klemperer [56] assuming a harmonic oscillator, and they are listed for only the fundamental band and their overtones.

The last factor in eqn. (4.1) is the line shape function. The line shape function was determined as follows. Emission lines from a neon calibration lamp were recorded and fitted to Gaussian, Lorentzian and Voigt line shape models but there was still a small but significant systematic error in the shape. The most satisfactory fit was obtained when we used a convolution of a trapezoid function with a Lorentzian; we call this model the *TL* function. The quality of the curve fits to atomic emission lines was equally good when we used a convolution of single step function with a Lorentzian (*SSL*) or a double step function with a Lorentzian (*DSL*). *TL* gave a better fit to a Raman spectrum from room air than did *SSL*. Although *DSL* and *TL* gave equally good fits to the spectrum from room air, the latter was chosen because it has fewer free parameters. Figure 4.1 displays the curve fits to recorded Ne line emission at 603.16 nm using various line shape models, and it illustrates that the *TL* function is the best match to the data. As shown in Fig. 4.1b the residuals (data-fit) are significantly minimized when *TL* function is used. The residuals on only the Gaussian, Voigt and *TL* function are shown so that the figure is legible.

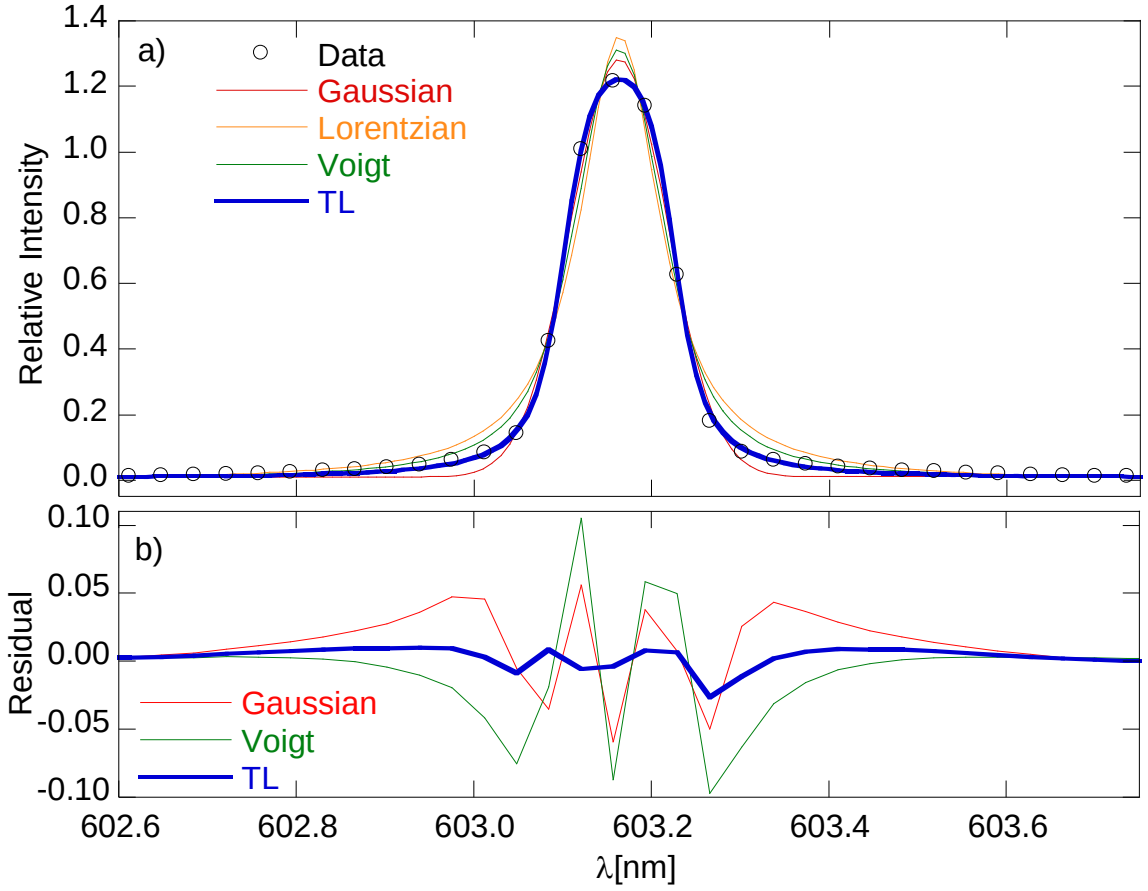

Figure 4.1: (a) Curve fits to a Ne line using some of the line shape models and (b) the residuals in the fits

The functional form of the *TL* is given in eqn. (4.12). The unit normalized trapezoid function is

$$T(x,b,t)=\begin{cases}0, & -\infty<x<-b\\ \dfrac{x+b}{(b+t)(b-t)}, & -b<x<-t\\ \dfrac{1}{b+t}, & -t<x<t\\ -\dfrac{x-b}{(b+t)(b-t)}, & t<x<b\\ 0, & b<x<\infty\end{cases}. \tag{4.9}$$

Here,

$$x = \lambda - \lambda_k, \tag{4.10}$$

b is the base halfwidth , and t (< b) is the tip halfwidth. The unit normalized Lorentzian is

$$L(x, \Delta\lambda_L) = \frac{1}{\pi}\frac{\Delta\lambda_L}{{\Delta\lambda_L}^2 + x^2}. \tag{4.11}$$

The convolution gives

$$\begin{aligned} S(\lambda; \lambda_k(v, J), b, \Delta\lambda_L, t) = {} & \frac{1}{2\pi(b^2 - t^2)} \\ & \times \Bigg\{ (x-b)\tan^{-1}\left(\frac{x-b}{\Delta\lambda_L}\right) \\ & + (x+b)\tan^{-1}\left(\frac{x+b}{\Delta\lambda_L}\right) \\ & - (x-t)\tan^{-1}\left(\frac{x-t}{\Delta\lambda_L}\right) \\ & - (x+t)\tan^{-1}\left(\frac{x+t}{\Delta\lambda_L}\right) \\ & + \frac{\Delta\lambda_L}{2} ln \frac{\left[{\Delta\lambda_L}^2 + (x-t)^2\right]\left[{\Delta\lambda_L}^2 + (x+t)^2\right]}{\left[{\Delta\lambda_L}^2 + (x-b)^2\right]\left[{\Delta\lambda_L}^2 + (x+b)^2\right]} \Bigg\}. \end{aligned} \tag{4.12}$$

Figures 4.2-4.5 show the curve fits on Raman data from nitrogen in room air (T = 295 K) or their residuals (data - fit) by excluding the Q branch from $^{14}N_2$. The Q branch is excluded as it has very high intensity relative to the O and the S branches so that a least-squares curve fit to experimental data that include the Q branch is biased towards minimizing the difference between the simulation of the Q branch intensity and the data. Table 4.1 provides some information on the level of theory in the models used for the simulations. The agreement between data and simulation improves as more theoretical details are included in the simulation. In addition to the theoretical details, the quality of agreement also depends slightly on the values of the polarizability derivatives used in the simulation.

Table 4.1: Level of theory used in the simulation

Figure	Angle dependence	Herman-Wallis factors	Isotope	Anharmonic effects	Polarization sensitivity factor
4.2	×	×	×	×	×
4.3	✓	✓	×	×	×
4.4	✓	✓	✓	×	×
4.5	✓	✓	✓	✓	✓

In the table above × implies exclusion from theory and ✓ implies inclusion in theory. For simulation of scattering from room temperature air, signal from up to $v_{max} = 7$ and $J_{max} = 100$ is calculated for $^{14}N_2$ and up to $v_{max} = 4$ and $J_{max} = 100$ for $^{14}N^{15}N$. For simulation of Raman spectra in flames $v_{max} = 10$ and $J_{max} = 100$ for $^{14}N_2$ and $v_{max} = 7$ and $J_{max} = 100$ for $^{14}N^{15}N$. At 1800 K the vibrational population fraction in $v > 10$ is less than 10^{-6}, and similarly for $J > 100$.

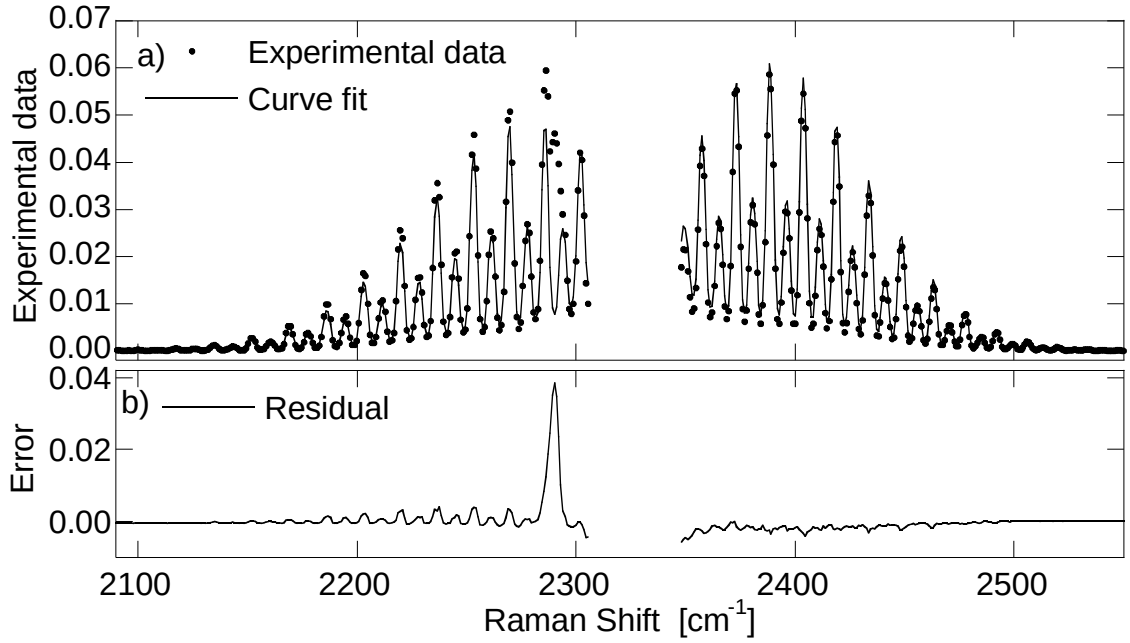

Figure 4.2: Curve fit to *O* and *S* branches from room air and the residuals. Angular dependence, Herman-Wallis factors, scattering from $^{14}N^{15}N$, anharmonic effects and polarization sensitivity factor are excluded from the model.

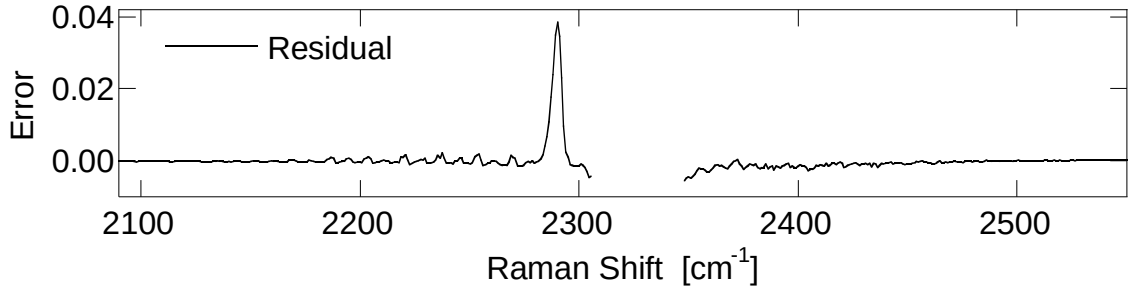

Figure 4.3: Residuals of curve fit to *O* and *S* branch from room air when angular dependence is included but scattering from $^{14}N^{15}N$, anharmonic effects and polarization sensitivity factor are excluded from the model.

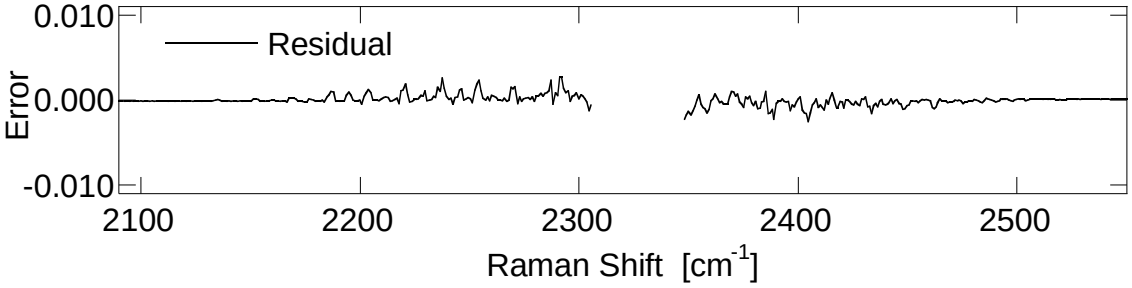

Figure 4.4: Residuals of curve fit to *O* and *S* branches from room air when angular dependence and scattering from $^{14}N^{15}N$ are included but anharmonic effects and polarization sensitivity factor are excluded from the model. Note the expanded scale of the error plot relative to the errors in Figs. 4.2b and 4.3.

The values of the polarizability derivatives α' and γ' used to generate the simulation in Figs. 4.2, 4.3 and 4.4 are obtained from [57]. The specific values are listed in Table 4.2.

Table 4.2: Values of polarizability parameters (in Å^3) for $^{14}N_2$

Polarizability Derivative	Knippers *et al.*[57], (Fig. 4.2)	Maroulis [58], (Figs. 4.2, 4.3, 4.4)	Buldakov *et al.*[42], (Fig. 4.5)
α		1.76	1.77
α'	1.89	1.90	1.86
α''		1.2	1.2
α'''		-6.5	-4.6
γ		0.68	0.71
γ'	2.07	2.16	2.23
γ''		2.5	2.6
γ'''		-4.5	-5.4

In Fig. 4.5, the values of the polarizability derivatives given by Buldakov *et al*. [42] are used.

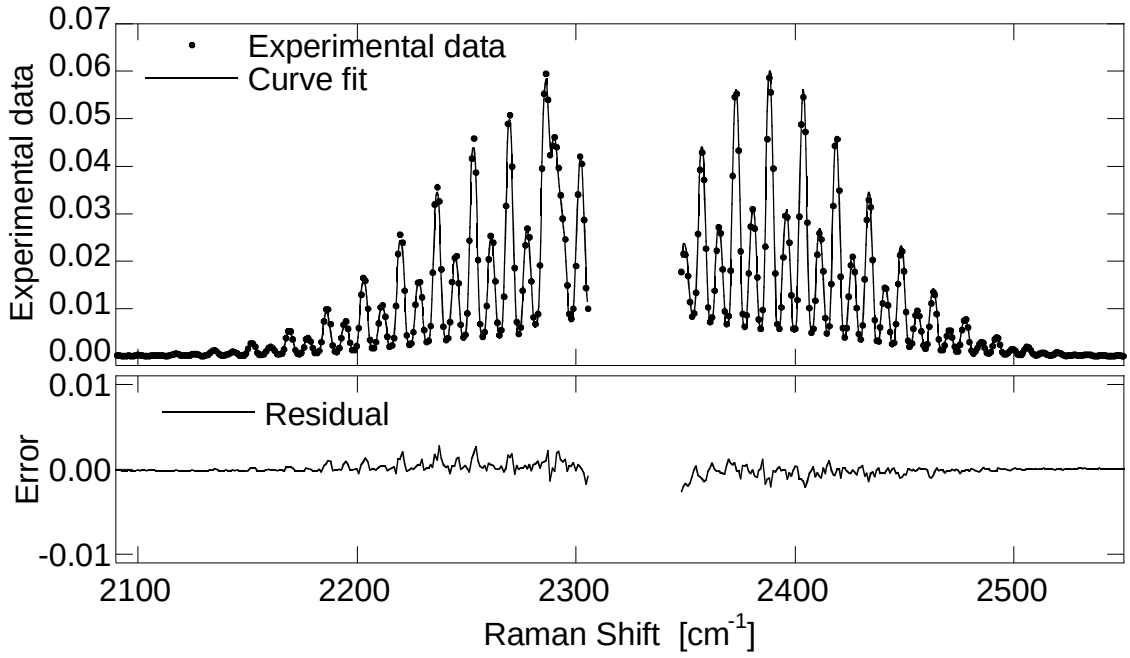

Figure 4.5: Curve fit to *O* and *S* branch from room air with all effects included. Note the expanded scale of the error plot relative to the errors in Figs. 4.2b and 4.3.

In Fig. 4.2, polarizability and its second and third order derivatives are not necessary because those parameters only appear in the expression for Herman-Wallis factors and in the vibrational part of the polarizability matrix elements when anharmonic effects are included. In Figs. 4.3 and 4.4, the Herman-Wallis factors are calculated using the values of polarizability derivatives obtained from a CCSD(T) expansion of dipole polarizability as given by Maroulis [58], and the expression for Herman-Wallis factors given by Tipping and Ogilvie [55] is used. The Herman-Wallis factors given in [55] depend only on the ratio of the polarizability derivatives of a given kind and not their absolute values. The Herman-Wallis factors for the fundamental band are also applied to

the hot bands. In Fig. 4.4, the Herman-Wallis factors used for the $^{14}N^{15}N$ are equal to the corresponding Herman-Wallis factors used for $^{14}N_2$. The α' and γ' for $^{14}N^{15}N$ are obtained from the corresponding values for $^{14}N_2$ by scaling them inversely with the square root of the reduced mass $x_1' = x_2' \left[\frac{m_2}{m_1}\right]^{1/2}$ where x'= α'or γ'; for $^{14}N^{15}N$ α'=1.86, γ'=2.04. This relation between α' and γ' of the different isotopes holds true for several molecular isotopes listed by Polavarapu [59].

It is obvious that the agreement between the data and the simulation improves from Figs. 4.2 to 4.4. Although the most detailed theory is used to generate Fig. 4.5, the residuals are almost indistinguishable from those in Fig. 4.4. We find this to be the case also with the curve fit to the flame data, which indicates that the inclusion of anharmonic effects in the vibrational matrix elements and the inclusion of the dependence of Herman-Wallis factors on the vibrational levels make negligible improvement in the agreement between the data and the simulation for N_2. Figure 4.6 shows the residuals when the *O* and the *S* branches recorded in a flame are fitted simultaneously by applying the theories used in Figs. 4.2, 4.3 and 4.5. The curve fit is performed by floating the line shape parameters, overall scale, overall wavelength shift and the background. The flame temperature is an input parameter, which is determined by following the procedure described in chapter 6. Even when the line shape is well known, floating *T* in a curve fit to *O* and *S* branches from flame is not very reliable because the SNR in the *O* and the *S* branches is low. However, floating the line shape parameters with *T* as a fixed input is more reliable because the lines are well resolved. The curve fit to the *O* and the *S* branches in flame data is performed by excluding the region where the *Q* branches from $^{14}N_2$ are prominent so that they do not produce a bias in the curve fit.

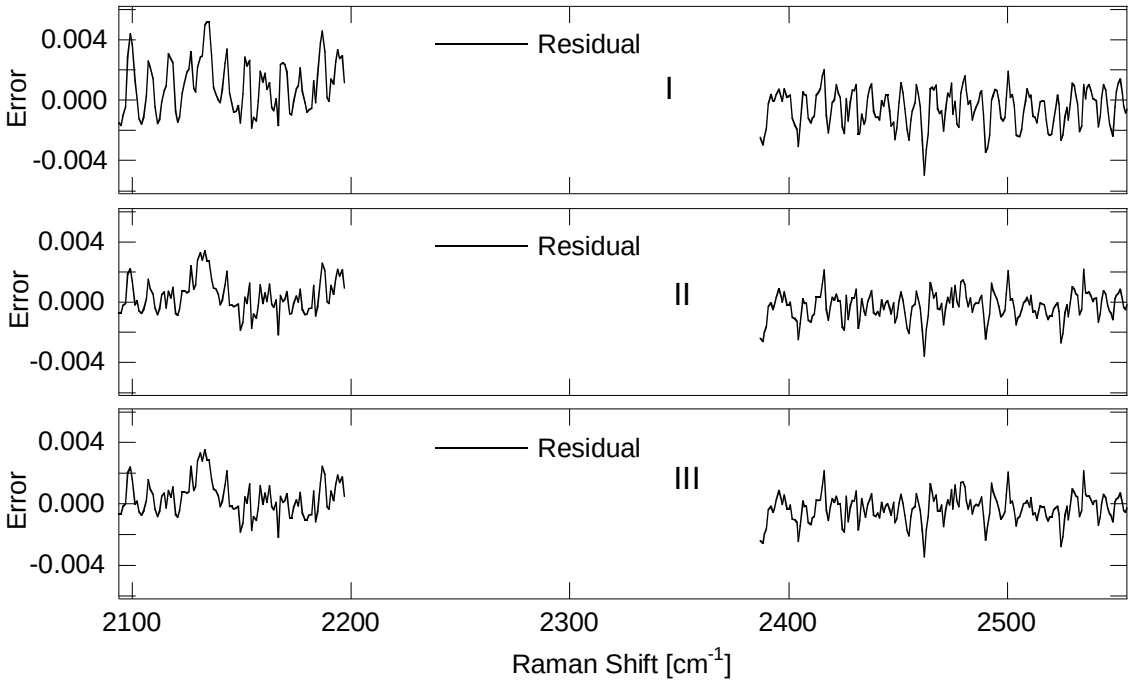

Figure 4.6: Residuals in the curve fit to flame data by using different levels of theory. Theory level of Fig. 4.2 (top--I), Fig. 4.3 (mid--II) and Fig. 4.5 (bottom--III).

The parameters obtained from the curve fit to *O* and *S* branches are used to simulate all the branches. The comparison between these simulations and the data is shown in Fig. 4.7. The systematic discrepancies between the model spectrum and experimental data discernible in Fig. 4.5, and that evident in Figs. 4.7a and b indicate that the relative values of the anisotropic polarizability derivatives (γ'/γ'', γ'/γ''', etc.) available in the literature and used in the simulations here are not accurate. In Figs. 4.7a and b note that the shortcomings of the inferior theory (I) are somewhat compensated by applying a suitable background. The data reported here might be useful to improve the calculated values of the polarizability derivatives. The discrepancy between the predicted and observed intensities of the *Q* branch in Fig. 4.7c is caused by the lack of the polarizability sensitivity factor in the inferior theories (I and II).

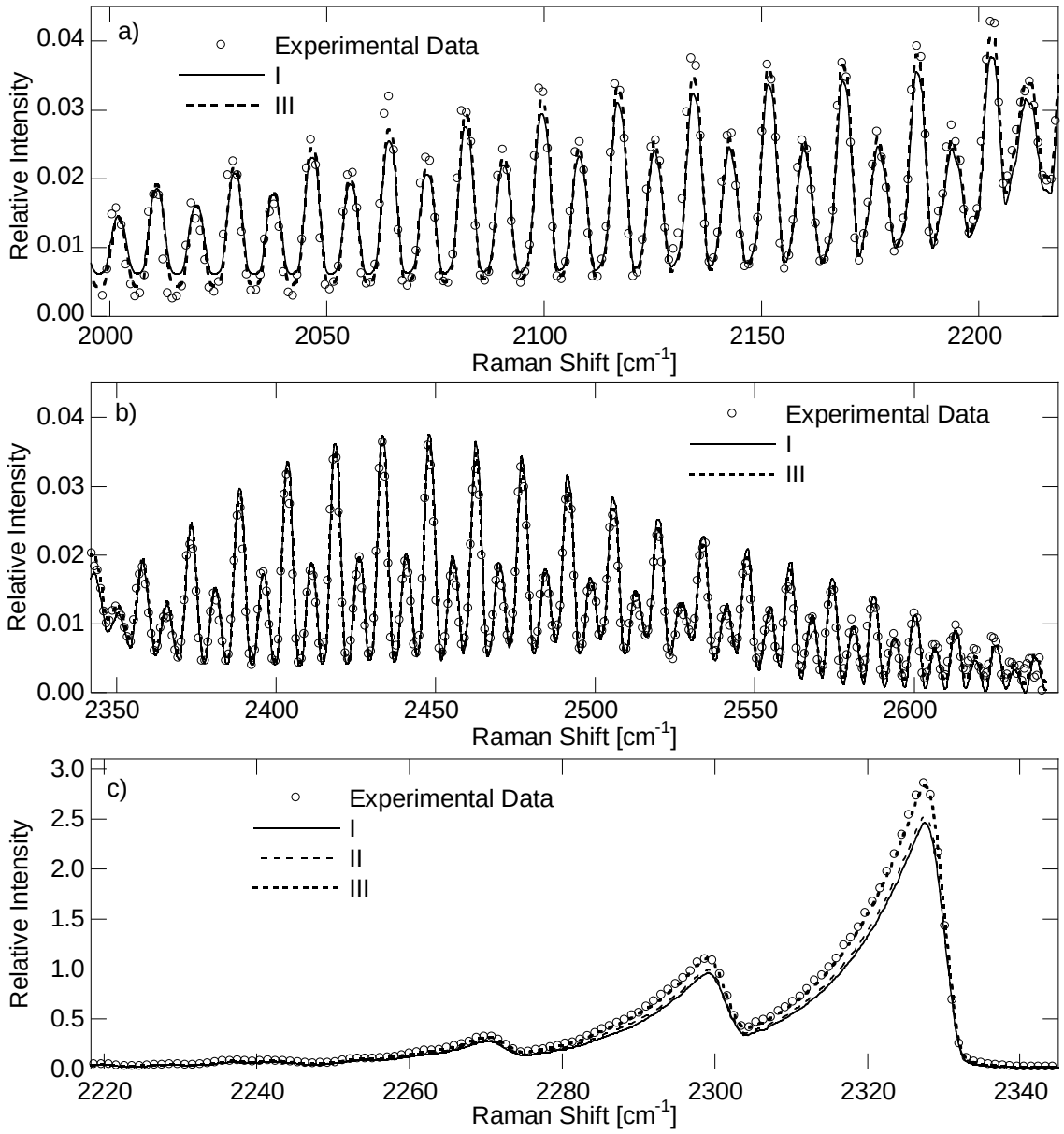

Fig. 4.7. Simultaneous curve fit to (a) *O* branch and (b) *S* branch in flame using the most (III) and the least (I) sophisticated theory by floating the line shape parameters at known temperature. Theory level in simulation II of (c) *Q* branch corresponds to that of Fig. 4.3.

There are additional challenges faced when attempting to determine temperature by curve fits to the *S* and the *O* branches. The value of temperature obtained from fits to

the *S* and the *O* branches is quite sensitive to the values of the line shape parameters used in the simulation so that any inaccuracy in the line shape leads to errors. Such complications which arise in temperature determination are circumvented by including data from the *Q* branch in the curve fit to infer the temperature. When the *Q* branch data are also included, the temperature is predominantly determined by the curve fit to the *Q* branch as it has very high intensity compared to the *O* or the *S* branches. The intensity of the overall background is also very low in comparison to the intensity of the *Q* branch, and the inclusion of the *S* and the *O* branch data help in baseline determination. The temperature extracted from the fit is also less sensitive to the values of the line shape parameters. Thus the most accurate value of temperature is obtained by curve fitting to the *O*, *Q* and *S* branches simultaneously, and hence this procedure is used to obtain the flame temperatures.

The detailed theoretical model used here can be easily modified to simulate Raman scattering from other diatomic molecules. The scattering from H_2 is described in Appendix C.

4.2 SIMULATION OF THE LOW RESOLUTION SPECTRUM

The simulation of the low resolution spectrum was carried out 2 years prior to that of the high resolution spectrum. Since the *O* and the *S* branches are not resolved, the effect of anharmonicity on line intensities, the presence of the isotope and Herman-Wallis factors were not included in the theory. The angular dependence of the scattering was also omitted. These simplifications modify eqn. (4.1) such that now,

$$\phi_{J\to J-2} = \frac{(v+1)}{v(v)}\frac{7}{45}(\gamma')^2\frac{3J(J-1)}{2(2J+1)(2J-1)}, \tag{4.13}$$

$$\phi_{J\to J} = \frac{(v+1)}{\nu(v)}\left[(\alpha')^2 + \frac{7}{45}(\gamma')^2\frac{J(J+1)}{(2J-1)(2J+3)}\right],$$

$$\phi_{J\to J+2} = \frac{(v+1)}{\nu(v)}\frac{7}{45}(\gamma')^2\frac{3(J+1)(J+2)}{2(2J+1)(2J+3)}$$

In the equations above $\nu(v)$ is the molecular vibrational frequency; $(v+1)$ should be replaced with v for the anti-Stokes signal. The labeling of *O* and *S* branches is flipped in the anti-Stokes spectrum so that $J \to J+2$ is the *O* branch and $J \to J-2$ is the *S* branch[12]. In the low resolution spectrum the temperature is inferred from curve fit to the Stokes and the anti-Stokes signal. Each curve fit also yields the total intensity of the Stokes and the anti-Stokes signals which can be compared to obtain the value of temperature. The relative intensities of the anti-Stokes and Stokes signals are proportional to the relative population distribution in the ground vibrational state and the higher vibrational states which is measured macroscopically as temperature. The line shape function is modeled as Voigt function[13]. Its functional form is

$$L\left(\lambda;\lambda_k(v,J),y,\Delta\lambda_D\right) = \frac{1}{\sqrt{\pi}\Delta\lambda_G}V(x;y). \tag{4.14}$$

Here, the Voigt profile is centered at $\lambda_k(v,J)$ [nm] determined from the scattering shift $\nu_k(v,J)$ [cm^{-1}] from the excitation laser wavelength ν_o; y is the normalized broadening parameter given by

[12] As mentioned in chapter 1, this is because the transition label is determined as $\Delta J = J_u - J_l$, where *u* and *l* refer to the higher and lower energy state quantum numbers respectively. ΔJ = -2, 0, 2 for *O*, *Q* and *S* branches respectively.

[13] When we did the low resolution experiments we had not invented the TL function. The aim of the low resolution experiments was to develop and demonstrate the application of the multiple-pass cell for flame temperature measurements; and the aim of the high resolution experiments was to improve the accuracy of the temperature measurements as much as possible.

$$y = \frac{\Delta\lambda_C}{\Delta\lambda_G}, \tag{4.15}$$

and

$$x = \frac{\lambda - \lambda_k}{\Delta\lambda_G}, \tag{4.16}$$

which is the shift from the line center measured in units of $\Delta\lambda_G$, the 1/*e*-Gaussian half-width. The term $\Delta\lambda_C$ represents the Lorentz half-width. The curve fit to Raman spectrum from room temperature air gives $\Delta\lambda_G$ = 0.404 nm and y = 0.450.

Because there is no detectable anti-Stokes signal at room temperature the best line shape parameters could not be determined for the anti-Stokes spectrum in the same way as the Stokes spectrum. Hence, the broadening parameters determined from the xenon lines at 462.56, 467.25 and 469.23 nm, which are near the spectral range of the anti-Stokes Raman signal from N_2 for 532 nm excitation, were retained. The fit gave $\Delta\lambda_G$ = 0.429 nm and a Voigt parameter of 0.232. Although the Voigt parameter (y) used to model the instrument broadening in the anti-Stokes region is substantially smaller than that in the Stokes region, the Gaussian width ($\Delta\lambda_G$) is larger, and as shown in Fig. 4.8 the net result is that the line shape function is not very different. The best-fit values of the two parameters are strongly correlated. We have verified that the quality of the fits to the experimental data is not sensitive to the precise values of the coupled set of parameters ($\Delta\lambda_G$, y) used.

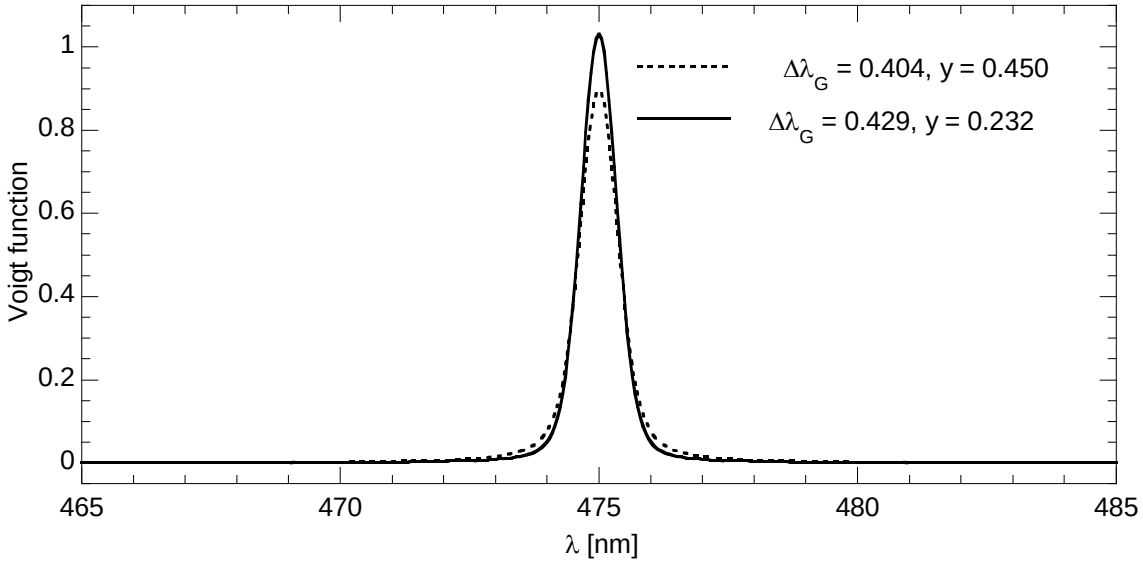

Figure 4.8: Line shapes for the low resolution Stokes and anti-Stokes curve fit.

Chapter 5: Gain Analysis

The purpose of using a multiple-pass cell is to increase the Raman signal and SNR in comparison to the single pass. In this chapter, the gains in signal and SNR obtained in the ring mode and the two point mode are explained.

5.1 SIGNAL GAIN IN THE RING MODE

The ratio of Stokes Raman scattering in room temperature air from a single pass to that from 100 passes was taken to determine the benefits achieved by using the multiple-pass cell. The recorded data are presented in Fig. 5.1.

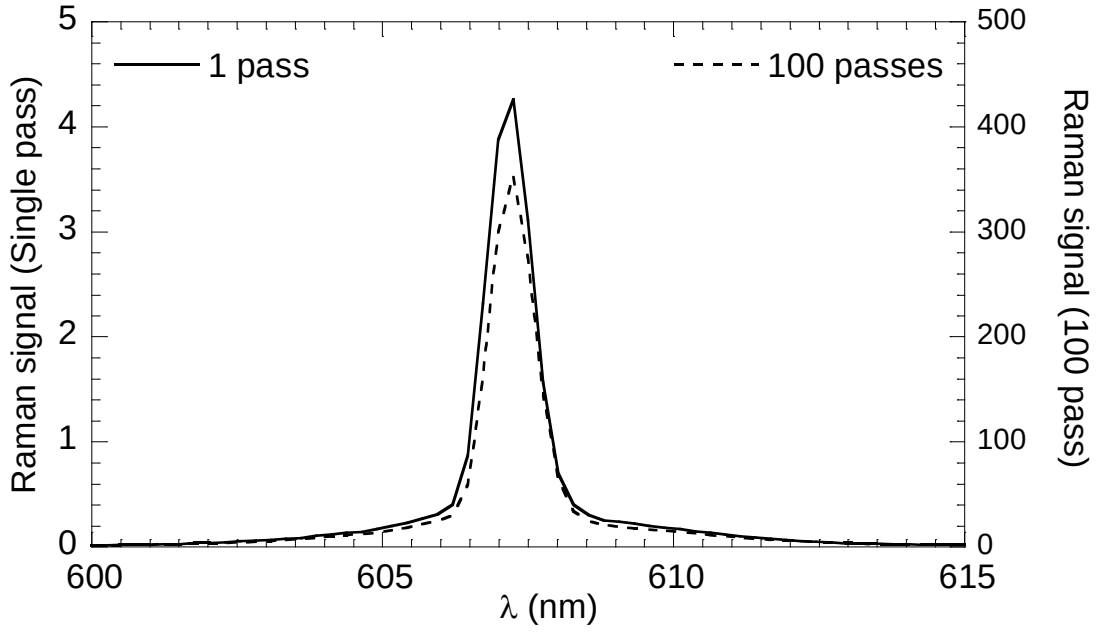

Figure 5.1: Measured Raman scattering signal from room air for a single pass of the Raman cell and for 100 passes

In the ring mode the experiments were carried out at low dispersion. The data shown are recorded for 3×10^4 pulses in each case so that the signal gain can be clearly seen without significant noise in either case. The ratio of areas under the Raman signal from 100 passes to that from 1 pass is 82.5±2. Figure 5.2 shows that the experimental

value compares well with the theoretical signal gains found by integrating the areas under the curves shown in Fig 5.3 [36]. The uncertainty in the experimental value arises from the somewhat subjective decision on the number of vertical pixels on the camera to bin when collecting the signal.

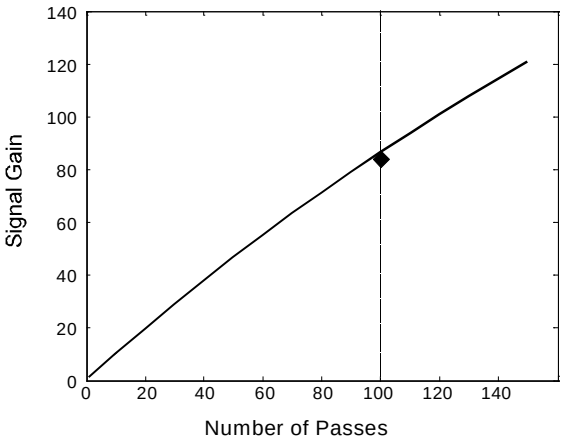

Figure 5.2: Plot of expected signal gain versus number of passes for Raman multiple-pass cell assuming mirror reflectivity of 99.7%. Diamond symbol is measured signal gain for N = 100 [36].

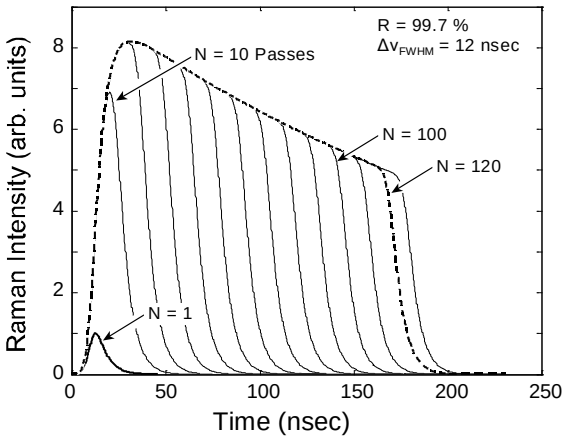

Figure 5.3: Time dependence of laser intensity in Raman imaging volume for 12 ns pulse as a function of N with reflectivity of 99.7 %. Dashed line shows envelope for N = 120 [36].

Figure 5.4 shows the signals as a function of y on the detector summing over x-pixels 770–775; this corresponds to the peak amplitude of the N_2 Stokes Q branch (606.8–608.4 nm). The gain in signal is accompanied by a reduction in spatial resolution, but the signal amplification by a factor of ~80 more than offsets the reduction in vertical spatial resolution by a factor of ~2. One could bin selected pixels on the camera and obtain equivalent spatial resolution with substantial improvement (~40) in signal amplitude. The gate width is set to 15 ns to collect signal from one pass and 165 ns to

obtain signal from 100 passes. Thus the single pass measurements are not penalized by collecting interference when the laser pulse is no longer in the field of view.

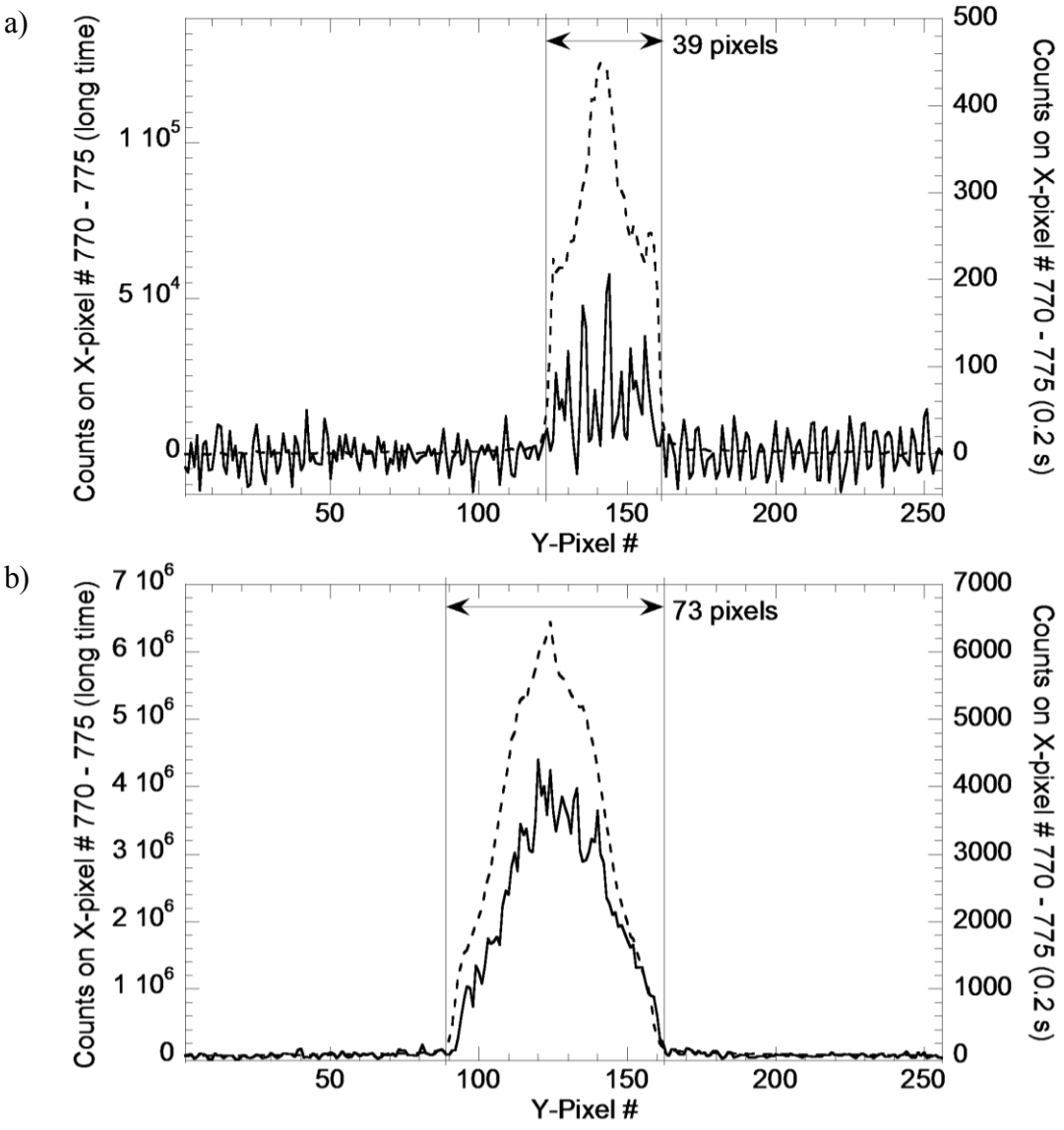

Figure 5.4: Comparison of the (a) 1 pass and (b) 100 pass signals in the region of the N_2 Stokes *Q* branch in room temperature air integrated over the same time intervals: ---- long time (3×10^4 pulses) and — short time (20 pulses). Note the difference in scales between (a) and (b).

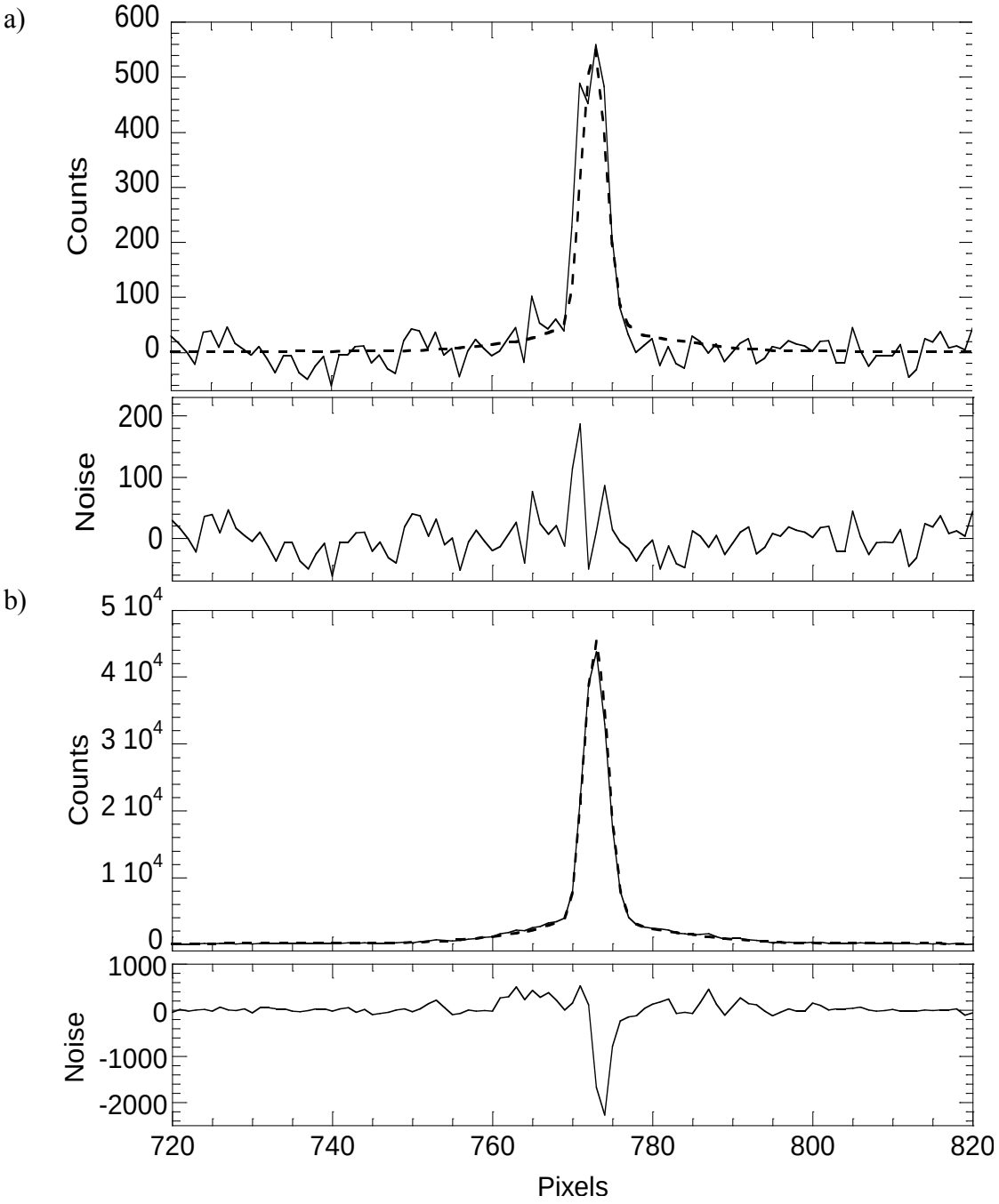

Figure 5.5: Comparison of the (a) 1 pass (SNR=16.4) and (b) 100 pass (SNR=153.4) signal and noise traces for the N_2 Stokes *Q*-branch in room temperature air integrated over the same time intervals: ---- long time (3×10^4 pulses) (virtually noise free); — short time (20 pulses). The SNR improves by a factor of 9.3 for the 100 pass configuration.

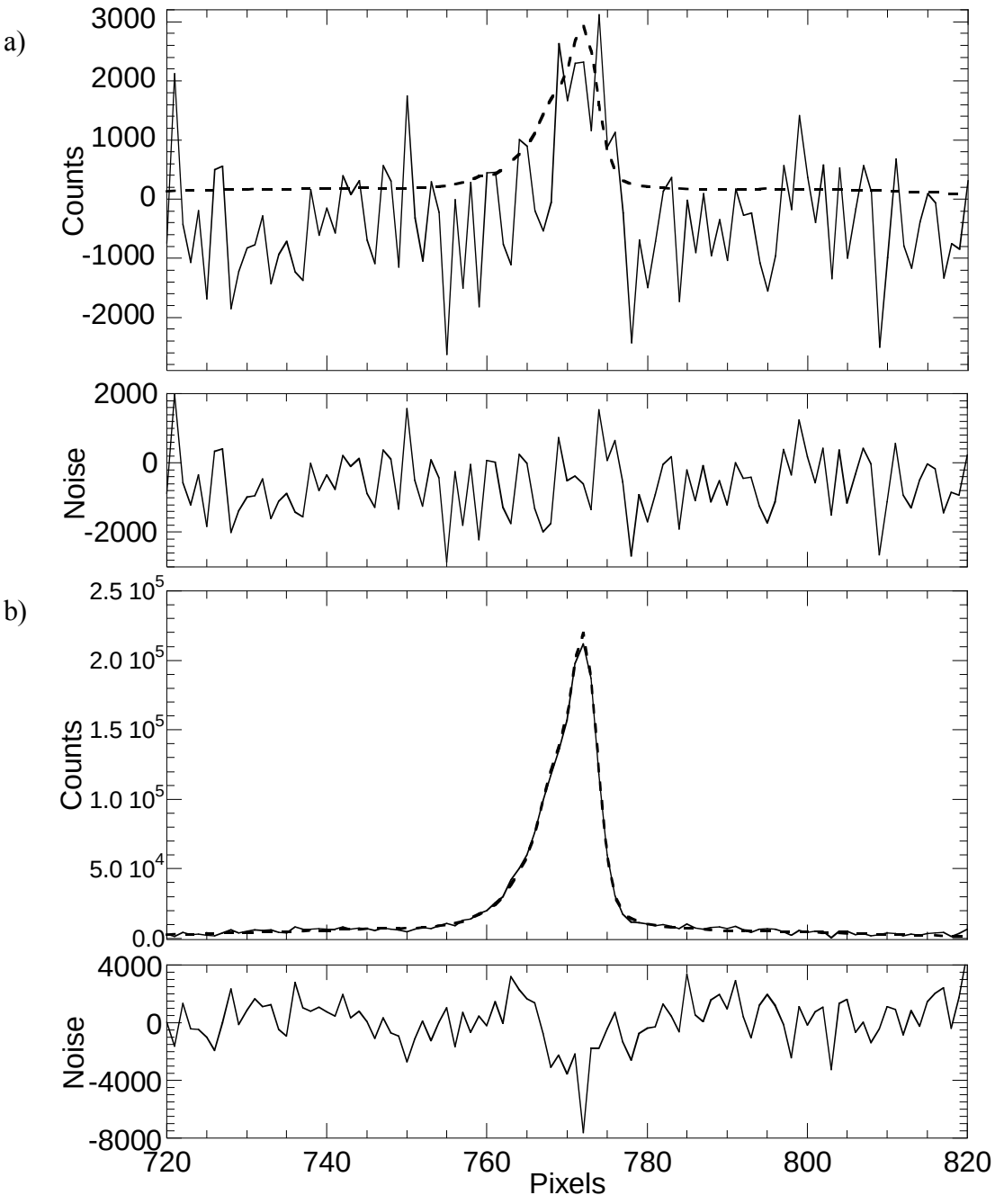

Figure 5.6: Comparison of the (a) 1 pass (SNR=2.47) and (b) 100 pass (SNR=134.9) signal and noise traces for the N_2 Stokes *Q*-branch in a flame integrated over the same time intervals: ---- long integration time (10^5 pulses) (nearly noise free); — shorter integration time (10^3 pulses). The SNR improves by a factor of 54 for the 100 pass configuration.

While signal amplification is desirable, improvement in SNR is more critical. Figure 5.5 shows a comparison of the signal and noise for single pass and 100 pass measurements. The data presented are for the Stokes branch of N_2 obtained in room-temperature air. The noisy data correspond to the signal from 20 pulses, while the smooth data are for 3×10^4 pulses scaled down by a factor of 1500. We compute the noise from the difference between the two data sets rather than from a model spectrum, so that there is no bias introduced from modeling error. The rms of the noise (33.3 and 296 counts respectively) is determined from computed noise amplitude in each case. From the appearance of the noise signals it is clear that the single pass data for 20 pulses have significant read-out noise, whereas the 100 pass data are close to shot-noise limited. The SNR is determined from the peak signal amplitude of the scaled long term average divided by the rms noise amplitude of the 20 pulse signal. The SNR for the single pass and 100 pass measurements are 16.4 and 153.4 respectively. Thus the SNR improves by a factor of 9.3. This is slightly higher than the improvement that would be expected from the improvement in signal amplitude ($82.5^{1/2} = 9.1$) because of the readout noise in the single pass data.

We find that the SNR improves by a higher factor in a flame. Figure 5.6 shows a comparison of the signal and noise traces for single pass and 100 pass measurements of the Stokes branch of N_2 obtained in a near-stoichiometric flame. The noisy data correspond to the signal from 1000 pulses, while the smooth data are for 10^5 pulses scaled down by a factor of 100. As before we eliminate bias due to modeling error by treating the 10^5 pulse trace as noise free and computing the noise from the difference between the two data sets. Because the single pass data were still somewhat noisy after integrating 10^5 pulses, this trace was digitally filtered to give a better approximation to a noise-free signal. The SNR for the flame measurements is determined from the peak

signal amplitude of the scaled long term average divided by the rms noise amplitude of the 10^3 pulse signal. With this definition we obtain SNRs of the Stokes signal of 2.47 and 134.9 for single pass and 100 pass measurements respectively. This is an improvement by a factor of 54. The SNRs are approximately 28 and 708 respectively when the signal is integrated over 10,000 laser pulses, which is an improvement of a factor of 25. The improvement could be driven down to the shot noise limit if one could integrate over a sufficiently large number of laser pulses on the camera, so that the readout noise is negligible compared to shot noise for the single-pass configuration. However, there is obviously no reason to degrade both temporal resolution and SNR improvement, provided the absolute SNR is adequate. Thus, for measurements with the best possible temporal resolution, the SNR improvement with the multi-pass arrangement is even greater for flame measurements than room temperature measurements, because the multi-pass configuration increases the signal level above the read-out noise to the shot noise limit.

5.2 SIGNAL GAIN IN THE TWO-POINT MODE

In the high resolution two-point mode, comparisons are made between the signals integrated over the central 6 pixels along the non-dispersion axis. The spectrum acquired over single pass was noisy even when it was recorded over 100,000 pulses. This was obvious particularly in the *O* and the *S* branches in room air and the hot bands in the flame. So, it was not appropriate to scale down the spectrum acquired over 100,000 pulses to compute the noise level in the spectra acquired over fewer pulses. The noise was determined by comparing the calibrated data with the most detailed simulation. For consistency, the noise in the spectra obtained from multiple passing was also calculated by comparing data with the simulation. Spectra were simulated by curve fitting the data

with temperature, line shape parameters and overall wavelength shift as the input parameters and the overall scale, background slope and offset as floating parameters. The results are summarized in Table 5.1.

Table 5.1: Gain in signal and SNR relative to single pass

	# laser pulses	Signal gain	SNR (Multiple-pass)	SNR (Single pass)	SNR gain
Flame	1000	20.5	139	18.6	7.5
	5000	24.4	238	60.4	3.9
	10,000	23.4	275	74.7	3.7
	100,000	22.2	376	126	3.0
Room air	20	16.3	95.0	5.35	18
	50	19.9	194	8.42	23
	100	22.1	367	17.1	21
	100,000	21.2	666	457	1.5

As shown in Table 5.1, the multiple-pass cell amplifies the signal by approximately 20 times. The gain in SNR is higher when the signal is acquired over fewer laser pulses. This is because the single pass signal acquired over fewer laser pulses has significant proportion of read out noise. As the number of pulses is increased the single pass data contains less proportion of noise and so the gain in SNR decreases.

Chapter 6: Temperature Measurement

6.1 Temperature from the ratio of Stokes to anti-Stokes signal

Our first approach to measure temperature was by comparing the Stokes signal which appears at around 607 nm with the anti-Stokes signal which appears at around 473 nm. The value of temperature obtained by measuring the ratio of intensities of the Stokes and anti-Stokes signals is compared with the temperature measured by the thermocouple, temperature inferred by curve fitting to the Stokes signal and the temperature inferred by curve fitting to the anti-Stokes signal.

Some typical spectra recorded at low dispersion are shown in Fig. 6.1. In principle, there are several ways to compute the value of temperature from these spectra. One can curve fit to the spectrum of one of the molecular species, multiple species or compare the Stokes and anti-Stokes signals of a given species. Comparison between Stokes and anti-Stokes of N_2 is chosen because it is present in all the flames, it has the strongest signal and it has minimum cross talk with other species.

Figure 6.2 shows the vibrational Stokes and anti-Stokes spectra from N_2 in near stoichiometric flame. The signals were recorded and integrated over 64 exposures using the camera software. The alignment of the multiple-pass cell is in the ring mode. Each exposure recorded signal from 300 laser pulses, and the gate width was 165 ns for each pulse. The spectra in Fig. 5.2 are generated by vertically binning over 41 pixels.

The curve fits to the calibrated Stokes and anti-Stokes data in Figs. 6.2a and 6.2b are undertaken separately. Overall scale, overall line shift, baseline offset, slope and temperature are the free parameters for curve fitting. The line shape parameters are the input parameters. As mentioned in Chapter 4, they are determined either by curve fitting the Stokes signal from room temperature air or by curve fitting the emission lines of xenon near 473 nm. The curve fit to the Stokes signal from room air is shown in Fig. 6.3.

In this fit, the line shape parameters, the background offset and slope were floating parameters and the overall scale, wavelength shift and temperature were input parameters.

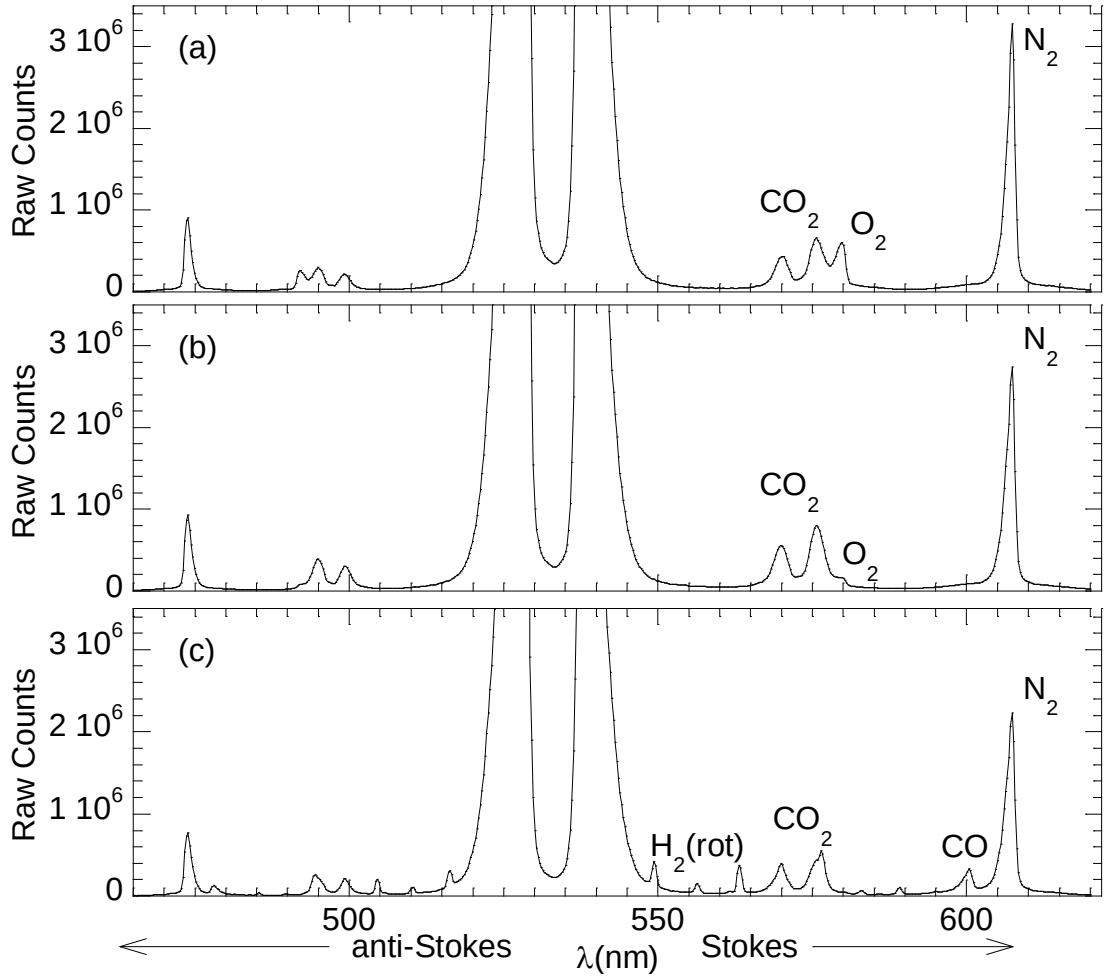

Figure 6.1: Raman spectra in post flame gases of (a) lean ($\phi = 0.66$), (b) near stoichiometric ($\phi = 0.94$), and (c) rich ($\phi = 1.24$) methane-air flames over the flat flame burner.

The Stokes spectrum in Fig. 6.2a is wider than the Stokes spectrum in Fig. 6.3 because the hot bands are also intense at high temperatures. However, the changes in the

shape of the spectrum with temperature are small, and so we believe that the temperature obtained from the curve fit to the low dispersion spectra are not as accurate as the temperature obtained from the ratio of the Stokes to anti-Stokes signal. Nevertheless, the curve fit is necessary even to compute the total intensity of the Stokes or anti-Stokes signal.

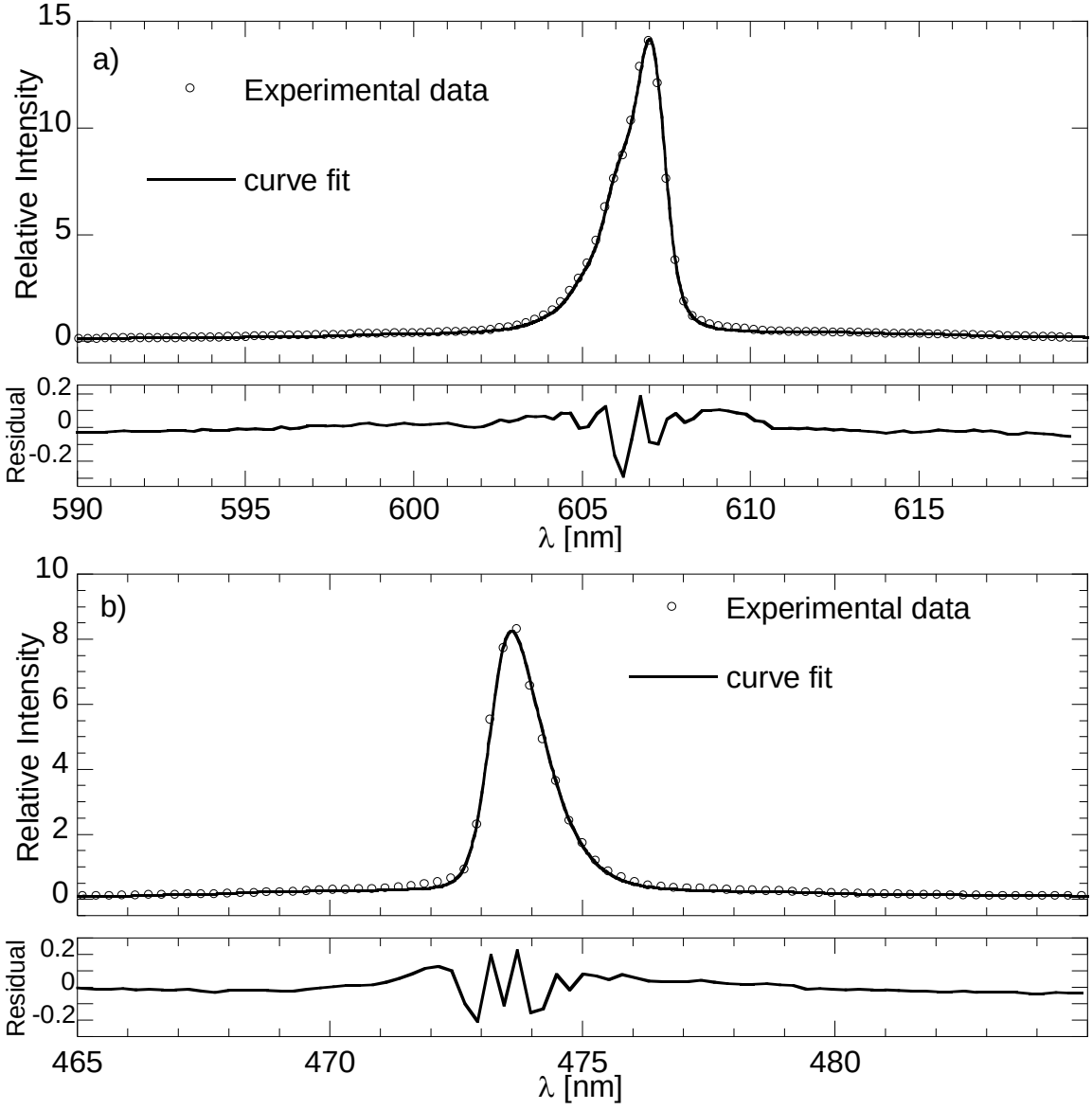

Figure 6.2: Curve fit to N_2 Raman signal obtained in the 100 pass configuration when (ϕ = 0.94). (a) Stokes and (b) anti-Stokes.

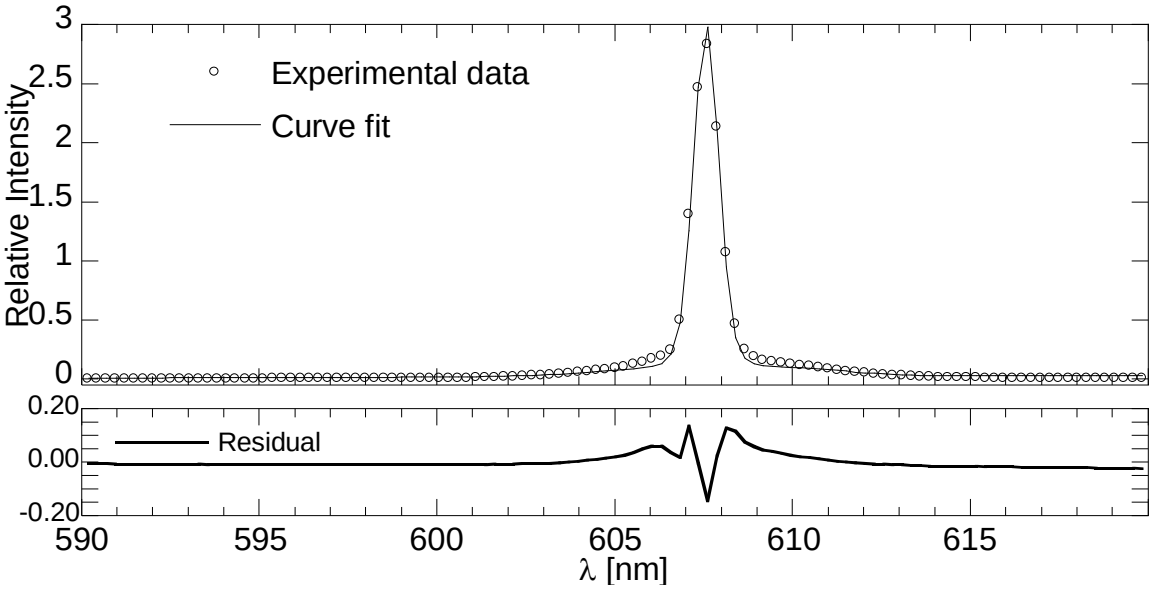

Figure 6.3: Room temperature Stokes spectrum of N_2 and best-fit simulation using instrumental broadening parameters determined from these data

The ratio of Stokes and anti-Stokes signals gives a measurement of the temperature that is independent of the temperature determined from the "shape" of the Stokes and anti-Stokes spectra. Measurements were made for two separate series of experiments at four equivalence ratios. Thermocouple measurements were made near simultaneously in each case. The thermocouple measurements agreed to within the precision of the measurement. For each measurement the temperature was estimated separately from the fit to Stokes spectrum (T_{Sj}), the anti-Stokes spectrum (T_{aSj}) and the ratio of areas (T_{ARj}), where j = I or II for the series of experiments. The results are presented in Fig. 6.4. The radiation corrected thermocouple temperature measurements are also shown (T_j). The calculation of radiation correction is explained in Appendix A. For clarity the thermocouple measurements have been slightly displaced to the right so the symbols can be distinguished more easily. The thermocouple and Raman temperature measurements agree to well within the estimated uncertainty of the measurements.

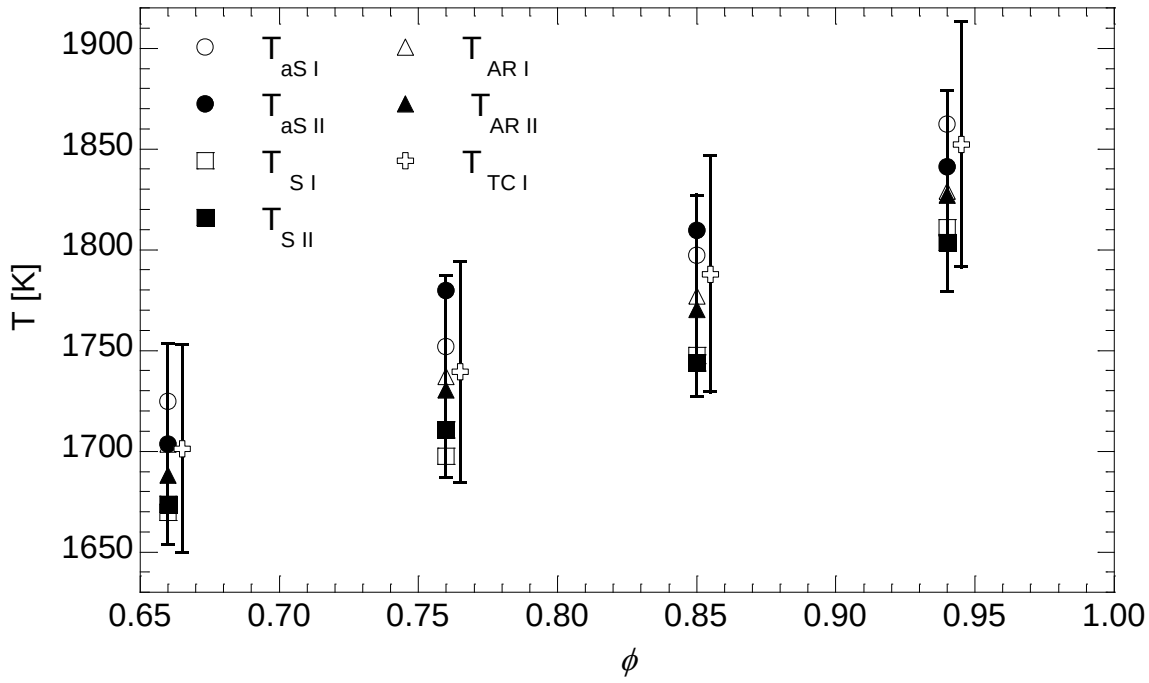

Figure 6.4: Temperature of flame from Raman thermometry and radiation corrected thermocouple measurements. The thermocouple measurements have been slightly displaced in ϕ for clarity.

The bead diameter of the thermocouple was 267 μm. The corrected thermocouple temperature was calculated by assuming radiation loss to ambient and burner surface following the procedure described by Bradley and Matthews [50]. Conduction losses from the thermocouple bead are assumed to be negligible because a substantial length (2.5 cm) of the 127 μm diameter thermocouple wires is exposed to the post-flame gases of the flat flame burner (6 cm diameter). The emissivity of the wire at flame temperatures is estimated to be 0.2, which is calculated using the expression for emissivity as a function of temperature and wire resistivity [50, 61]. The value of resistivity at flame temperatures is obtained from Vines [62]. The values of viscosity, thermal conductivity and thermal diffusivity of the post flame gases were obtained iteratively from Gaseq [63].

When computing the radiation correction we assumed that 15% of the bead surface was obstructed by the thermocouple leads and hence could not radiate. However, it was assumed that the entire bead surface was effectively available for convective heat transfer as there is heat transfer to the thermocouple leads. It was also assumed that 36% of the thermocouple field of view was the burner surface which reached an equilibrium temperature depending on the equivalence ratio. The burner surface temperature measured using the thermocouple was 738 K, 653 K, 563 K and 396 K for equivalence ratios of 0.94, 0.85, 0.76 and 0.66 respectively. The computed radiation correction was about 200 K and was not very sensitive to the assumptions made in the calculations. The estimated uncertainty in the radiation correction is ±30% (±50–60 K depending on temperature) arising from an estimated uncertainty of ±25% in the heat transfer correlation, ±10% in thermocouple emissivity, and ±10% in the gas properties, and additional uncertainty in the precise geometry of the thermocouple bead.

Although the higher vibrational states are not resolved, the shapes of the spectra give temperatures (T_S and T_{aS}) that agree within the estimated uncertainty with the temperature determined from the ratio of Stokes and anti-Stokes intensities (T_{AR}). Figure 6.4 shows that T_S is consistently a little lower and T_{aS} is consistently a little higher than T_{AR}. The reason for this discrepancy is not yet known, but it may be due to errors in the line shape parameters used in the simulations, or to small systematic errors in the model. The area ratio is insensitive to modeling details and is believed to provide the most reliable estimate of temperature. The uncertainty in the temperature measured by this method is ±50 K estimated from the spread between the temperature determined from the area ratio and that determined from the fit to the Stokes and anti-Stokes spectra.

6.2 TEMPERATURE FROM CURVE FIT TO HIGH RESOLUTION STOKES SPECTRUM

The curve fit to a N_2 spectrum measured at high dispersion in a near-stoichiometric flame is shown in Fig. 6.5.

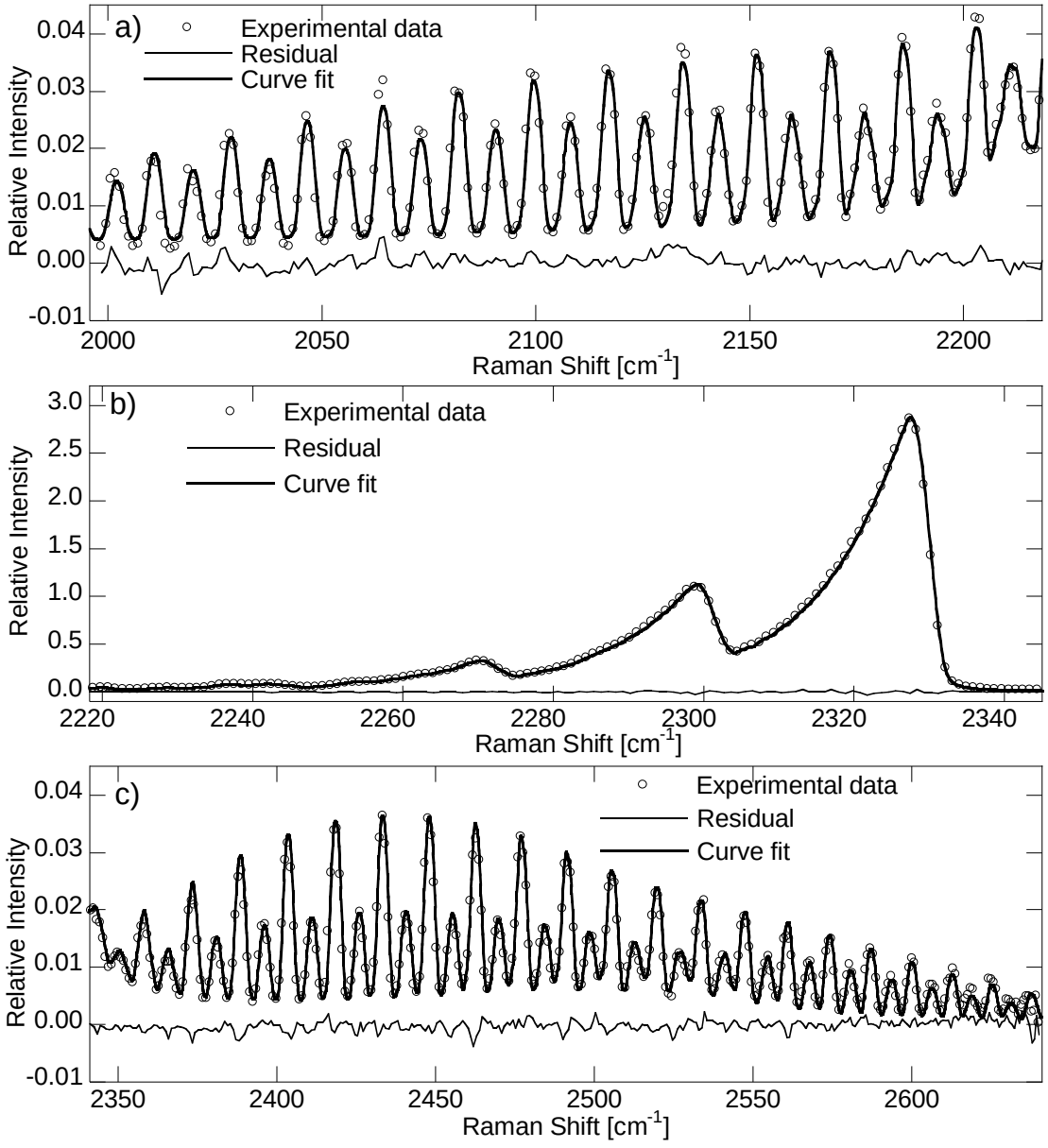

Figure 6.5: Simultaneous curve fit to (a) *O* branch, (b) *Q* branch and (c) *S* branch from flame for temperature determination.

The regions where the *O*, *Q* and the *S* branches are most intense are shown separately as the *O* and the *S* branches have very low intensity in comparison with the *Q* branch. The data were obtained from 100,000 laser pulses (50 exposures of 2000 laser pulses). The raw spectrum was binned over the central 6 pixels of the upper point along the non-dispersion axis. The probe region for the upper point is about 1.5 cm above the surface of the burner. After the calibration the spectrum was scaled appropriately for curve fitting. The curve fit was performed simultaneously over the entire spectral range (595-620 nm). The line shape parameters are the input parameters in the curve fit; the temperature, overall scale, overall wavelength shift, background offset and slope are the floating parameters.

The line shape parameters in the flame are determined as follows. Having determined the proportion of $^{14}N^{15}N$, first the curve fit is performed on the *O* and the *S* branch from room air in the absence of the *Q* branch from $^{14}N^{15}N$ and $^{14}N_2$. The exclusion of the region where the *Q* branch from $^{14}N^{15}N$ is most intense helps to reduce the inaccuracy in the values of the line shape parameters arising from uncertainty in the proportion of $^{14}N^{15}N$ in the mixture. The omission of the region where the *Q* branch from $^{14}N_2$ is the most intense helps the fit to be more sensitive to the values of the line shape parameters as the peaks in the *O* and *S* branches are much better resolved than in the *Q* branch. The line shape parameters for room air are used as the initial input values of the line shape parameters for curve fitting the flame data to obtain a value of the flame temperature. The recorded line shapes of flame Raman spectra are expected to be slightly different from the room temperature spectra because the dispersion is sufficiently high that the molecular line shape is non-negligible compared to the instrumental line shape. As already explained in the chapter on Raman simulation, the most reliable value of temperature is obtained from the simultaneous curve fit to the *O*, *Q* and *S* branches. This

value of temperature is used as an input parameter to curve fit to the flame spectrum with only the *O* and *S* branches. The new values of the line shape parameters are then used as the input parameters to curve fit to the spectrum from flame with *O*, *Q* and *S* branches to obtain a new value of temperature, which is again used to curve fit to the flame spectrum with only the *O* and *S* branches. This process is iterated until the values of the line shape parameters and the temperature converge. This type of fit procedure accounts for any possible differences between the line shape parameters in the flame and in the room air. In Fig. 6.5 the final value of temperature is 1774 K and the line shape parameters are b = 0.103 nm t = 0.030 nm, and $\Delta\lambda_L$ = 0.011 nm. These values of the line shape parameters which are deduced from the spectrum acquired over 100,000 pulses are also used as input parameters to curve fit to the data acquired over fewer laser pulses.

The uncertainty in the value of temperature can be attributed to two main sources. It arises from noise in the data and from the limitations of the model used for simulation. The effect of each source is analyzed separately. First, the uncertainty caused by the noise in the data is characterized.

Table 6.1 shows the value of temperature obtained from curve fit as the total number of laser pulses and thus the SNR is varied. The SNR is defined as the ratio of peak intensity to r.m.s of the noise. The signal acquired over long exposure (100,000 pulses) is treated as the noise free signal. It is scaled down by a factor of 100000/n to compare it with data obtained from n pulses. Peak intensity is the maximum intensity in the scaled down version of the spectrum acquired over long exposure. Noise is defined as the difference between the scaled down long term data and the data acquired over n pulses. This prevents bias arising from errors in modeling the spectrum. The metered mixture of methane and air was held fixed for all the experiments. The McKenna burner was constantly cooled by running water and so stable operating conditions are assumed.

Table 6.1: Temperature from curve fit for different values of SNR

Number of pulses	SNR	T [K]	ΔT [K]
100,000		1774	
10,000	468.2	1780	+ 6
6000	300.4	1796	+22
1000	186.8	1756	–18
500	73.8	1785	+11
200	43.0	1814	+40
100	35.9	1837	+63
50	32.9	1660	–114
20	23.0	1652	–122
10	15.1	1976	+202

According to Table 6.1, an SNR of ~500 is necessary for $\Delta T \lesssim 10$ K. Measurements were repeated with 100,000, 1000 and 100 pulses over several runs. These second set of experiments were carried out many months after the set reported in Table 6.1, and so a slight drift in the calibration of the rotameters, imperfect repeatability of flow rates, and changes in the alignment of the experimental set-up are not unexpected. The curve fit revealed that the new spectra are shifted by 0.047 nm, which is a little less than 2 pixels. Three sets of data were acquired over 100,000 pulses and 50 sets of data were acquired over 1000 and 100 pulses. The values of the temperature inferred from data acquired over 100,000 pulses are 1750, 1752 and 1748 K, which indicate that the metered equivalence ratio of the CH_4 and air is not exactly the same as that for the cases in Table 6.1. More importantly, it also indicates that the SNR in the data acquired over 100,000 pulses is high enough to not affect the calculation of temperature. The values of deviation of temperature from 1750 K obtained from 1000 and 100 pulses are shown in Fig. 6.6; $\Delta T = T$ - 1750 K.

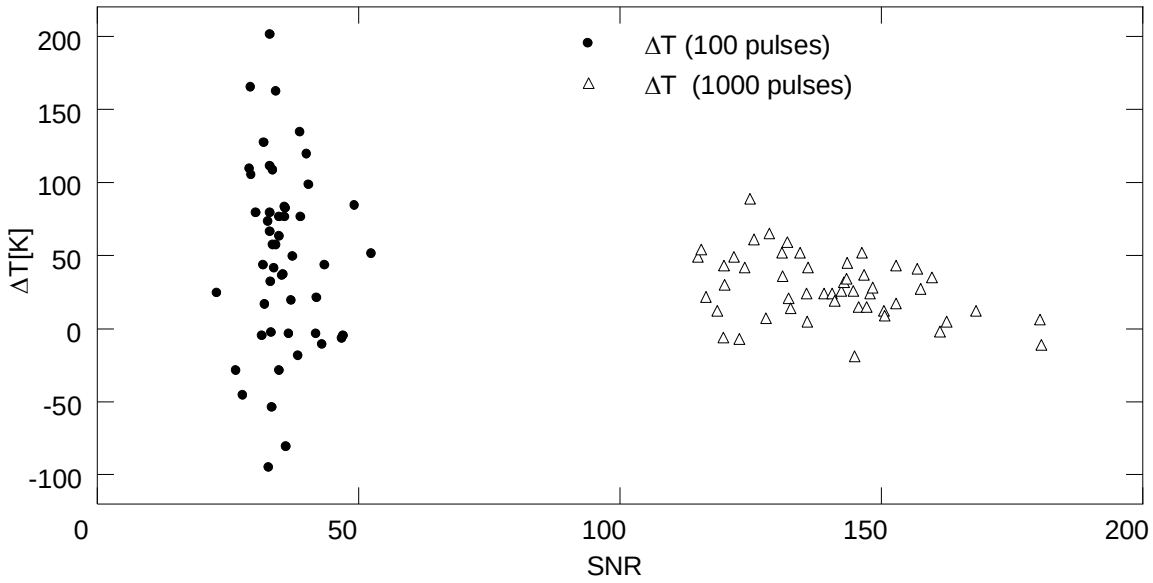

Figure 6.6: Errors in the value of inferred temperature in the spectra acquired over 100 and 1000 pulses

In the data acquired over 1000 pulses the average value of ΔT = 28 K, the std. deviation is ±22 K, and the range is -19 K to 89 K. Similarly, for 100 pulses the average value of ΔT = 48 K, the std. deviation is ±63 K, and the range is -95 *K* to 201 *K*. The reason $\Delta T > 0$ in the majority of the cases can be explained by referring to Table 6.2. Here, v = 0, 1 and 2 refer to the fundamental band, the first and the second hot bands respectively. First, the nearest pixels that correspond to the peaks of the fundamental, the first and the second hot bands are identified, and then we bin over 10 neighboring pixels which are closest to the pixel that contains the peak of a band. The ratio of the mean to the standard deviation of the total counts in the region dominated by a band represents the signal to noise ratio in the band. The hot bands are noisier compared to the fundamental band. The intensity of the hot bands is likely to be more enhanced by the relatively higher proportion of noise and so the temperature is most often overestimated. In the case of data from 100 pulses, there are more frequent occurrences of $\Delta T < 0$ than in the data from

1000 pulses. This is because in the former the fundamental band is also quite noisy and so in some instances it appears relatively more enhanced than the hot bands, and this leads to lower value of inferred temperature. In this way, depending on the noise level in the individual bands $\Delta T < 0$ or $\Delta T > 0$, but the latter is more common.

Table 6.2: Signal to noise in the fundamental band and the first and second hot bands

v	Mean/Std. Deviation (100 pulses)	Mean/Std. Deviation (1000 pulses)
0	16.6	43.0
1	10.1	30.9
2	6.8	19.5

Now, we discuss how the temperature inferred using the model is affected by the uncertainty in the instrument line shape parameters. This type of uncertainty is specific to our set-up. The tests are carried out on the least noisy experimental data of Table 6.1 for which T is 1774 K. The line shape parameters used as the input to calculate the value of temperature were obtained by curve fitting simultaneously to the O and the S branches. Two additional sets of line shape parameters were obtained by curve fitting to the O and the S branches separately. Their values are tabulated below.

Table 6.4: Possible values of the line shape parameters in the flame

Data	b [nm]	t [nm]	$\Delta\lambda_L$ [nm]
O and S branch	0.103	0.030	0.011
O	0.099	0.033	0.012
S	0.100	0.031	0.016

According to Table 6.4, b varies by $\pm$2%, t by $\pm$5%, and $\Delta\lambda_L$ by $\pm$20% .When the S branch parameters (broadest line shape) are used to curve fit the experimental data the temperature inferred from the fit is 1759 K. When the O branch parameters (narrowest line shape) are used the temperature is 1776 K, and when the average line shape parameters are used the inferred temperature is 1768 K. So, a systematic decrease

in inferred temperature is observed as the model line shape gets broader. The uncertainty in the values of the line shape parameters leads to uncertainty of ±9 K in the inferred temperature. The line shapes are shown in Fig. 6.7.

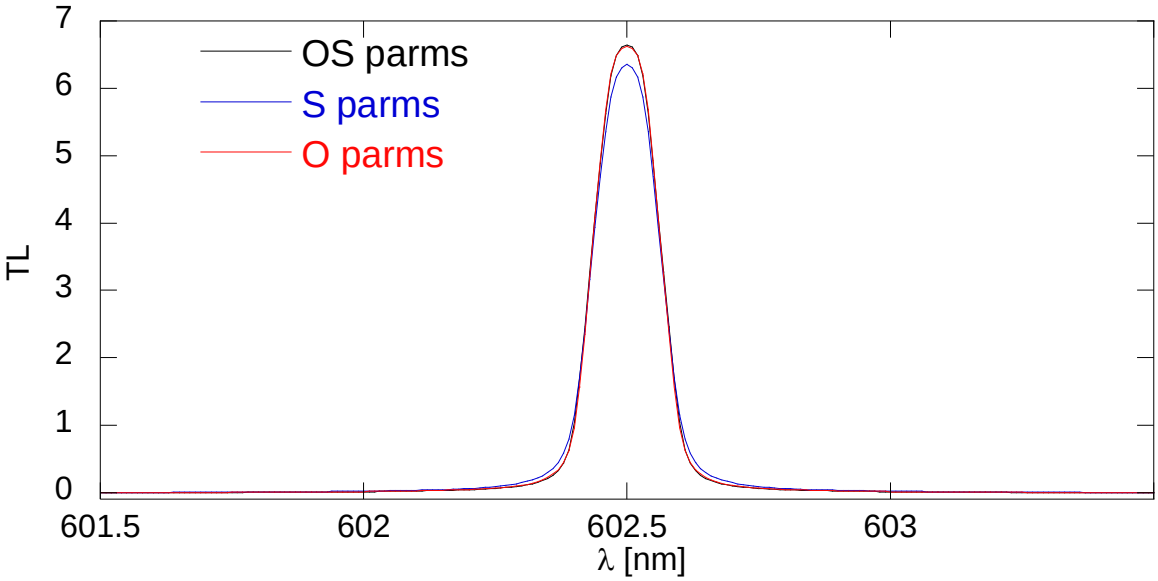

Figure 6.7: Line shapes of the *S*, the *O* branches and the combination of the *S* and *O* branches.

Now, we estimate how the value of temperature changes as a result of slight modifications of Raman theory in the model. Since we are comparing various models here the curve fit is done on a simulated spectrum which is generated using the most sophisticated model that is currently used to simulate the spectrum. The simulated spectrum does not have any background intensity, and so in the curve fit only the overall scale and temperature are set as floating parameters. We have verified that even if the background was included the same results would be obtained. The slope and the offset parameters are not coupled with the temperature. Table 6.3 lists the modifications in the current model and the value of temperature that is obtained as a result. The temperature in the simulated spectrum is 1800 K.

Based on the results tabulated in Table 6.3, we estimate that the maximum error that arises from the limitations in the model is within 5 K when the temperature is 1800 K. The comparison of the second and the fourth case in Table 6.3 shows that the effect of uncertainty in the model can cause errors of opposite signs that can cancel one another. The effect of the modifications in the code on the value of temperature can be explained as follows.

Table 6.3: Temperature sensitivity to slight changes in the model

Modification in the model	T [K]
Replace the current values of polarizability derivatives with those obtained from CCSD(T) method and reported by Maroulis [58].	1802
Exclude the contribution from $^{14}N^{15}N$ from the current model	1807
Exclude anharmonic corrections (use vibrational matrix elements assuming harmonic oscillator).	1798
Same as 3 plus also exclude contributions from $^{14}N^{15}N$	1805

The temperature is most sensitive to the ratio of the intensity of the first hot band to the intensity of the fundamental band. Hence, the trends in the values of temperature obtained as a consequence of modifications in the model can be explained by examining their effect on the relative intensity of the first hot band and the fundamental band. In Table 4.2, two different sets of polarizability parameters are listed. We could have used either set in the final simulation. We chose to use the values of polarizability parameters given by Buldakov *et al.* [42] because they also give the expressions for Herman-Wallis factors and the vibrational part of the polarizalibity matrix elements as a function of v. If the values of polarizability parameters from Maroulis [58] are used in Buldakov's expressions the temperature is overestimated by 2 K. This is because the ratio of square of the vibrational part of polarizablity matrix element for $v = 1$ to that for $v = 0$ is 1.005

when Maroulis' polarizability parameters are used, and it is equal to 1.011 when Buldakov's values are used, and so a slightly lower value of temperature is calculated in the latter case to suppress the intensity of hot band from $v = 1$ in the simulation.

In case 2, when the contribution from $^{14}N^{15}N$ scattering is excluded from the model, the intensity of its Q branch which appears at ~606.1 nm, is not accounted for in the total intensity in that spectral region. In the least squares curve-fit the error is minimized by attributing a slightly higher intensity to the first hot band of $^{14}N_2$ which appears at ~606.5 nm. In consequence one infers a slightly higher temperature.

Case 3 examines the influence of neglecting the anharmonic corrections to the square of the polarizability matrix elements. From [42]

$$\frac{\left|R_{v=1}^{anh}\right|^2}{\left|R_{v=0}^{anh}\right|^2} = \left(\frac{(1.871+0.105v)_{v=1}}{(1.871+0.105v)_{v=0}}\right)^2 = 1.0113,$$

whereas for a harmonic oscillator

$$\frac{\left|R_{v=1}^{h}\right|^2}{\left|R_{v=0}^{h}\right|^2} = \frac{v_0}{v_1} = \frac{2329.914}{2301.238} = 1.0125.$$

Because the harmonic oscillator model slightly overestimates the contribution of the first (and higher) hot bands relative to the more accurate anharmonic model at any temperature, a fit to the model spectrum assuming a harmonic oscillator results in a slight underestimate of temperature from the fit. To the extent that the most complex model is equivalent to the experimental data, using more approximate models (no rare isotope, harmonic oscillator) introduces an error in fitted T of ± 5 K at 1800 K.

So, in the least noisy data $\Delta T \cong 9$ K as there is ±9 K because of uncertainty in line shape and the measurement is repeatable to ±2 K. Similarly, if we leave out the

contributions of the rare nitrogen isotope, anharmonic corrections in the vibrational matrix elements and use slightly different set of polarizability parameters then $\Delta T \cong 10$ K.

Chapter 7: Conclusion

The spontaneous Raman scattering signal is very weak. The signal from flames is even weaker because the gas density is low. It is desirable to increase the intensity of the laser incident on the flame, but this can lead to laser induced breakdown of the combustion gases. We have shown that it is possible to circumvent the problem of laser induced breakdown of flame gases by using a multiple-pass cell. The local incident excitation power density can be increased while preventing gas breakdown by focusing a low energy pulse laser repeatedly within a small region because the reflected pulses are only partially overlapped temporally.

Stable operation was first demonstrated in the ring mode with 100 passes. The drawback of the ring mode is that the spatial resolution is not high. The probe region is a cylindrical ring ~ 3.5 mm in diameter along the axis of the collection optics, with a length of 200 μm set by the width of the spectrometer slit. Later it was also shown that it is possible to achieve both the multiple passing and high spatial resolution by aligning the cell in the two point mode in which 25 passes are achieved at each point and each region is 300 μm × 200 μm.

The Raman instrument described here can be operated in the high dispersion mode or the low dispersion mode by changing gratings in the spectrograph. The primary goal of the low dispersion measurements was to demonstrate the operation of the multiple-pass Raman instrument for accurate temperature measurements. The objective of the high dispersion mode was to simplify the experiment by obviating the need to measure both Stokes and anti-Stokes signals and to improve the precision of the temperature measurement. It was shown that temperature can be measured reliably from both the low and high dispersion Raman spectra.

The Raman spectra were analyzed with a code that simulates the Raman spectrum. Improved theoretical models were added to the code to analyze the high resolution spectrum and reduce the uncertainty in the temperature measurement. The final version of the code includes angular dependence of Raman scattering, a more accurate instrument line shape function, scattering from the rare isotope of nitrogen present in the air, and vibration-rotation interaction and anharmonic effects on the Raman matrix elements. Because of the detailed theoretical model the noise in the signal and the uncertainty in the line shape parameters are now the biggest contributors to the uncertainty in temperature. As a result of very careful calibration and detailed simulation, the uncertainty in temperature measurement is ±9 K at flame temperatures because of uncertainty in the instrument line shape, and the measurement is repeatable to ±2 K.

The credibility of our results could further increase if we use the multiple-pass Raman instrument to measure the temperature of a NIST traceable source. For example, if we used our instrument and analysis tools to measure the temperature of pure nitrogen heated in a cell, and its temperature is known *a priori*, then we can calibrate our instrument against the standard source.

The multiple-pass Raman instrument that we have developed can either be directly applied or it can be modified and customized for other applications. The construction of a Raman cell, which is described in Appendix E, is a step in that direction. Some possible future directions that are interesting and potentially very useful are briefly discussed below. They can be categorized into instrument development, direct application, and technique development.

7.1 INSTRUMENT DEVELOPMENT – TOWARDS SINGLE SHOT MEASUREMENT

Single shot measurements are always desirable. It provides the best temporal resolution which is necessary to study fast processes in the sample. Here, I will briefly outline how the current multiple-pass Raman instrument can be modified for single shot measurements.

Consider Fig. 7.1, which shows the curve fit to the Stokes spectrum from N_2 in flame. The signal was acquired over 50 laser pulses in the ring mode. The *Q* branch of the fundamental and the first hot bands are adequately resolved to infer a temperature of 1880 K ±30 K. Suppose this is the type of data we aim to acquire from single shot of the laser, and the question is how the Raman instrument can be modified to achieve it.

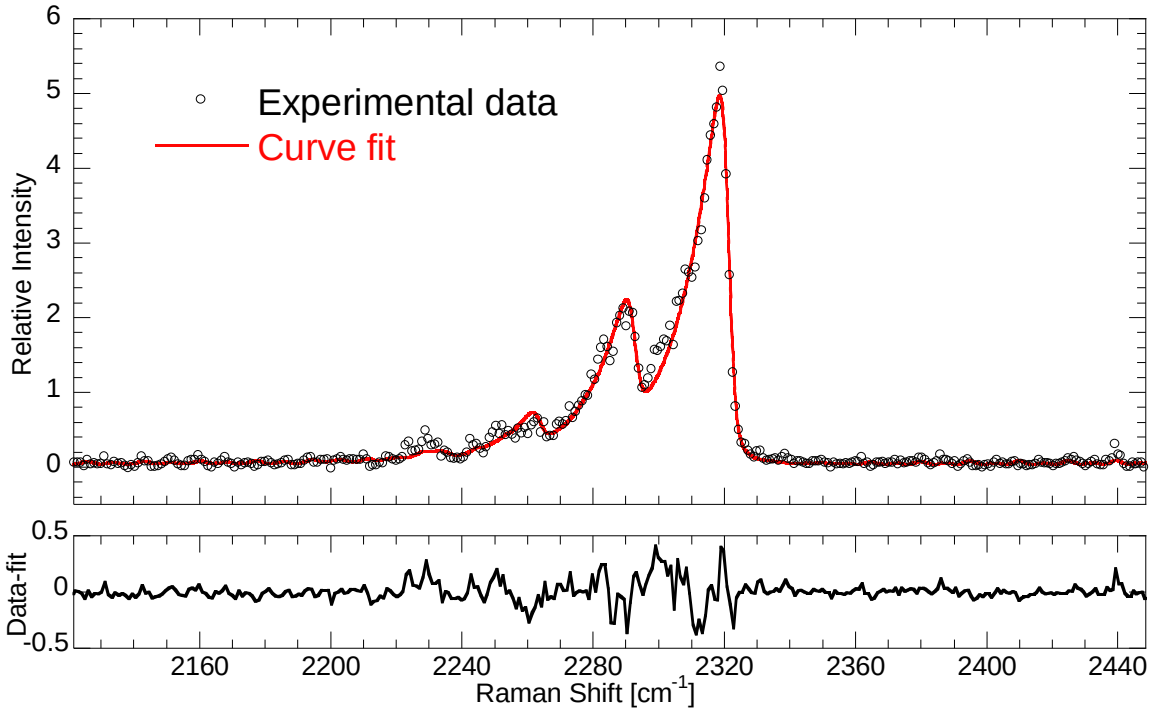

Figure 7.1: Stokes Raman spectrum of N_2 in flame from 50 laser pulses. The temperature inferred from the fit is 1880 K ± 30 K.

The f/# of the collection optics which acquired the data in Fig. 7.1 is 5.9. If the front lens in the collection optics is replaced with the Sigma 200-500 mm F2.8 APO EX DG ultra telephoto lens then the diameter of the collection lens will be 179 mm. The diameter of the collection lens at present is 38 mm. Everything else being equal, the collection f/# with the ultra telephoto lens will be 5.9/(179/38) = 1.25~1.3, which is a reasonable estimate. The f/# obtained by this scaling does not assume that the all the light gathered by the front lens is transmitted to the spectrometer as the f/5.9 of the current collection optics is measured by accounting for the possibility that some of the light that falls on the front lens will not be transmitted through the rest of the optics. In the best case scenario all the light entering the front lens is transmitted through it and the f/ # would be 0.8 when the object distance is 15 cm. This would lead to an increase in Q branch intensity by a factor of 41. According to Fig. B.5, when f/# is 1.3 the Q branch intensity will increase by 18.4 times which means that the spectrum in Fig. 7.1 can be generated with 3 pulses. Further improvement in the collection f/# can be attempted by moving the front lens closer to the sample. The current slit width is 100 μm, which can also be widened at the cost of spatial and spectral resolution for single shot measurements.

7.2 INSTRUMENT DEVELOPMENT – TWO DETECTION SYSTEMS

The capability of the multiple-pass Raman spectrometer can be greatly extended by setting up another detection system facing the current collection optics.

It will then be possible to acquire low and high resolution spectra simultaneously by mounting a low dispersion grating in one spectrograph and a high dispersion grating in another spectrograph, respectively. This will allow accurate temperature measurements

from the high dispersion spectrum and the low dispersion spectrum would also allow measurement of concentration of multiple species.

In general an additional detection system will extend the capability of the instrument to make simultaneous measurements of spectra which are separated far from one another. It will also be possible to record high dispersion Stokes and anti-Stokes spectra simultaneously by using Stokes and anti-Stokes gratings in the two spectrographs.

The two detection system will also enable simultaneous measurements of the perpendicular and parallel polarized Raman spectra. Each detection system can include a linear polarizer in a crossed orientation relative to the other. Since the unpolarized signal will be present in the spectra recorded by both the systems, it can be subtracted out and in this way, it will be possible to get rid of interferences from laser induced fluorescence signals which are often present in rich flames.

7.3 DIRECT APPLICATION – MEASUREMENT OF CH_4 ISOTOPES.

It is estimated that the US has enough shale gas reserves to last for 92 years at the rate of consumption in 2011 [66]. However, people in many states across the US are vehemently opposed to the extraction of shale gas as it can cause irreversible damage to the environment. Many people argue that fracturing the layers of rocks deep inside the earth (to release the shale gas) can cause earthquakes. They also believe that the fracture process can release toxic gases which can mix with the ground water.

The productivity of the shale gas reservoirs can be predicted from the ratio of ^{12}C to ^{13}C isotopes in CH_4 [67], which could be measured using the multiple-pass Raman instrument with a high dispersion grating. It can also be inferred from indirect Raman based techniques. For example, the methane can be burned to produce CO_2 and the ratio of ^{12}C to ^{13}C can be measured in CO_2. If the productivity of the shale gas reservoirs can

be reliably predicted then one can drill for the shale gas only in those regions where the potential economic benefits significantly outweigh the costs.

7.4 TECHNIQUE DEVELOPMENT – SURFACE ENHANCED RAMAN FLOW DIAGNOSTICS (SERFD)

The multiple-pass instrument can be an integral part of a new flow diagnostics technique. The flow can be seeded with gold nano particles (GNP) which are ~40 nm in diameter [68]. This is smaller than most of the dust particles so that in a practical environment the presence of GNP will not cause any more intrusion in the flow diagnostics than the dust particles [69]. The melting point of gold is 1337 K so flows up to ~1000 K can be safely seeded with GNP.

The Raman scattering from the molecules of the gas which adsorb on the GNP is enhanced by many orders of magnitude so that even single shot measurement can yield spectra with high SNR. The spatial resolution can be as good as the size of the GNP so that it could be limited by the optics and diffraction limits of the signal wavelength. The multiple-pass cell can be aligned in the line mode. The GNP can potentially generate surface enhanced Raman spectra of multiple species in the flow so that with a single laser shot it will be possible to simultaneously measure the temperature and concentration field of multiple species in the probe region using a relatively low energy laser pulse.

Raman spectroscopy is a versatile diagnostics technique so there can be many interesting applications of a Raman instrument. Most Raman instruments in the field are used for molecule identification for which a very high SNR is not necessary. We have shown that our Raman instrument is capable of very accurate temperature measurements. It can be operated in multiple alignment modes. It can also easily switch from low dispersion mode to high dispersion mode and vice versa. The instrument can now be applied to make precision temperature measurements in the study of combustion systems.

Appendix A: Thermocouple Radiation Correction

When the heat transferred to the thermocouple bead from the flame is in equilibrium with heat radiated to the room we have

$$A_c(T_g - T_b)h_c = \epsilon\sigma A_r(T_b^4 - T_r^4). \tag{A.1}$$

Here, T_b is the thermocouple bead temperature, T_g is the gas or flame temperature, T_r is the room temperature and h_c is the heat transfer coefficient of flame gases, and A_c and A_r are the effective surface areas for convective heat transfer and radiative heat transfer respectively. The expression for radiation temperature correction is

$$\Delta T_c = T_g - T_b = \frac{\epsilon\sigma(T_b^4 - T_r^4)A_r}{h_c A_c}. \tag{A.2}$$

The heat transfer coefficient is calculated as follows. From the definition of Nusselt number, Nu we get

$$\begin{aligned} h &= \frac{k\,Nu}{D} = \frac{k}{D}[0.42\mathrm{Pr}^{0.2} + 0.57\,\mathrm{Pr}^{0.33}Re^{0.5}] \\ &= \frac{k}{D}\left[0.42\left(\frac{\nu}{\alpha}\right)^{0.2} + 0.57\left(\frac{\nu}{\alpha}\right)^{0.33}\left(\frac{VD}{\nu}\right)^{0.5}\right]. \end{aligned} \tag{A.3}$$

Here, k is the thermal conductivity of the flame gases, Pr is the Prandtl number, Re is the Reynold's number, ν is the kinematic viscosity, α is the thermal diffusivity, V is the flow speed in the flame, and D is the thermocouple bead diameter.

At equilibrium, from eqns. A.2 and A.3 we have

$$T_g - T_b - \frac{\epsilon\sigma(T_b^4 - T_r^4)A_r}{A_c\frac{k}{D}\left[0.42\left(\frac{\nu}{\alpha}\right)^{0.2} + 0.57\left(\frac{\nu}{\alpha}\right)^{0.33}\left(\frac{VD}{\nu}\right)^{0.5}\right]} = 0. \tag{A.4}$$

The value of T_g that satisfies the above equation is the flame temperature, however this equation has to be solved iteratively or ν, α, k and V have to be explicitly expressed as functions of T_g and then the equation should be solved. The equation can be solved analytically or graphically.

The parameters ν, α, k are determined using the Gaseq program in the following way. The value of equivalence ratio ϕ is input to the program, and then a value for initial temperature is entered. The program then calculates the adiabatic flame temperature and the values of ν, α, k for the flame. This can be repeated for several input values of temperature and then a table of flame temperature vs. ν, α, k can be generated. The plot of these variables as a function of temperature can be curve fitted with a polynomial function to obtain $\nu\left(\frac{T_g+T_b}{2}\right), \alpha\left(\frac{T_g+T_b}{2}\right), k\left(\frac{T_g+T_b}{2}\right)$. Because of the presence of a thermal boundary layer the thermodynamic properties are calculated at a "film temperature" taken to be the average of the bead temperature and the flame temperature.

The flow speed V in eqn. (A.4) is determined as follows. We have

$$V = \frac{Q_{ref}}{A}\frac{(T_g + T_b)/2}{T_{ref}}. \tag{A.5}$$

Here, A is the area of the burner surface, T_{ref} is the room temperature and Q is the volume flow rate of the mixture of CH_4 and air.

$$Q = \frac{\dot{m}_{air} + \dot{m}_{CH_4}}{\bar{\rho}_{air+CH_4}(\phi, T_{ref})}. \tag{A.6}$$

The density of the mixture of air and CH_4 at a given equivalence ratio, ϕ and T can also be obtained from Gaseq.

The entire surface of the bead does not radiate to the room, some of it also radiates to the surface of the burner. Based on simulations in ZEMAX it was estimated that 36% of the bead surface radiates to the burner surface. The result of ZEMAX simulation is shown in Fig. A. 1. In this case $A_r/A_c = 0.64$, and eqn. (A.4) becomes

$$T_g - T_b - \frac{64}{100}\frac{\epsilon\sigma(T_b^4 - T_r^4)}{\frac{k}{D}\left[0.42\left(\frac{\nu}{\alpha}\right)^{0.2} + 0.57\left(\frac{\nu}{\alpha}\right)^{0.33}\left(\frac{VD}{\nu}\right)^{0.5}\right]} - \frac{36}{100}\frac{\epsilon\sigma(T_b^4 - T_{burner}^4)}{\frac{k}{D}\left[0.42\left(\frac{\nu}{\alpha}\right)^{0.2} + 0.57\left(\frac{\nu}{\alpha}\right)^{0.33}\left(\frac{VD}{\nu}\right)^{0.5}\right]} = 0 \tag{A.7}$$

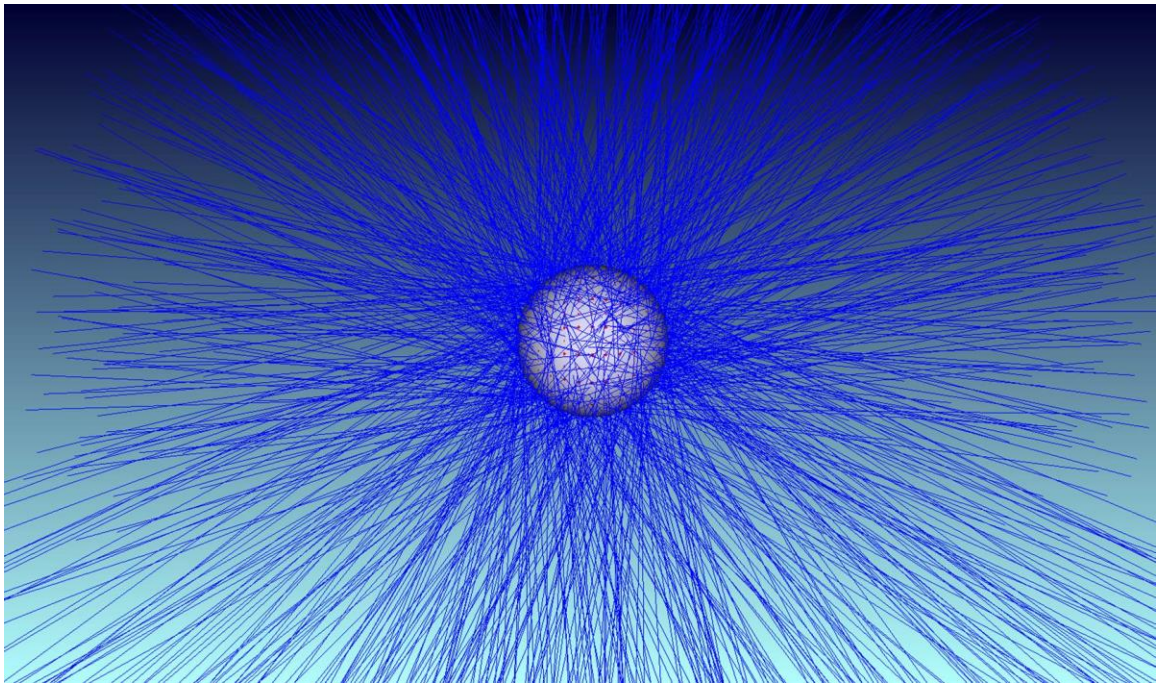

Figure A.1: Simulation of radiation from the bead. The figure contains 1000 rays, but the analysis was done with 1000000 rays.

Figure A.2 shows the set-up. The bead is 1.5 cm above the surface of the burner which is 6 cm in diameter. The grid used for calculations of irradiance on the burner surface is shown in Fig. A.3. Figure A.4 shows the radiation distribution on the surface of the burner as a result of the radiation from the bead. Out of 1000000 rays which are launched from the surface of the bead about 360,000 fall on the surface of the burner.

Figure A.2: The bead and the detector surface which represents the surface of the burner.

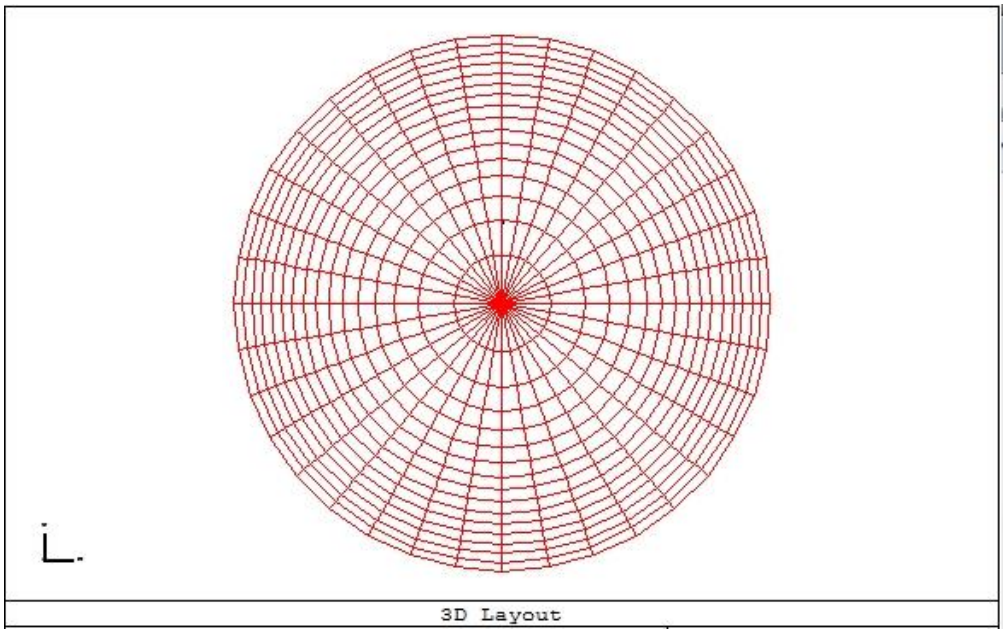

Figure A.3: The surface of the detector (burner) viewed from the top

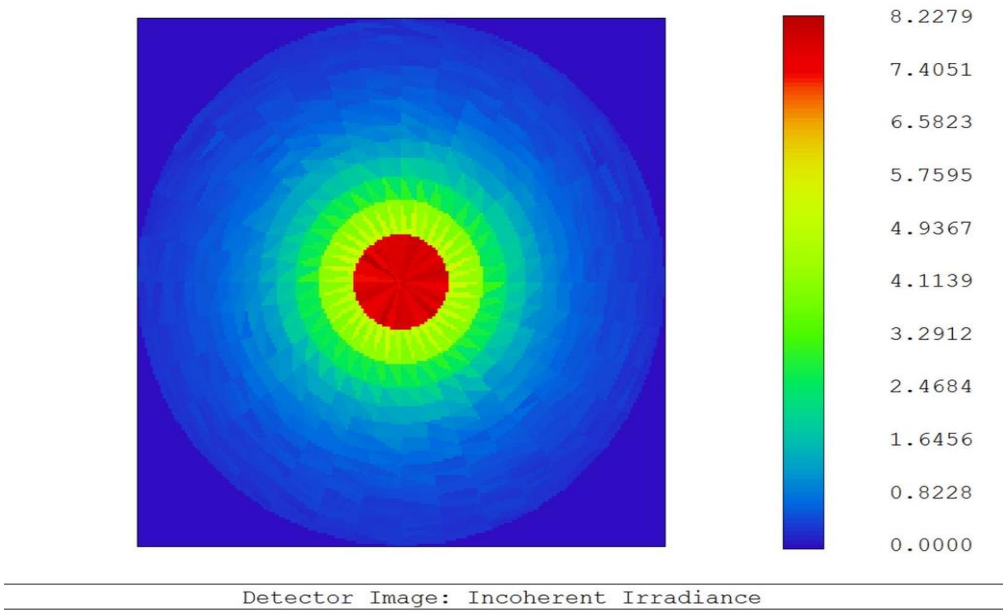

Figure A.4: Total power emitted by the bead is 100 W out of which 36 W falls on the surface of the burner

Appendix B: Angular Dependence of Raman Scattering

Consider the schematic of a scattering event shown below:

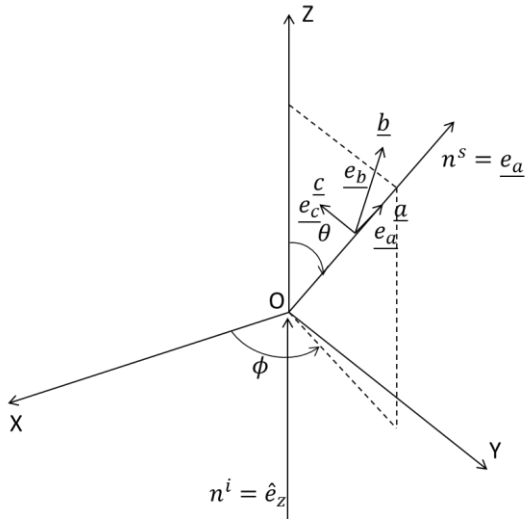

Figure B.1: Light scattering

The notations used in the figure are as follows. X, Y, Z are the axes of the space-fixed coordinate system, which means that their orientation is defined relative to one another. $\underline{a}, \underline{b}, \underline{c}$ are the axes of the system-fixed coordinate system, which means their orientation is defined by the incident and the scattered radiation. $\underline{e_a}$ is the unit vector in the direction of the scattered signal; $\underline{e_b}$ is perpendicular to the scattering plane, which is the plane containing the incident and the scattered radiation; $\underline{e_c}$ lies in the scattering plane.

Our goal is to express the power radiated into a given solid angle in terms of the polarizability derivatives and the Plackzek-Teller coefficients. In the subsequent statements, Φ is the average power from an oscillating dipole which is radiated into solid angle Ω, and $\left|\vec{P}\right|^2$ is the square of the magnitude of the induced dipole moment, ω is the angular frequency of oscillation of the induced dipole.

In the far field approximation, the electric field from an induced dipole oscillator is given by

$$\vec{E}(\theta, \phi, r) = \frac{\omega^2 \left|\vec{P}\right| \underline{e_b}}{4\pi\epsilon_0 c^2 r}. \tag{B.1}$$

The magnetic field is

$$\vec{H}(\theta,\phi,r) = \frac{\omega^2 \left|\vec{P}\right| \underline{e_c}}{4\pi c r}. \tag{B.2}$$

These expressions are available in any book on electromagnetism [24]. The vector representation of the direction of the propagation of the field is called the Poynting vector. Physically it is the flow of energy per unit time per unit area in the direction of the propagation of the wave. The Poynting vector is related to the electric and magnetic fields as follows:

$$\zeta = \vec{E} \times \overrightarrow{H}. \tag{B.3}$$

Now, we get

$$\zeta_{inst} = \frac{\omega^4 \left|\vec{P}\right|^2}{16\pi^2 \epsilon_0 c^3 r^2},$$

$$\overline{\zeta} = \frac{\omega^4 \langle \left|\vec{P}\right|^2 \rangle}{16\pi^2 \epsilon_0 c^3 r^2} = \frac{(2\pi c\tilde{\nu})^4 \langle \left|\vec{P}\right|^2 \rangle}{16\pi^2 \epsilon_0 c^3 r^2} = \frac{\pi^2 c \tilde{\nu}^4 \langle \left|\vec{P}\right|^2 \rangle}{\epsilon_0 r^2}.$$

Since, $\overline{\zeta}$ is the energy flux, we can define

$$d\overline{\Phi} \equiv d\Phi = \left|\overline{\zeta}\right| dA = \frac{\pi^2 c \tilde{\nu}^4 \langle \left|\vec{P}\right|^2 \rangle}{\epsilon_0 r^2} dA.$$

Using $\frac{dA}{r^2} = d\Omega$,

$$d\Phi = \frac{\pi^2 c \tilde{\nu}^4 \langle \left|\vec{P}\right|^2 \rangle}{\epsilon_0} d\Omega = \frac{\pi^2 c \tilde{\nu}^4 \langle \left|\vec{P}\right|^2 \rangle}{\epsilon_0} sin\theta d\theta d\phi.$$

Therefore,

$$\Phi = \frac{\pi^2 c \tilde{\nu}^4}{\epsilon_0} \int_{\phi_1}^{\phi_2} \int_{\theta_1}^{\theta_2} \langle \left|\vec{P}\right|^2 \rangle \, sin\theta' d\theta' d\phi'. \tag{B.3}$$

We are interested in calculating the components of the scattered signal that are polarized parallel and perpendicular to the scattering plane respectively. These components are in the system fixed coordinate system and then they can be converted to the space fixed coordinate system. So, now we want to find $\left|\vec{P}_{\parallel}\right|^2$ and $\left|\vec{P}_{\perp}\right|^2$ and then solve eqn. B.3.

Consider Fig. B.2, which is basically the same as Fig. B.1, but here only $\underline{e_c}$ is shown for clarity.

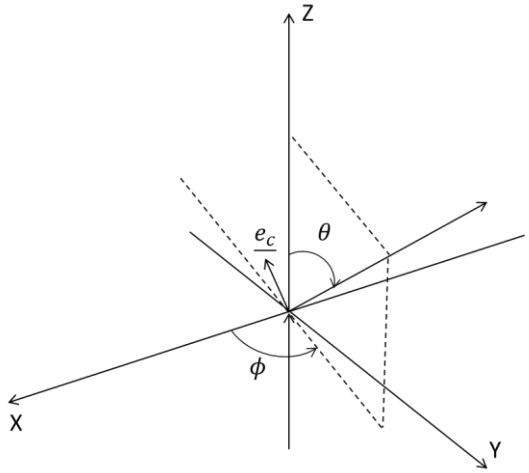

Figure B.2: Vector perpendicular to the direction of scattering in the scattering plane

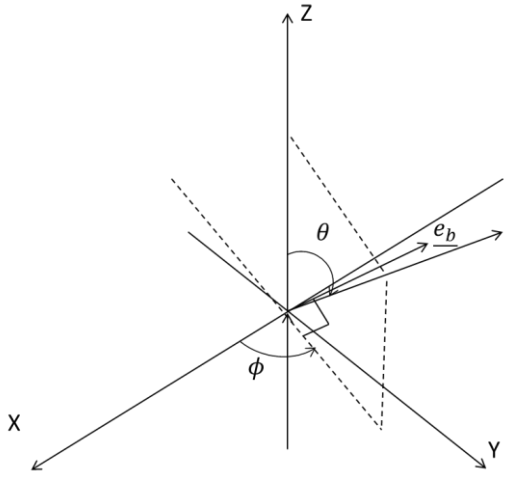

Figure B.3: Vector perpendicular to the direction of scattering and the scattering plane

From the diagram it can be inferred that

$$\begin{aligned}\underline{e_c} = &\left|\underline{e_c}\right| \hat{e}_z \sin\theta \\ &+ \left|\underline{e_c}\right| (-\hat{e}_y) \sin\left(\frac{\pi}{2} - \theta\right) \cos\left(\frac{\pi}{2} - \phi\right) \\ &+ \left|\underline{e_c}\right| (-\hat{e}_x) \sin\left(\frac{\pi}{2} - \theta\right) \sin\left(\frac{\pi}{2} - \phi\right),\end{aligned}$$

or

$$\underline{e_c} = -\hat{e}_x \cos\phi \cos\theta - \hat{e}_y \sin\phi \cos\theta + \hat{e}_z \sin\theta. \tag{B.4}$$

Now from eqn. B.4,

$$\begin{aligned}\left|\vec{P}_{\parallel}\right|^2 = \left|\vec{P}_c\right|^2 = &\left(-P_x \hat{e}_x \cos\phi \cos\theta - P_y \hat{e}_y \sin\phi \cos\theta + P_z\, \hat{e}_z \sin\theta\right) \\ &\cdot \left(-P_x \hat{e}_x \cos\phi \cos\theta - P_y \hat{e}_y \sin\phi \cos\theta + P_z\, \hat{e}_z \sin\theta\right).\end{aligned}$$

So

$$\left|\vec{P}_{\parallel}\right|^2 = P_x^2 \cos^2\phi \cos^2\theta + P_y^2 \sin^2\phi \cos^2\theta + P_z^2 \sin^2\theta \tag{B.5}$$

Similarly, for the component perpendicular to the scatter plane we can refer to Fig. B.3 and write

$$\underline{e_b} = -\hat{e}_x \left|\underline{e_b}\right| \cos\left(\frac{\pi}{2} - \phi\right) + \hat{e}_y \left|\underline{e_b}\right| \sin\left(\frac{\pi}{2} - \phi\right) = -\hat{e}_x \sin\phi + \hat{e}_y \cos\phi,$$

$$\left|\vec{P}_\perp\right|^2 = \left|\vec{P}_b\right|^2 = \left(-P_x \hat{e}_x \sin\phi + P_y \hat{e}_y \cos\phi\right) \cdot \left(-P_x \hat{e}_x \sin\phi + P_y \hat{e}_y \cos\phi\right).$$

So

$$\left|\vec{P}_\perp\right|^2 = P_x^2 \sin^2\phi + P_y^2 \cos^2\phi. \tag{B.6}$$

Now, we want to find P_x, P_y and P_z in eqns. B.5 and B.6. As mentioned in Chapter 1,

$$P_x = \alpha_{xx}E_x + \alpha_{xy}E_y + \alpha_{xz}E_z, \tag{B.7}$$

$$P_y = \alpha_{yx}E_x + \alpha_{yy}E_y + \alpha_{yz}E_z,$$

$$P_z = \alpha_{zx}E_x + \alpha_{zy}E_y + \alpha_{zz}E_z.$$

We have oriented the axes such that the excitation frequency is incident along $\hat{e}_z$ (hence, $E_z = 0$) and in practice we can set the laser polarization so that $E_x = 0$ and $E_y \neq 0$. This would be the intended case if the collection optics would be along the *X*-axis. Then we have

$$P_x = \alpha_{xy}E_y; \quad P_y = \alpha_{yy}E_y; \quad P_z = \alpha_{zy}E_y. \tag{B.8}$$

We can substitute for the components of the induced dipole using eqn. B.8 in B.5 and B.6. When we space average, i.e. average over all the possible orientations of the free molecule, and only consider the first derivative terms of the polarizability we can write

$$\overline{\left|\vec{P}_\parallel\right|^2} = \left[\overline{\left(\alpha'_{xy}\right)^2}\cos^2\phi\cos^2\theta + \overline{\left(\alpha'_{yy}\right)^2}\sin^2\phi\cos^2\theta + \overline{\left(\alpha'_{zy}\right)^2}\sin^2\theta\right]E_y^2, \tag{B.9}$$

$$\overline{\left|\vec{P}_\perp\right|^2} = \left[\overline{\left(\alpha'_{xy}\right)^2}\sin^2\phi + \overline{\left(\alpha'_{yy}\right)^2}\cos^2\phi\right]E_y^2. \tag{B.10}$$

We can express the matrix elements given in eqns. B.9 and B.10 in terms of the isotropic and anisotropic polarizability derivatives by referring to Table I from Long [24]. Their form depends on the energy states and the selection rules.

In the above expressions, I have dropped the terms that are not angle dependent. The exact form of these terms is obtained by operating on the vibrational-rotational wave functions with the polarizability operator and taking the inner product. This procedure is within the domain of computational spectroscopy and requires expertise in quantum chemistry. Here, our goal is only to obtain the angular dependent components of the expression for Raman scattering, and so all the details of the angle independent terms are not necessary, and are represented by a scaling factor K in the expressions below.

Since $\overline{|\vec{P}|^2} = \overline{|\vec{P}_\parallel|^2} + \overline{|\vec{P}_\perp|^2}$, for the O, Q and S branches we have

$$\overline{|\vec{P}|_Q^2} = \left[(a')^2 + \frac{7(\gamma')^2}{45} b_{JJ} - \left((a')^2 + \frac{(\gamma')^2}{45} b_{JJ}\right) \sin^2\theta \sin^2\phi\right] K, \tag{B.11}$$

$$\overline{|\vec{P}|_{S,O}^2} = \left[\frac{7(\gamma')^2}{45} b_{J\pm2,J} - \frac{(\gamma')^2}{45} b_{J\pm2,J} \sin^2\theta \sin^2\phi\right] K. \tag{B.12}$$

From eqns. B.11, B.12, B.3 with $\theta_1 = \theta, \theta_2 = \pi - \theta, \phi_1 = -\phi, \phi_2 = \phi$ we get

$$\begin{aligned}\Phi_Q = {} & K\left[(a')^2 + \frac{7(\gamma')^2}{45} b_{JJ}\right] 4\phi\cos\theta \\ & + K\left[(a')^2 + \frac{(\gamma')^2}{45} b_{JJ}\right] \frac{1}{12} (9\cos\theta - \cos 3\theta)(\sin 2\phi - 2\phi),\end{aligned} \tag{B.13}$$

$$\begin{aligned}\Phi_{S,O} = {} & K\left[\frac{7(\gamma')^2}{45} b_{J\pm2,J}\right] 4\phi\cos\theta \\ & + K\left[\frac{(\gamma')^2}{45} b_{J\pm2,J}\right] \frac{1}{12} (9\cos\theta - \cos 3\theta)(\sin 2\phi - 2\phi).\end{aligned} \tag{B.14}$$

If the collection optics is along the X-axis and the incident light is along the Z-axis, it is not generally desirable to set the laser polarization such that $E_y = 0$ and $E_x \neq 0$. However, let us imagine that it is the case and then the angle dependent parts for the expression for Raman scattering is found as follows. This is useful when one is trying to

suppress the Q branch signal because when the collection solid angle is vanishingly small and the polarization of the excitation wavelength is parallel to the scattering plane the scattered Raman signal only depends on the anisotropic derivatives. The comparison of this data with the Raman signal generated when the polarization of the excitation wavelength is perpendicular to the scattering plane can help to estimate the values of the polarizability derivatives. Equation B.8 now becomes

$$P_x = \alpha_{xx}E_x; \quad P_y = \alpha_{yx}E_x; \quad P_z = \alpha_{zx}E_x. \tag{B.15}$$

Instead of eqns. B.9 and B.10 we have

$$\overline{\left|\vec{P}_{\parallel}\right|^2} = \left[\overline{(\alpha'_{xx})^2}\cos^2\phi\cos^2\theta + \overline{\left(\alpha'_{yx}\right)^2}\sin^2\phi\cos^2\theta + \overline{(\alpha'_{zx})^2}\sin^2\theta\right]E_x^2, \tag{B.16}$$

$$\overline{\left|\vec{P}_{\perp}\right|^2} = \left[\overline{(\alpha'_{xx})^2}\sin^2\phi + \overline{\left(\alpha'_{yx}\right)^2}\cos^2\phi\right]E_x^2. \tag{B.17}$$

Then we get

$$\overline{\left|\vec{P}\right|_Q^2} = \left[(a')^2 + \frac{7(\gamma')^2}{45}b_{JJ} - \left((a')^2 + \frac{(\gamma')^2}{45}b_{JJ}\right)\sin^2\theta\cos^2\phi\right]K, \tag{B.18}$$

$$\overline{\left|\vec{P}\right|_{S,O}^2} = \left[\frac{7(\gamma')^2}{45}b_{J\pm2,J} - \frac{(\gamma')^2}{45}b_{J\pm2,J}\sin^2\theta\cos^2\phi\right]K. \tag{B.19}$$

So,

$$\begin{aligned}\Phi_Q = {} & K\left[(a')^2 + \frac{7(\gamma')^2}{45}b_{JJ}\right]4\phi\cos\theta \\ & -K\left[(a')^2 + \frac{(\gamma')^2}{45}b_{JJ}\right]\frac{1}{12}(9\cos\theta - \cos 3\theta)(\sin 2\phi + 2\phi),\end{aligned} \tag{B.20}$$

$$\Phi_{S,O} = K\left[\frac{7(\gamma')^2}{45} b_{J\pm2,J}\right] 4\phi\cos\theta \qquad \text{(B.21)}$$
$$-K\left[\frac{(\gamma')^2}{45} b_{J\pm2,J}\right]\frac{1}{12}\,(9\cos\theta - \cos 3\theta)(\sin 2\phi + 2\phi).$$

So far the angular dependence of Raman scattering was derived assuming that the excitation radiation is incident along the *Z*-axis. When there are multiple beams, as in a multiple-pass cell, it is necessary to know the angular distribution of the signal when the excitation beam is at an angle to the *Z*-axis. This expression will be more relevant for the two point mode. The method of derivation is the same as shown above so only the important results will be stated below.

Assume that the axis of the cell is along the *Z*-axis. The laser beam is incident at the origin. As shown in Fig. B.4, it makes angle β with the Z-axis, and it is in the *XZ* plane. Now, assume that the collection optics is along the *Y*-axis. In this case the scattering towards the collection optics is maximized if $E_y = 0$, and $E_x = E_0\cos\beta$ and $E_z = E_0\sin\beta$. Then

$$\overline{\left|\vec{P}_\perp\right|^2} = \left[\overline{(\alpha'_{xx})^2}\sin^2\phi\cos^2\beta + \overline{(\alpha'_{xz})^2}\sin^2\phi\sin^2\beta + \overline{\left(\alpha'_{yx}\right)^2}\cos^2\phi\right]E_0^2, \qquad \text{(B.22)}$$

$$\overline{\left|\vec{P}_\parallel\right|^2} = \left[\begin{array}{c}\overline{(\alpha'_{xx})^2}\cos^2\phi\cos^2\theta\cos^2\beta + \overline{(\alpha'_{xz})^2}\cos^2\phi\cos^2\theta\sin^2\beta \\ +\overline{\left(\alpha'_{yx}\right)^2}\sin^2\phi\cos^2\theta + \overline{(\alpha'_{zz})^2}\sin^2\theta\sin^2\beta + \overline{(\alpha'_{zx})^2}\sin^2\theta\cos^2\beta\end{array}\right]E_0^2, \qquad \text{(B.23)}$$

$$\overline{\left|\vec{P}\right|_Q^2} = \left[\begin{array}{c}\left((a')^2 + \frac{(\gamma')^2}{45}b_{JJ}\right)(\cos^2\beta - \cos^2\beta\sin^2\theta\cos^2\phi + \sin^2\beta\sin^2\theta) \\ +\frac{2(\gamma')^2}{15}b_{JJ}\end{array}\right], \qquad \text{(B.24)}$$

$$\overline{\left|\vec{P}\right|_{S,O}^{2}} = \left[\left(\frac{(\gamma')^2}{45} b_{J\pm2,J}\right)(\cos^2\beta - \cos^2\beta \sin^2\theta \cos^2\phi + \sin^2\beta \sin^2\theta) + \frac{2(\gamma')^2}{15} b_{J\pm2,J}\right]. \quad \text{(B.25)}$$

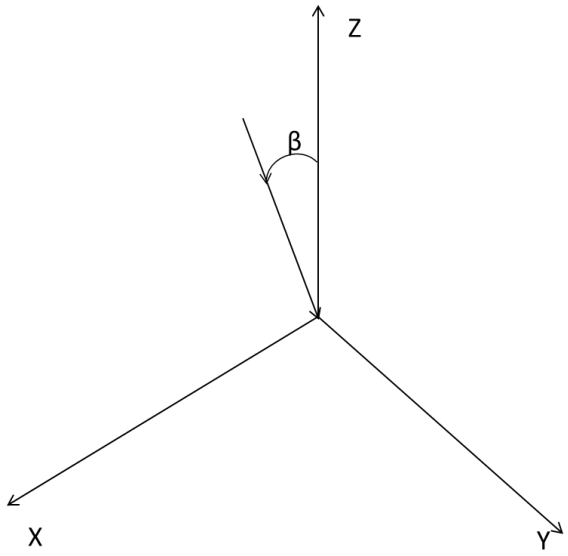

Figure B.4: Incident light is in the XZ plane and it makes an angle β with the Z axis

The limits of integral when we use eqn. B.3 depend on the location of the collection optics. In the earlier case we assumed that the collection optics was axis symmetric about the *X*-axis and so $-\phi \le \phi' \le \phi$ and $\theta \le \theta' \le \pi - \theta$. Now, we assume that the collection optics is axis symmetric about the *Y*-axis and so $\phi \le \phi' \le \pi - \phi$ and $\theta \le \theta' \le \pi - \theta$. The reason we now assume that the collection optics is along *Y*-axis instead of *X*-axis is that it is consistent with the way the optics is aligned in the lab with respect to the path of the laser beam in the two point mode in the real experiment. The results are as follows.

$$\begin{aligned}\Phi_Q = \Bigg\{\left[(a')^2 + \frac{(\gamma')^2}{45} b_{JJ}\right]\Big[&2(\pi - 2\phi)\cos\theta\cos^2\beta \\ &+ \frac{1}{12}(2\phi + \sin 2\phi - \pi)(9\cos\theta - \cos 3\theta)\cos^2\beta \\ &+ \frac{1}{6}(\pi - 2\phi)(9\cos\theta - \cos 3\theta)\sin^2\beta\Big] \\ &+ \frac{2(\gamma')^2}{15} b_{JJ} 2(\pi - 2\phi)\cos\theta\Bigg\} K\end{aligned} \quad \text{(B.26)}$$

$$\Phi_{S,O} = \left\{\left[\frac{(\gamma')^2}{45} b_{J\pm2,J}\right]\left[2(\pi - 2\phi)\cos\theta\cos^2\beta\right.\right. \tag{B.27}$$
$$+ \frac{1}{12}(2\phi + \sin 2\phi - \pi)(9\cos\theta - \cos 3\theta)\cos^2\beta$$
$$\left.+ \frac{1}{6}(\pi - 2\phi)(9\cos\theta - \cos 3\theta)\sin^2\beta\right]$$
$$\left. + \frac{2(\gamma')^2}{15} b_{J\pm2,J} 2(\pi - 2\phi)\cos\theta\right\} K$$

The angles θ and ϕ are related to f/# of the collection optics as follows. When deriving the angle dependence with the laser beam oriented along the *Z*-axis and collection optics along the *X*-axis we have

$\phi = \arctan\left(\frac{1}{2f\#}\right)$,

$\theta = \frac{\pi}{2} - \arctan\left(\frac{1}{2f\#}\right)$.

When the collection optics is along the *Y*-axis,

$\phi = \theta = \frac{\pi}{2} - \arctan\left(\frac{1}{2f\#}\right)$.

The method outlined here can be used to find the angle dependent scattering for any location of the collection optics. The following conclusions are derived from the equations above.

When the f/# changes, all the *S* branch and *O* branch intensities scale by a constant factor. All the *Q* branch intensities also scale by a constant factor, but the *Q* branch scaling factor is slightly less than the *O* or *S* branch scaling factor. This implies that the inclusion of angle dependence factors does not affect the value of temperature as the temperature is determined either by comparing the relative intensity of *Q* branch transitions, *O* branch transitions or *S* branch transitions. However, when fitting the *Q* branch simultaneously with the *O* and *S* branches, there is a slight inconsistency that might be attributed to an uncertainty in the relative values of polarizability derivatives. This also implies that the values of "effective polarizability derivatives" are affected by the angular dependence of Raman scattering if the angular dependence is not included in

the model; as shown in Fig. B.5, when the f/# decreases the *S* or *O* branch transition intensities increase faster than those in the *Q* branch. Figure B.5 is obtained from eqns. B.13 and B.14 by summing over contributions from *J*=0 to 100. The *Q* branch intensity at a given f/# is normalized to the *Q* branch intensity at f/5.9, the current f/# of our collection optics.

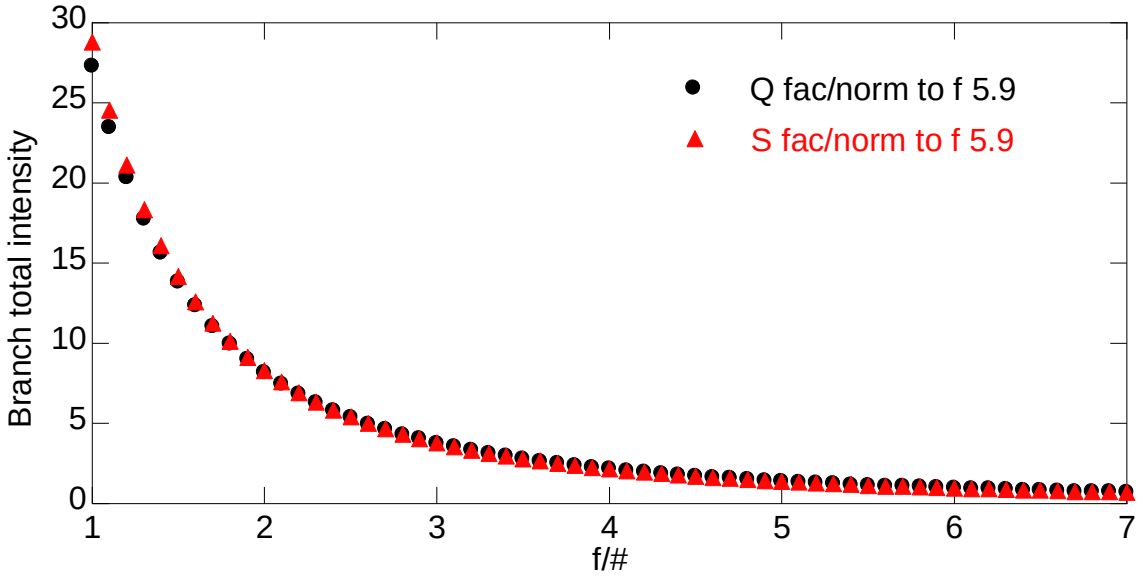

Figure B.5: Change in total intensity (sum of transitions from *J*=0 to 100) of *Q* and *S* branch normalized to the total intensity f/# is 5.9

Figure B.6 shows the ratio of the *S* and *Q* branch intensities given in fig. B.5. It further emphasizes that as the f/# decreases the angular effect should be included in the model; otherwise in the comparison between the simulation and the experimental results it would appear as if the ratio of the isotropic to anisotropic polarizability derivatives is incorrect.

Raman spectroscopy has traditionally been used for the identification of complex polyatomic molecules. High precision, high resolution Raman spectra on small molecules have usually been collected at large f/#, so the *S* or *O* vs. *Q* discrepancy displayed in Fig.

B.6 is unlikely to have affected them. However, modern spectrographs with holographic gratings and array detectors, Raman microscopy systems, and Fourier Transform-Raman techniques can operate at sufficiently high collection solid angle that the corrections shown in Fig. B.6 would need to be incorporated in accurate measurements.

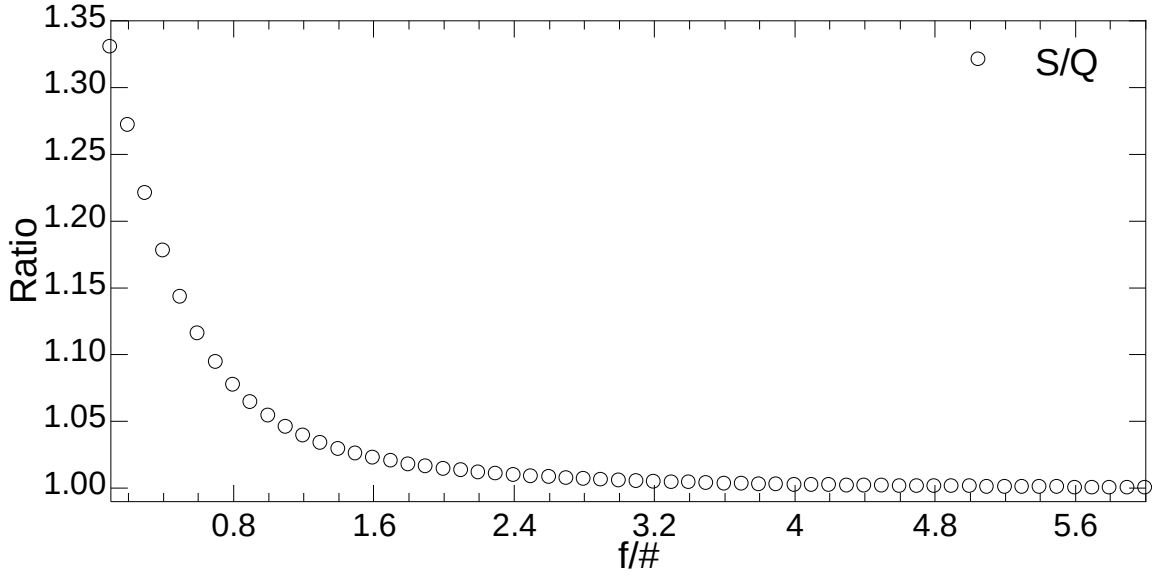

Figure B.6: Ratio of the S and Q branch factors in Fig. B.5. Significant errors in modeling will occur if angular dependence is not included if the data is collected with low f/# or large collection solid angle.

Now, we calculate the difference in the angular effect when the laser beam is incident on the origin O at an angle β to the Z-axis. It is assumed that 25 beams are incident on O and they are separated at 1° interval from -12° to 12°. The basis for the assumption is as follows. The mirrors are separated by ~400 cm. The diameter of each mirror is 101.6 mm and the length of the slot through which the beam enters is about 9.5 mm. This means the beams focused at a point at the center of the cell are spread over ~26°. Assuming there are 25 passes spread over 25° the beams would be spread over -12° to 12° at interval of 1°. A simple MATLAB code can sum over all β and J's in eqns. B.26

and B.27. The ratio of the total intensity of the Q branches and S branches for 25 passes and single pass as a function of f/# is shown in Fig. B.7. One can infer that at the f/# (5.9) of our collection optics the contribution to the Raman intensity from 25 passes is ~25 times the contribution from single pass, and so in the current Raman code we do not sum over the Raman signal produced by all the beams; we only calculate the scattering caused by one beam. It is important to take the angle of incidence into consideration at very low f/#s.

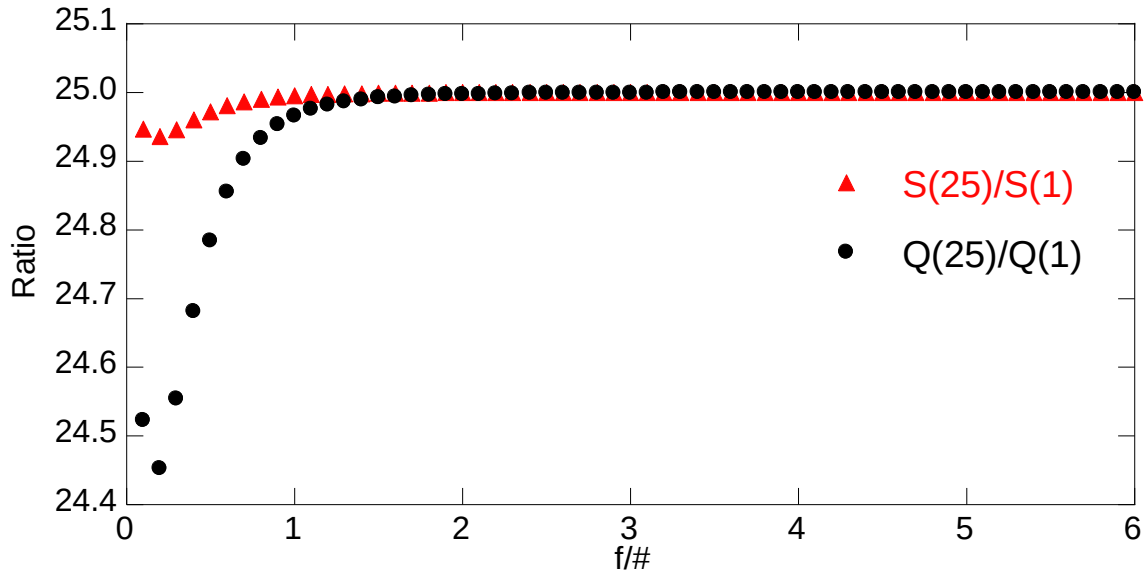

Figure B.7: Ratio of S and Q branch intensity from 25 passes distributed over 25 degrees to the intensity of S and Q branch of single pass at 0 degrees to the Z axis

The magnitude of the angular effect is molecule specific as shown below. From eqn. B.13

$$\frac{\Phi_Q\left(\frac{f}{\#}\right)}{\Phi_Q\left(\frac{f}{\#}\to\infty\right)} \approx \frac{\left((a')^2+\frac{7(\gamma')^2}{45}b_{JJ}\right) + \frac{1}{4\phi\cos\theta}\left((a')^2+\frac{(\gamma')^2}{45}b_{JJ}\right) \times \frac{1}{12}\,(9\cos\theta-\cos 3\theta)(\sin 2\phi-2\phi)}{\left((a')^2+\frac{7(\gamma')^2}{45}b_{JJ}\right)}. \tag{B.28}$$

From eqn. B.14

$$\frac{\Phi_{S,O}\left(\frac{f}{\#}\right)}{\Phi_{S,O}\left(\frac{f}{\#}\to\infty\right)} \approx \frac{\times\frac{1}{12}\,(9\cos\theta-\cos 3\theta)(\sin 2\phi-2\phi)}{\left(\frac{7(\gamma')^2}{45}b_{J\pm,J}\right)}. \tag{B.29}$$
$$\left(\frac{7(\gamma')^2}{45}b_{J\pm2,J}\right)$$
$$+\frac{1}{4\phi\cos\theta}\left(\frac{(\gamma')^2}{45}b_{J\pm2,J}\right)$$

Equation B.28 can be written as

$$\frac{\Phi_Q\left(\frac{f}{\#}\right)}{\Phi_Q\left(\frac{f}{\#}\to\infty\right)} \approx 1+\frac{1}{4\phi\cos\theta}\frac{\left((a')^2+\frac{(\gamma')^2}{45}b_{JJ}\right)}{\left((a')^2+\frac{7(\gamma')^2}{45}b_{JJ}\right)}\frac{1}{12}\,(9\cos\theta-\cos 3\theta)(\sin 2\phi-2\phi), \tag{B.30}$$

while equation B.29 can be written as

$$\frac{\Phi_{S,O}\left(\frac{f}{\#}\right)}{\Phi_{S,O}\left(\frac{f}{\#}\to\infty\right)} \approx 1+\frac{1}{4\phi\cos\theta}\frac{1}{7}\,\frac{1}{12}\,(9\cos\theta-\cos 3\theta)(\sin 2\phi-2\phi). \tag{B.31}$$

Now,

$$\frac{\left((a')^2+\frac{(\gamma')^2}{45}b_{JJ}\right)}{\left((a')^2+\frac{7(\gamma')^2}{45}b_{JJ}\right)} = \frac{(a')^2+\frac{4(\gamma')^2}{45}b_{JJ}-\frac{(\gamma')^2}{15}b_{JJ}}{\left((a')^2+\frac{7(\gamma')^2}{45}b_{JJ}\right)} = \frac{I_\perp^\perp\left(\frac{\pi}{2}\right)-I_\parallel^\perp\left(\frac{\pi}{2}\right)}{I_\perp^\perp\left(\frac{\pi}{2}\right)+I_\parallel^\perp\left(\frac{\pi}{2}\right)} = \frac{1-\rho_\perp}{1+\rho_\perp}.$$

Hence, the amount of enhancement (or suppression) of *Q* branch relative to the *S* or *O* branch is a function of the *Q* branch depolarization ratio which is molecule specific:

$$\frac{\frac{\Phi_Q\left(\frac{f}{\#}\right)}{\Phi_Q\left(\frac{f}{\#}\to\infty\right)}}{\frac{\Phi_{S,O}\left(\frac{f}{\#}\right)}{\Phi_{S,O}\left(\frac{f}{\#}\to\infty\right)}} \approx \frac{\left[1+\frac{1}{4\phi\cos\theta}\left(\frac{1-\rho_\perp}{1+\rho_\perp}\right)\frac{1}{12}\,(9\cos\theta-\cos 3\theta)(\sin 2\phi-2\phi)\right]}{\left[1+\frac{1}{4\phi\cos\theta}\frac{1}{7}\,\frac{1}{12}\,(9\cos\theta-\cos 3\theta)(\sin 2\phi-2\phi)\right]},$$

or

$$\frac{\dfrac{\Phi_Q\left(\frac{f}{\#}\right)}{\Phi_Q\left(\frac{f}{\#}\to\infty\right)}}{\dfrac{\Phi_{S,O}\left(\frac{f}{\#}\right)}{\Phi_{S,O}\left(\frac{f}{\#}\to\infty\right)}} \approx \frac{\left[1+\frac{1}{4\phi\cos\theta}\left\{\left(\frac{1-\rho_\perp}{1+\rho_\perp}\right)_Q\right\}\frac{1}{12}\,(9\cos\theta-\cos 3\theta)(\sin 2\phi-2\phi)\right]}{\left[1+\frac{1}{4\phi\cos\theta}\left\{\left(\frac{1-\rho_\perp}{1+\rho_\perp}\right)_{S,O}\right\}\frac{1}{12}\,(9\cos\theta-\cos 3\theta)(\sin 2\phi-2\phi)\right]},$$

where, as mentioned earlier, $\phi = \arctan\left(\frac{1}{2f\#}\right)$ and $\theta = \frac{\pi}{2} - \arctan\left(\frac{1}{2f\#}\right)$.

Appendix C: Simulation of Raman Scattering from H_2

The purpose of this appendix is to show that the code for Raman scattering from N_2 can be easily modified by changing the values of molecular parameters to simulate Raman spectra of other diatomic molecules like O_2, H_2, Cl_2, etc. Simulated spectra of H_2 are shown at 300 K and 1800 K in Figs. C.1 and C.2, respectively. The line shape is the same as in the lab experiments. The most detailed version of the theory is used. In Fig. C.2, all the lines are not labeled so that the figure is legible. The notation is $B_v(J)$, where B is the name of the branch to which the transition belongs, v is the vibrational level of the initial state, and J is the rotational level of the initial state. The values of vibrational and rotational constants can be obtained from NIST [70]. The values of Dunham potential coefficients are taken from the same source as Tipping and Ogilvie [55, 71]. The calculation of the polarizability derivatives is described here.

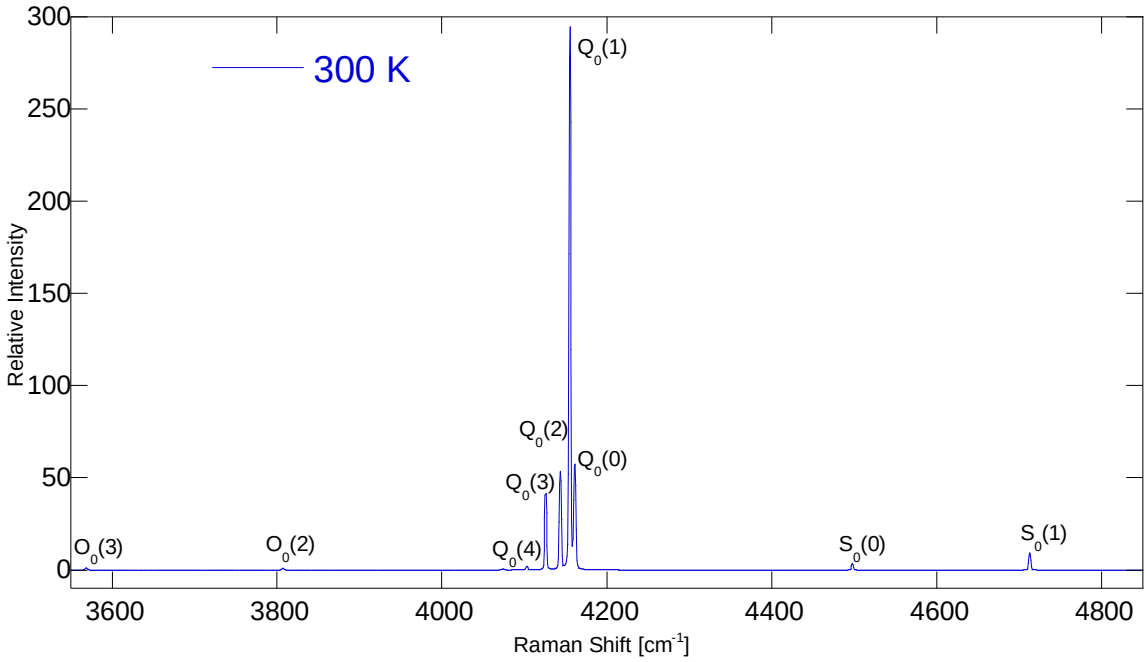

Figure C.1: Predicted Stokes Raman spectrum of H_2 at 300 K using our detection optics

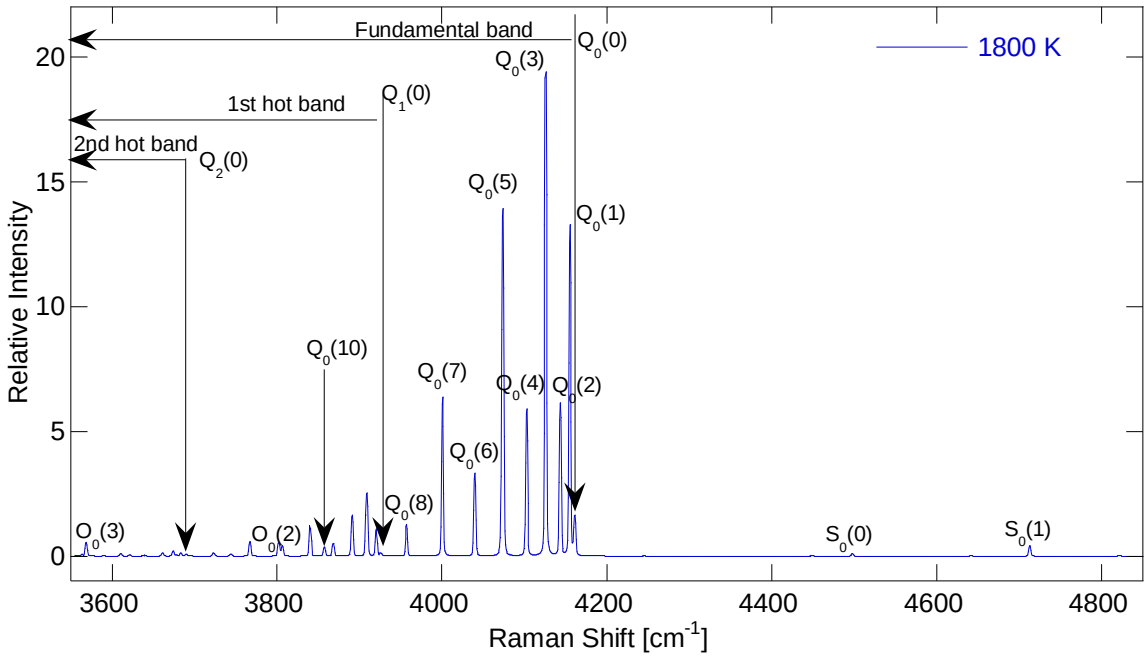

Figure C.2: Predicted Stokes Raman spectrum of H_2 at 1800 K using our detection optics

The polarizability derivatives of H_2 are determined using the numerical results provided by Kolos and Wolniewicz [72]. Simulation of Raman scattering requires the values of polarizability derivatives about the equilibrium position. We assume that the polarizability can be expanded in a series about its equilibrium value [55].

$$p(x) = \sum_{j=0} p_j x^j \tag{C.1}$$

Here $x = (R - R_e)/R_e$. One could curve fit only the region of data that is near x=0. However, it is not clear over what range of x the series expansion should be determined. The coefficients of the expansion also depend on the plot points included in the fit and the order of the polynomial. Therefore, there is high uncertainty in the values

of high order polarizability derivatives obtained here. Tipping and Ogilvie list $\gamma_0, \gamma_1, \gamma_2$ and γ_3, however, they also obtained it by performing a least-squares fit on the anisotropic polarizability function provided by Cheung *et al*. [73]. The values they obtained are given in Table C.1

Table C.1: Coefficients of anisotropic polarizability (in $Å^3$) computed by Tipping and Ogilvie

Anisotropic polarizability coefficients	
γ_0	1.91633
γ_1	4.93862
γ_2	3.29358
γ_3	2.21407

The values of γ_0, γ_1 and γ_2 obtained here are close to the values obtained by Tipping and Ogilvie; however there is large discrepancy between the values of γ_3 obtained here and by Tipping and Ogilvie. So, in addition to theory used to calculate the polarizability at various inter nuclear separations, as mentioned earlier, the freedom in the way the curve fit is performed on polarizability vs. inter nuclear separation also leads to uncertainty in the value of polarizability derivatives. Here, Raman scattering from hydrogen molecule will be simulated using the values of polarizability derivatives obtained from the curve fit as shown in Fig. C.3.

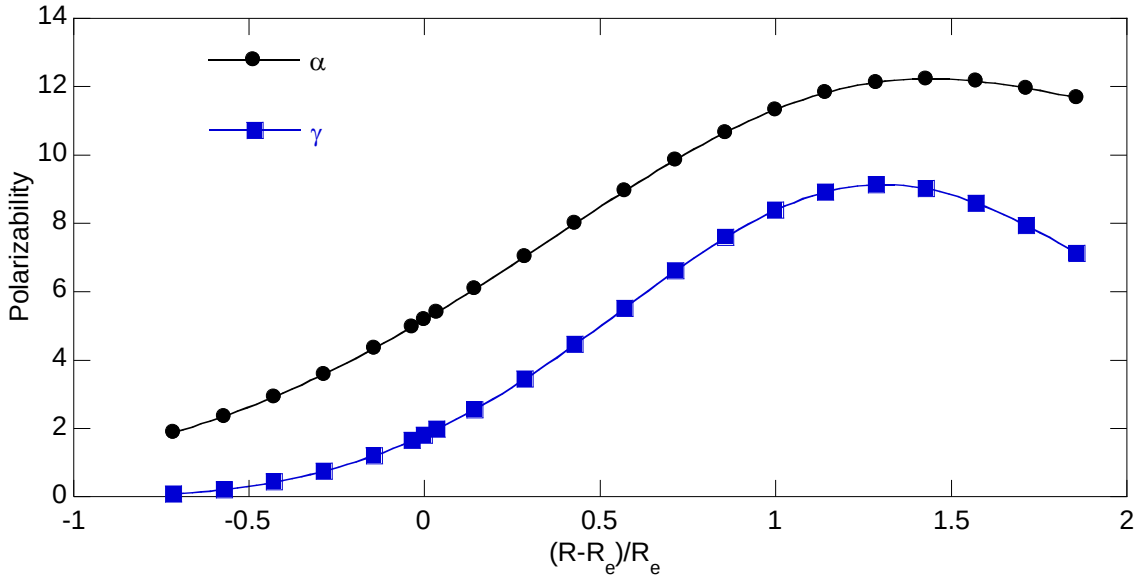

Figure C.3: Determination of the polarizability derivatives (in $Å^3$) of H_2

Equation C.1 with $j = 9$ is used as the polynomial function. The coefficients of the polynomial are listed in Table C.2.

Table C.2 Coefficients of the polynomial used to curve fit polarizability as a function of reduced displacement

Isotropic polarizability coefficients		Anisotropic polarizability coefficients	
α_0	5.1787	γ_0	1.8029
α_1	6.0853	γ_1	4.7186
α_2	1.6255	γ_2	3.6862
α_3	-0.86098	γ_3	0.090705
α_4	-0.54166	γ_4	-1.2791
α_5	-0.33856	γ_5	-1.056
α_6	0.02714	γ_6	2.9591×10^{-5}
α_7	0.21571	γ_7	0.57586
α_8	-0.056492	γ_8	-0.15378
α_9	-0.0020344	γ_9	-0.001183

Alternatively, polarizability can be expressed as Taylor series [24, 42] such that the coefficients of the expansion in eqn. C.1 are related to the coefficient of the Taylor expansion as

$$p_n = \frac{\partial^n p}{\partial x^n}\frac{1}{n!} \tag{C.2}$$

The Raman code requires the input of polarizability derivatives so $\partial^n p/\partial x^n$ are computed from Table C.2 and eqn. C.2, and their values are listed in Table C.3.

Table C.3: Isotropic and anisotropic polarizability derivatives (in $Å^3$) obtained from curve fit to polarizability vs. non-dimensionalized internuclear separation

Isotropic polarizability derivative		Anisotropic polarizability derivative	
α	5.18	γ	1.80
α'	6.09	γ'	4.72
α''	3.25	γ''	7.37
α'''	-5.17	γ'''	0.54

Appendix D: A Note on Polarizability Derivatives

In the literature the polarizability derivatives are defined as $\frac{\partial^n P}{\partial r^n}$ or $\frac{\partial^n P}{\partial r^n} r^n$. When the definition is $\frac{\partial^n P}{\partial r^n}$ the units are in atomic units and when the definition is $\frac{\partial^n P}{\partial r^n} r^n$ the units are in Å^3. Lack of this awareness can cause confusion particularly when the units and thus, values of the polarizability derivatives, are interchanged between a paper and its citing article.

The following table lists some of the references which have defined the polarizability derivatives in one of the afore mentioned ways.

Table D.1: Definitions of polarizability derivatives in various sources

Polarizability derivative	Reference
$(\partial^n P/\partial r^n)\ r^n$	Tipping and Ogilvie [55]
$\partial^n P/\partial r^n$	Langhoff *et al.* [64]
$(\partial^n P/\partial r^n)\ r^n$	Knippers *et al.* [57]
$(\partial^n P/\partial r^n)\ r^n$	Buldakov *et al.* [42]
$\partial^n P/\partial r^n$	Maroulis [58]

An example of the conversion of polarizability derivatives of N_2 in terms of atomic units to Å^3 is shown below.

Mean:

$\alpha = 11.71\ e^2 {a_0}^2 {E_h}^{-1}$

$1e^2 {a_0}^2 {E_h}^{-1} = 1.648778 \times 10^{-41} \text{C}^2\text{m}^2\text{J}^{-1}$ [58], so

$\alpha = 11.71 \times 1.648778 \times 10^{-41} \text{C}^2\text{m}^2\text{J}^{-1}$.

Now,

$\alpha[\text{Å}^3] = \frac{10^{30}}{4\pi\epsilon_0} \alpha[\text{C}^2\text{m}^2\text{J}^{-1}]$ [74],

where $\epsilon_0 = 8.8541878176 \times 10^{-12}\ \frac{\text{F}}{\text{m}}$

So, $\alpha = 11.71 \times 1.648778 \times 10^{-41} \times \frac{10^{30}}{4\pi\epsilon_0} \text{Å}^3 = 1.74\ \text{Å}^3$

Derivative of the mean:

$\alpha' = \frac{d\alpha}{dr} = 5.98\ \text{e}^2 a_0 {E_h}^{-1}$

Now,

$\alpha' = \frac{d\alpha}{dr} . r = 5.98 e^2 a_0 E_h^{-1} \times 2.07432 a_0 = 1.84\ \text{Å}^3$

Long [24] defines polarizability derivatives with respect to mass adjusted normal coordinates as $\frac{\partial P}{\partial Q}$. Here Q is the mass adjusted normal coordinate, and the units of P' are $\text{C}^2\text{mJ}^{-1}\text{kg}^{-1/2}$.

In a similar spirit some references state polarizability explicitly as a Taylor series [57, 65] while others express it as a polynomial [55, 58]. This means when Buldakov's values of polarizability derivatives are used in the expressions given by Tipping *et al*. they should be multiplied by $\frac{1}{n!}$.

Appendix E: Raman Gas Cell

A Raman gas cell was designed and machined to measure spectra from gases at room temperature. This section contains the designs of the parts of the cell. The glands for the O-rings were designed by following the guidelines given in O-Ring Design and Materials Guide by R.L. Hudson & Company. The two point alignment was demonstrated in the lab, and it is shown in Fig. E.1. The cell can be firmly attached to a post. It has a threaded hole on the top surface where a valve can be attached. The laser windows are 20QW20-2 by Newport and the signal windows are PW-1925-UV by CVI Melles Griot.

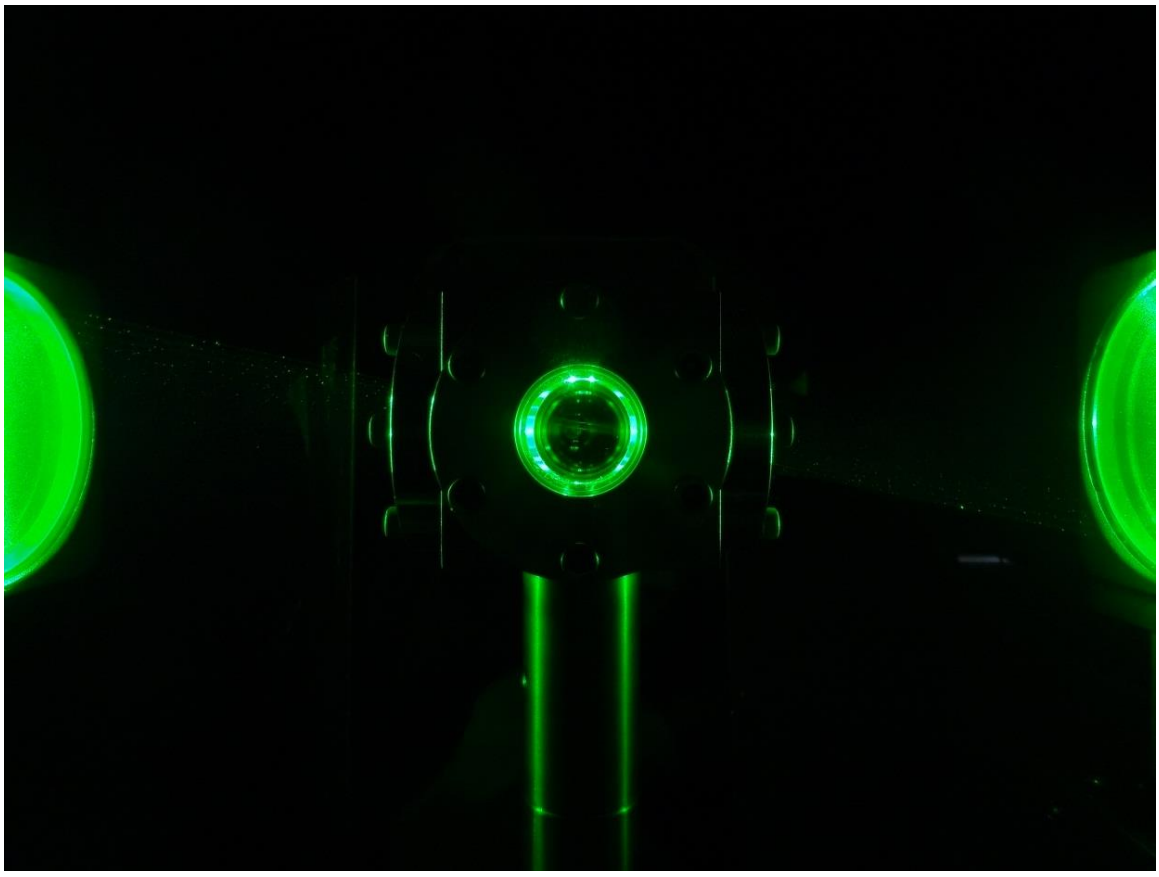

Figure E.1: Multiple-pass two point alignment in a sample cell

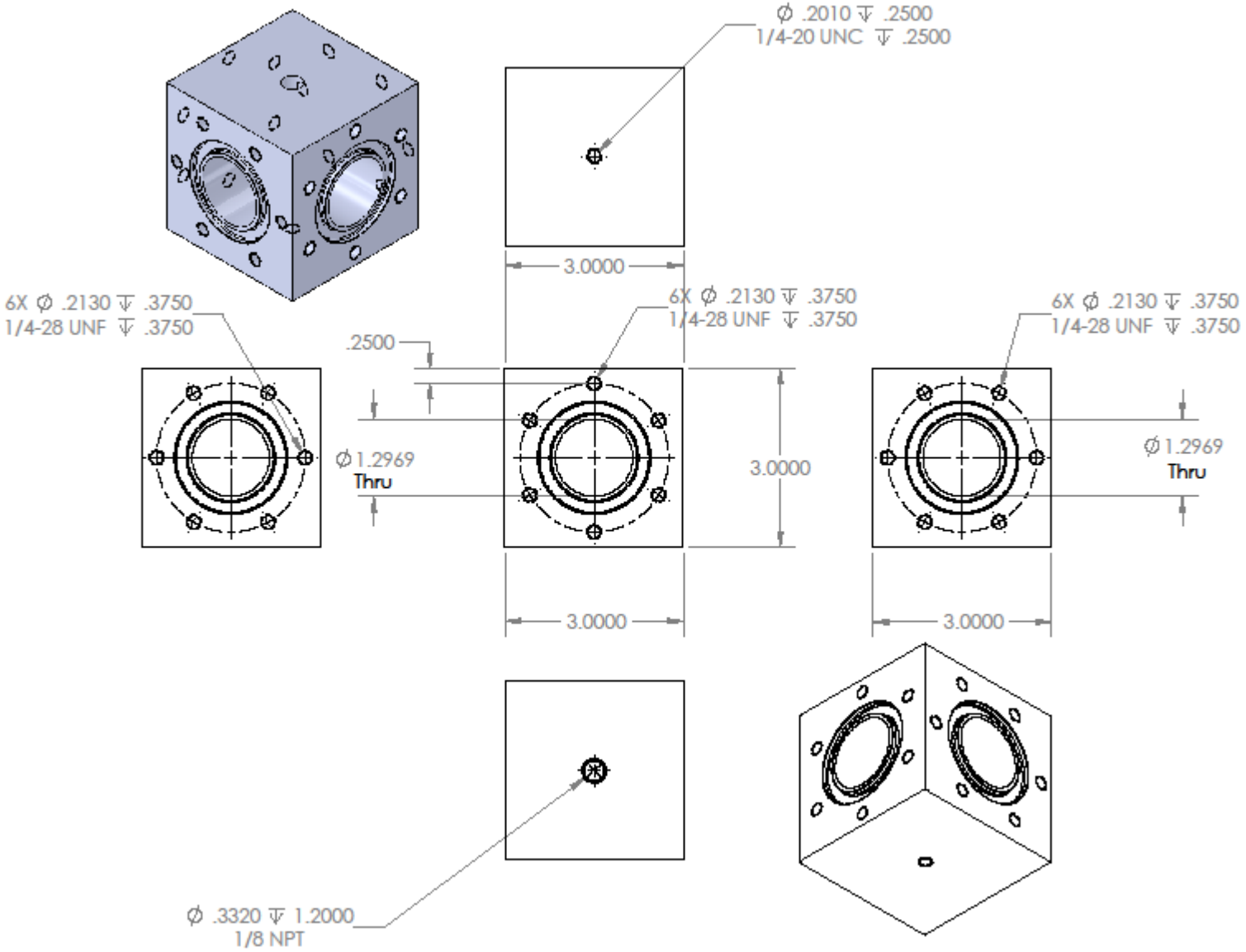
Ø .2010 ↧ .2500
1/4-20 UNC ↧ .2500
3.0000
6X Ø .2130 ↧ .3750
1/4-28 UNF ↧ .3750
6X Ø .2130 ↧ .3750
1/4-28 UNF ↧ .3750
6X Ø .2130 ↧ .3750
1/4-28 UNF ↧ .3750
.2500
Ø1.2969
Thru
3.0000
Ø1.2969
Thru
3.0000
3.0000
Ø .3320 ↧ 1.2000
1/8 NPT

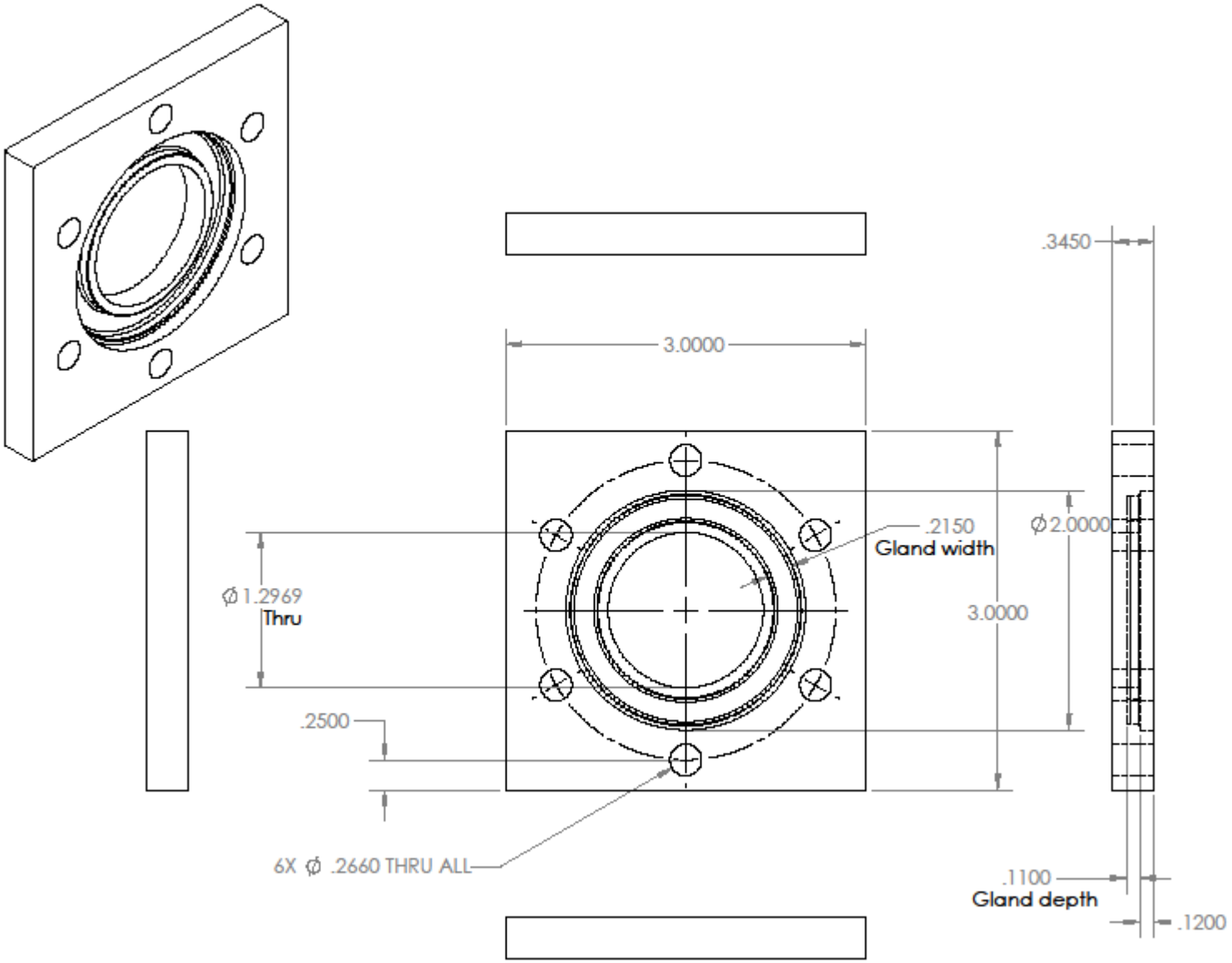
.3450
3.0000
Ø2.0000
.2150
Gland width
Ø1.2969
Thru
3.0000
.2500
6X Ø .2660 THRU ALL
.1100
Gland depth
.1200

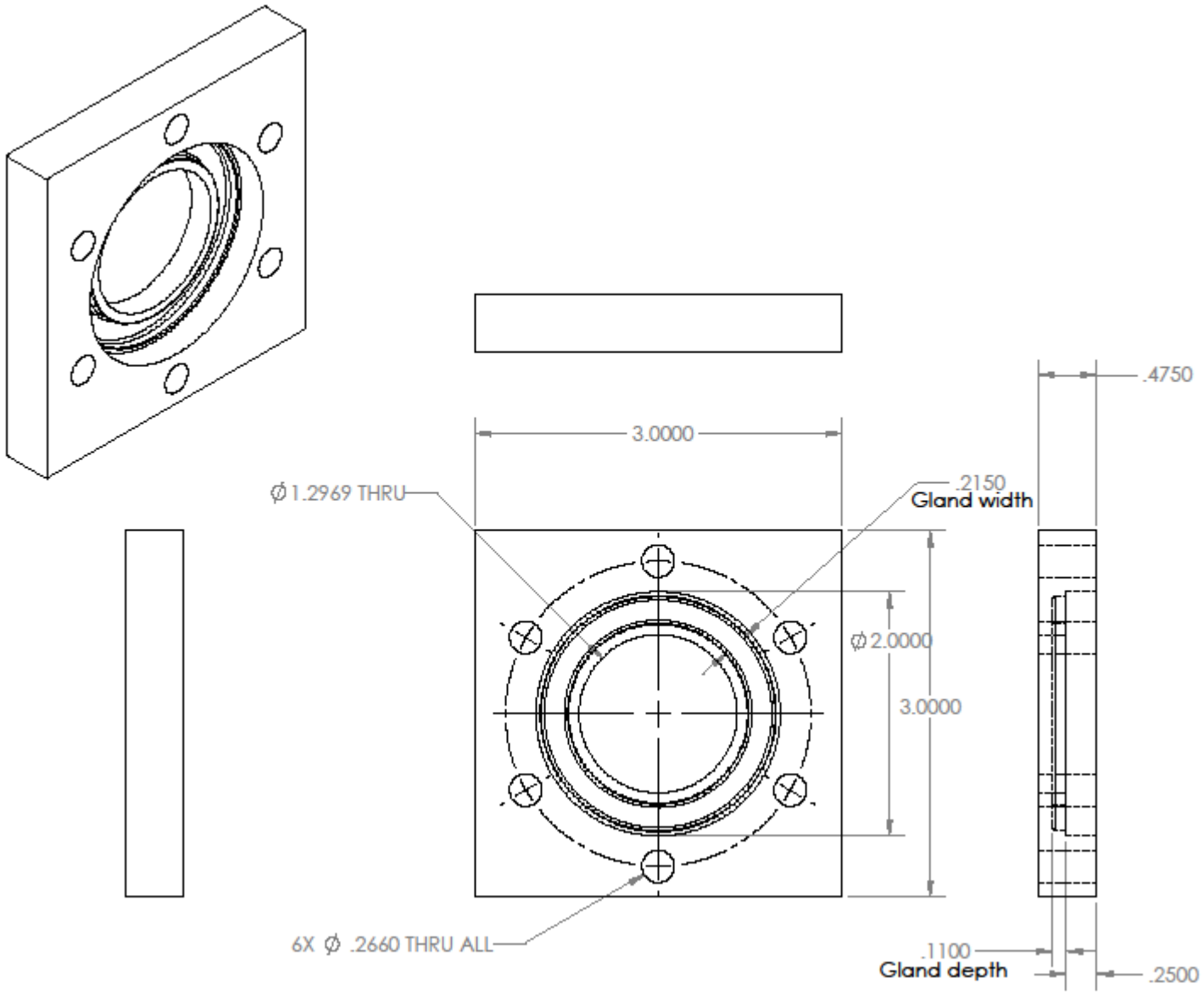
.4750
3.0000
Ø1.2969 THRU
.2150
Gland width
Ø2.0000
3.0000
6X Ø .2660 THRU ALL
.1100
Gland depth
.2500

References

1. Fran Adar, Michel Delhaye, Edouard DaSilva, “Evolution of Instrumentation for Detection of the Raman Effect as Driven by Available Technologies and by Developing Applications,” http://www.jobinyvon.com/usadivisions/Raman/applications/waters_symposium_pittcon.pdf
2. Alan C. Eckbreth, *Laser Diagnostics for Combustion Temperature and Species* (Gordon and Breach Publishers, 1996).
3. C. N. Banwell, *Fundamentals of Molecular Spectroscopy* (McGraw-Hill, 1983).
4. John M. Brown, *Molecular Spectroscopy* (Oxford Science Publications, 1998).
5. Richard B. Miles, Walter R. Lempert, and Joseph N. Forkey, "Laser Rayleigh scattering." Measurement Science and Technology **12**, Issue 5, R33 (2001).
6. W. M. Tolles, J. W. Nibbler, J. R. McDonald, and A. B. Harvey, "A review of the theory and application of coherent anti-Stokes Raman spectroscopy CARS)," Applied Spectroscopy **31**, Issue 4, pp. 253-271 (1977).
7. M. Woyde and W. Stricker, "The application of CARS for temperature measurements in high pressure combustion systems," Applied Physics B **50**, Issue 6, pp. 519-525 (1990).
8. R. S. Barlow, R. W. Dibble, and Robert P. Lucht, "Simultaneous measurement of Raman scattering and laser-induced OH fluorescence in nonpremixed turbulent jet flames," Optics letters **14**, Issue 5, pp. 263-265 (1989).

9. R. W. Dibble, W. Kollmann, and R. W. Schefer, "Conserved scalar fluxes measured in a turbulent nonpremixed flame by combined laser Doppler velocimetry and laser Raman scattering," Combustion and flame **55**, Issue 3, pp. 307-321 (1984).
10. K. J. Rensburger, J. B. Jeffries, R. A. Copeland, K. Kohse-Hoinghaus, M. L. Wise and D. R. Crosley, "Laser-induced fluorescence determination of temperatures in low pressure flames," Applied optics **28**, Issue 17, pp. 3556-3566 (1989).
11. John E. Dec and J. O. Keller, "High speed thermometry using two-line atomic fluorescence," Symposium (International) on Combustion,. Vol. **21**. No. 1. Elsevier, (1988).
12. Robert Cattolica, "OH rotational temperature from two-line laser-excited fluorescence," Applied Optics **20**, Issue7, pp. 1156-1166 (1981).
13. J. H. Grinstead, G. Laufer and J. C. McDaniel Jr., "Single-pulse, two-line temperature-measurement technique using KrF laser-induced O_2 fluorescence," Applied optics **34**, Issue 24, pp. 5501-5512 (1995).
14. J. H. Grinstead, T. M. Quagliaroli, G. Laufer and J. C. McDaniel, "Single-pulse temperature measurements in a turbulent flame using KrF laser-induced O_2 fluorescence," AIAA, Aerospace Sciences Meeting and Exhibit, 33 rd, Reno, NV (1995).
15. P Ferrão and M. V. Heitor, "Probe and optical diagnostics for scalar measurements in premixed flames," Experiments in fluids **24**, Issue 5-6, pp. 389-398 (1998).

16. Gregory S. Elliott, Nick Glumac and Campbell D. Carter, "Molecular filtered Rayleigh scattering applied to combustion," Measurement Science and Technology **12**, Issue 4, pp. 452 (2001).
17. Robert J. Hall and Alan C. Eckbreth, "Combustion diagnosis by coherent anti-Stokes Raman spectroscopy (CARS)," Optical Engineering **20**, Issue 4, pp. 494-500 (1981).
18. Roger L. Farrow, P. L. Mattern and Larry A. Rahn, "Comparison between CARS and corrected thermocouple temperature measurements in a diffusion flame," Applied Optics **21**, Issue 17, pp. 3119-3125 (1982).
19. Michael C. Drake, and Gerd M. Rosenblatt, "Flame temperatures from Raman scattering," Chemical Physics Letters **44**, Issue 2, pp. 313-316 (1976).
20. G. Alessandretti , "Some results on the measurement of temperature and density in a flame by Raman spectroscopy," Journal of Modern Optics **27**, Issue 8, pp. 1095-1103 (1980).
21. A. V. Sepman, V. V. Toro, A. V. Mokhov, H. B. Levinsky, "Determination of temperature and concentrations of main components in flames by fitting measured Raman spectra," Applied Physics B, pp. 1-13 (2013).
22. Fuest, Frederik, et al. "Raman/Rayleigh scattering and CO-LIF measurements in laminar and turbulent jet flames of dimethyl ether." Combustion and Flame159.8 (2012): 2533-2562.
23. University of Cambridge, DoITPoMS, TLP Library, “Raman Spectroscopy,” http://www.doitpoms.ac.uk/tlplib/raman/active_modes.php
24. D. A. Long, *Raman Spectroscopy* (McGraw-Hill, 1977)

25. D. A. Long, *The Raman Effect* (John Wiley & Sons, 2002)

26. A. J. Mulac, W. L. Flower, R. A. Hill, and D. P. Aeschliman, "Pulsed spontaneous Raman scattering technique for luminous environments," Applied Optics **17**, Issue 17, pp. 2695-2699 (1978).

27. W. R. Trutna and R. L. Byer, "Multiple-pass Raman gain cell," Applied Optics **19**, Issue 2, pp. 301-312 (1980).

28. William F. Pearman, J. Chance Carter, S. Michael Angel, and James W-J. Chan, "Quantitative measurements of CO_2 and CH_4 using a multipass Raman capillary cell," Applied Optics **47**, Issue 25, pp. 4627-4632 (2008).

29. Mikael Afzelius, Per-Erik Bengtsson, Joakim Bood, Christian Brackmann, and Alfred Kurtz, "Development of multipoint vibrational coherent anti-Stokes Raman spectroscopy for flame applications," Applied Optics **45**, Issue 6, pp. 1177-1186 (2006).

30. Xiaoyun Li, Yuxing Xia, Li Zhan, and Juming Huang, "Near-confocal cavity-enhanced Raman spectroscopy for multitrace-gas detection," Optics Letters **33**, Issue 18, pp. 2143-2145 (2008).

31. M. Fink and J Campbell, "An all-quartz cell for multipass cavity," Review of Scientific Instruments **77**, Issue 3, pp. 036113-036113-2 (2006).

32. Gregor A. Waldherr and Hai Lin, "Gain analysis of an optical multipass cell for spectroscopic measurements in luminous environments," Applied Optics 47, Issue 7, pp. 901-907 (2008).

33. B. N. Ganguly, “Hydrocarbon combustion enhancement by applied electric field and plasma kinetics,” Plasma Phys. Control. Fusion **49**, B239-B246 (2007).

34. D. L. Wisman, S. D. Marcum, and B. N. Ganguly, “Electrical control of the thermodiffusive instability in premixed propane-air flames,” Combust. Flame **151**, 639-649 (2007).

35. Jun Kojima and Quang-Viet Nguyen, “Laser pulse-stretching with multiple optical ring cavities,” Applied Optics **41**, Issue 30, pp. 6360-6370 (2002).

36. Utsav KC, Joel A. Silver, David C. Hovde, and Philip L. Varghese, “Improved multiple-pass Raman spectrometer,” Applied Optics **50**, Issue 24, pp. 4805-4816 (2011).

37. Jun Kojima and Quang-Viet Nguyen, Spontaneous Raman Scattering Diagnostics: Applications in Practical Combustion Systems. Handbook of Combustion, 125-154, (Wiley-VCH Verlag GmbH & Co. KGaA, 2010).

38. Ralchenko, Yu., Kramida, A., Reader, J. and NIST ASD Team (2011). NIST Atomic Spectra Database (version 4.1), [Online]. Available: http://physics.nist.gov/asd

39. S. B. Kim, R. M. Hammaker, and W. G. Fateley, "Calibrating Raman Spectrometers Using a Neon Lamp," Appl. Spectrosc. **40**, 412-415 (1986).

40. J. A. Stone Jr., J. H. Zimmerman,“Index of Refraction of Air,” http://emtoolbox.nist.gov/Wavelength/Documentation.asp

41. Kaiser Optical Systems, Inc, “VPH Tutorial and FAQ,” http://www.kosi.com/Holographic_Gratings/vph_tutorial_faq.php

42. M. A. Buldakov, V. N. Cherepanov, B.V. Korolev, and I. I. Matrosov, "Role of intramolecular interactions in Raman spectra of N_2 and O_2 molecules," Journal of Molecular Spectroscopy **217**, 1-8 (2003).

43. Michael Berglund and Michael E. Wieser, "Isotopic Compositions of the Elements 2009 (IUPAC Technical Report)," Pure Appl. Chem. **83**, No. 2, 397-410 (2011)

44. R. R. Laher and F. R. Gilmore, "Improved fits for the vibrational and rotational constants of many states of nitrogen and oxygen," J. Phys. Chem. Ref. Data **20**, 685-712 (1991)

45. J. Bendtsen, "High-resolution Fourier transform Raman spectra of the fundamental bands of $^{14}N^{15}N$ and $^{15}N_2$," J. Raman Spectrosc. **32**, 989-995 (2001)

46. G. Herzberg, *Molecular Spectra and Molecular Structure I. Spectra of Diatomic Molecules* (D. Van Nostrand Company, 1950)

47. M. Pecul, A. Rizzo, "Linear response coupled cluster calculation of Raman scattering cross sections," Journal of Chemical Physics **116**, 1259-1268 (2002)

48. R. H. Tipping, J.-P. Bouanich, "On the use of Herman-Wallis factors for diatomic molecules," Journal of Quantitative Spectroscopy & Radiative Transfer **71**, 99-103 (2001)

49. Michele Marrocco, "Reliability of Herman-Wallis factors for Raman spectroscopy of Q-branch molecular transitions," Chemical Physics Letters **442**, 224-227 (2007)

50. Michele Marrocco, "Herman-Wallis factor to improve thermometric accuracy of vibrational coherent anti-Stokes Raman spectra of H_2,", Proceedings of the Combustion Institute **32**, 863-870 (2009)

51. Michele Marrocco, “CARS thermometry revisited in light of the intramolecular perturbation,” J. Raman Spectrosc. **41**, 870-874 (2010)

52. Michele Marrocco, “Herman-Wallis correction in vibrational CARS of oxygen,” J. Raman Spectrosc. **42**, 1836-1842 (2011)

53. Michele Marroco, “Comparative analysis of Herman-Wallis factors for uses in coherent anti-Stokes Raman spectra of light molecules,” J. Raman Spectrosc. **40**, 741-747 (2009)

54. Alexis Bohlin, Per-Erik Bengtsson and Michele Marrocco, “On the sensitivity of rotational CARS N_2 thermometry to the Herman-Wallis factor,” J. Raman Spectrosc. **42**, 1843-1847 (2011)

55. R. H. Tipping, J. F. Ogilvie, “Herman-Wallis factors for Raman transitions of $^1\Sigma$-state diatomic molecules,” Journal of Raman Spectroscopy **15**, 38-40 (1984)

56. T. C. James and W. Klemperer, “Line intensities in the Raman effect of $^1\Sigma$ diatomic molecules,” Journal of Chemical Physics **31**, 130-134 (1959)

57. W. Knippers, K. Van Helvoort, and S. Stolte, “Vibrational overtones of the homonuclear diatomics (N_2, O_2, D_2) observed by the spontaneous Raman effect,” Chem. Phys. Lett. **121**, 279-286 (1985)

58. G. Maroulis, “Accurate electric multipole moment, static polarizability and hyperpolarizability derivatives for N_2,” J. Chem. Phys. **118**, 2673 (2003)

59. P. L. Polavarapu, “*Ab initio* vibrational Raman and Raman optical activity spectra,” J. Phys. Chem. **94**, 8106-8112 (1990)

60. D. Bradley and K. J. Matthews, "Measurement of High Gas Temperatures with Fine Wire Thermocouples," J. Mechan. Eng. Science **10**, 299-305 (1968).

61. C. Davisson and J. R. Weeks Jr., "The Relation Between the Total Thermal Emissive Power of a Metal and its Electrical Resistivity," J. Opt. Soc. Am. **8**, 581-602 (1924).

62. R. F. Vines, *The Platinum Metals and Their Alloys* (The International Nickel Company Inc., 1941).

63. C. Morley, "GASEQ A Chemical Equilibrium Program for Windows," http://www.c.morley.dsl.pipex.com/.

64. Stephen R. Langhoff, Charles W. Bauschlicher, and Delano P. Chong, "Theoretical Study of the Effects of Vibrational-Rotational Interactions on the Raman Spectrum of N_2," J. Chem. Phys. **78**, 5287 (1983)

65. M.A. Buldakov, I.I. Ippolitov, B.V. Korolev, I.I. Matrosov, A.E. Cheglokov, V.N. Cherepanov, Yu.S. Makushkin, O.N. Ulenikov, "Vibration rotation Raman spectroscopy of gas media," Spectrochimica Acta Part A: Molecular and Biomolecular Spectroscopy, Volume **52**, Issue 8, Pages 995-1007 (1996)

66. US Energy Information Administration, "How much natural gas does the United States have and how long will it last?" http://www.eia.gov/tools/faqs/faq.cfm?id=58&t=8

67. John B. Curtis, "U.S. Shale Gas From Resources and Reserves to Carbon Isotope Anomalies," http://energyseminar.stanford.edu/sites/all/files/eventpdf/JohnCurtisStanfordShale.pdf

68. Sathuluri RR, Yoshikawa H, Shimizu E, Saito M, Tamiya E, "Gold Nanoparticle-Based Surface-Enhanced Raman Scattering for Noninvasive Molecular Probing of Embryonic Stem Cell Differentiation," PLoS ONE 6(8): e22802 (2011)

69. Glenn Elert, "Diameter of a speck of dust," The Physics Factbook, http://hypertextbook.com/facts/2003/MarinaBolotovsky.shtml

70. NIST, "Diatomic Constants for H_2," http://webbook.nist.gov/cgi/cbook.cgi?ID=C1333740&Mask=1000

71. C.L. Beckel and F. Wu, paper presented at the 27th Symposium on Molecular Structure and Spectroscopy, Columbus, Ohio, 1972, paper AA9

72. W. Kolos and L. Wolniewicz, "Polarizability of the Hydrogen Molecule," J. Chem. Phys. **46**, 1426 (1967)

73. Lap M. Cheung, David M. Bishop, David L. Drapcho, Gerd M. Rosenblatt, "Relative Raman Line Intensities for H_2 and D_2. Correction Factors for Molecular Non-Rigidity," Chemical Physics Letters, **80**, Issue 3, 445-450 (June 1981)

74. Jefferey K. Nagle, "Atomic Polarizability and Electronegativity," J. Am. Chem. Vol. **112**, No. 12 (1990)